Assessing the Behaviour of Solid Particulates in the Flow of Molten Salt Reactor Coolant Circuits

by

Cole William Arthurs

A Project submitted to the
School of Graduate and Postdoctoral Studies in partial
fulfillment of the requirements for the degree of

Master of Engineering in **Nuclear Engineering**

Faculty of Engineering and Applied Science

University of Ontario Institute of Technology (Ontario Tech University)

Oshawa, Ontario, Canada

April 2023

REVIEW INFORMATION

Submitted by: **Cole Arthurs**

Master of Engineering in **Nuclear Engineering**

Project Title: Assessing the Behaviour of Solid Particulates in the Flow of Molten Salt Reactor Coolant Circuits

The Project was approved on April 17, 2023 by the following review committee:

Review Committee:

Research Supervisor	Dr. Markus Piro
Second Reader	Dr. Jennifer McKellar

The above review committee determined that the Project is acceptable in form and content and that a satisfactory knowledge of the field was covered by the work submitted. A copy of the Certificate of Approval is available from the School of Graduate and Postdoctoral Studies.

ABSTRACT

This work investigated solid particulate behaviour in molten salt nuclear reactors. Solid particulates are expected to form from fission products reacting with fuel components, creating compounds with melting temperatures above the reactor operational temperature. These particulates may present operational risks including flow obstruction and corrosion. A sensitivity analysis was performed by simulating flow of molten salt within a reactor containing solid particulates via Computational Fluid Dynamics, where three parameters of the particulate were varied: diameter, density, and initial concentration. A case was simulated where values for these properties were selected based on a review of related literature. Subsequently, two more simulations were performed for each parameter using high and low values within the expected ranges, modifying only one parameter at a time. Results indicate that particle diameter has low impact on fluid dynamics of the reactor, but particulate density and concentration resulted in increased localized accumulation and cyclical movement of the particulate at the reactor outer edges.

Keywords: Molten Salt; Solid Particulate; Multiphase Flow; OpenFOAM, Sensitivity Analysis

AUTHOR'S DECLARATION

I hereby declare that this report consists of original work of which I have authored. This is a true copy of the report, including any required final revisions, as accepted by my examiners.

I authorize the University of Ontario Institute of Technology (Ontario Tech University) to lend this report to other institutions or individuals for the purpose of scholarly research. I further authorize University of Ontario Institute of Technology (Ontario Tech University) to reproduce this report by photocopying or by other means, in total or in part, at the request of other institutions or individuals for the purpose of scholarly research. I understand that this report may be made electronically available to the public.

Cole William Arthurs

STATEMENT OF CONTRIBUTIONS

I hereby certify that I am the sole author of this report and that no part of this report has been published or submitted for publication. I have used standard referencing practices to acknowledge ideas, research techniques, or other materials that belong to others. Furthermore, I hereby certify that I am the sole source of the creative works and/or inventive knowledge described in this report.

ACKNOWLEDGEMENTS

I would like to thank my supervisor for this work, Dr. Markus Piro, for his guidance and support selecting an interesting project that contributes to the scientific community. The recommendations and advice he provided during my master's courses and while I was performing this work were extremely educational and I appreciate them greatly. The benefit I gained from the effort he put into reviewing this report and working with me through the past several years is incalculable.

To my peers Nikolas Scuro, Lowell Bower, and Zheng Lu, thank you for your support throughout this endeavour. Your guidance in using OpenFOAM, our working together in sharing reference information for molten salt reactors, and support in the remote use of supercomputers for modelling and performing simulations was extremely useful.

The Nuclear Fuels and Materials Group as a whole is thanked for their great support throughout my time with the group. Many on the team have contributed in ways that have been invaluable to my development.

Finally, I would like to thank my family. My parents for their continued support throughout my years of education, including the stimulating discussions and moral support, and my wife for her endless motivational support and help with everything in my life that has allowed me to be successful in completing this work.

Computing resources provided by Compute Canada are appreciated as well. Work performed to facilitate this paper was possible in part thanks to funding from the Canada Research Chairs program (950-231328) of the Natural Sciences and Engineering Research Council of Canada.

CONTENTS

List of Figures

List of Tables

LIST OF ACRONYMS

CFD Computational Fluid Dynamics

EVOL Evaluation and Viability of Liquid Fuel Fast Reactor System

FP Fission Product

JRC MSD Joint Research Centre Molten Salt Database

LES Large Eddy Simulation

MSFR Molten Salt Fast Reactor

MSR Molten Salt Reactor

MSRE Molten Salt Reactor Experiment

OpenFOAM Open Source Field Operation and Manipulation

ORNL Oak Ridge National Laboratory

RANS Reynolds-Averaged Navier Stokes

RAS Reynolds-Averaged Simulation

SAMOFAR Safety Assessment of the Molten Salt Fast Reactor

SAMOSAFER Severe Accident Modeling and Safety Assessment for Fluid-fuel Energy Reactors

TAF-ID Thermodynamics of Advanced Fuels - International Database

1

INTRODUCTION

Molten Salt Reactors (MSR) are a liquid-fueled reactor design included as one of the Generation IV nuclear fission reactors for which there is ongoing research for industrial applications [1]. To date, demonstration MSRs have been successfully constructed and operated for research purposes (e.g. Oak Ridge National Laboratory [2]), and after a long pause on construction of MSRs, new demonstration reactors are being constructed for tests with the ultimate intent of using them for power generation [3]. Key benefits of MSRs include the low operational pressure, elimination of the risk of melting fuel since it is already molten, and in some cases, on-line fuel processing. Complications include material science given the high operational temperatures, the corrosive nature of molten salt, containment of the liquid fuel and gaseous fission products generated during operation, and mass accountancy [1] [4].

New solid compounds can be generated within an MSR in that fission products may interact with the molten salt. In some cases, new compounds will be generated with melting temperatures higher than that of the primary molten salt loop, and solid precipitates will form [5]. These precipitates may then present risks to the operation of the reactor, such as collecting in areas where they may impact or ob-

struct flow, erode components, and influence reactor physics. Flow obstruction can lead to insufficient cooling if an area is not receiving cooler salt. As some solid particulates may be harder than the walls of the reactor, recurring interaction could deteriorate surfaces in the long term. If solid particulates contain components that have very high neutron absorption cross sections, collection of solids in on area could considerably influence reactor physics. As such, it is important to model and assess the behaviour of solid particulates that result in fission products in MSRs, and understand how to manage them. The objective of this project is to improve understanding of the flow characteristics of solid particulates precipitated from the salt in an MSR core to help guide design features to mitigate the negative impacts of solid particulates on reactor operation. In this work, the Computational Fluid Dynamics (CFD) software code OpenFOAM is used to simulate relevant scenarios.

The following sections of this chapter include a review of MSR design, fuel properties, the method used to select the solid particulates, and an introduction to the CFD software used to perform simulations documented in this report.

1.1. INTRODUCTION TO MOLTEN SALT REACTORS

In a Canadian context, MSRs are an area of focus for displacing fossil fuels in industrial applications, reusing spent fuel from CANDU reactors, producing hydrogen, and adding power generation capacity to the electrical grid. Terrestrial Energy, who were one of the candidates for the Small Modular Reactor being built in Clarington, Ontario, are designers of an Integral Molten Salt Reactor (IMSR) [6]. They seek to deploy their modular cogeneration plant to provide process heat for heavy industry and produce electrical power [7]. Moltex Energy, a company designing a Stable Salt Reactor - Wasteburner (SSR-W), intend to power their reactor partially with the spent fuel from the Point Lepreau CANDU generating station, and claim that the reactor will be able to produce hydrogen in addition to process heat and power [8].

The properties selected for the MSR design considered in this work are related to those of the Safety Assessment of the Molten Salt Fast Reactor (SAMOFAR) and Severe Accident Modelling and Safety Assessment for Fluid-fuel Energy Reactor (SAMOSAFER) projects as prominent molten salt reactor projects in which properties are used that would be common to many molten salt reactors. The objective of the

SAMOFAR project was to demonstrate the safety features of the Molten Salt Fast Reactor (MSFR) through a series of experimental and simulation activities [9]. The SAMOSAFER project builds on the learnings of the SAMOFAR project with a focus on safety barrier behaviours in severe accident scenarios [10].

1.1.1. MOLTEN SALT REACTOR MODEL DESIGN

An MSR model was developed for this work. The model design is based on the MSFR originally outlined by the FP7 project EVOL (Evaluation and Viability of Liquid Fuel Fast Reactor System), which has also been a focus within the SAMOFAR and SAMOSAFER projects [11]. As depicted in Figure 1.1, the reactor includes a continuous molten salt core, which pumps the fluid from the base edges of containment, up through the core, and out at the top via piping that routes the flow through heat exchangers and back through the pumps to recirculate the salt. This was used as the basis for the 2-D model employed in this project, where the intent is to mimic the full model through using a portion of said model that would be representative of the full model through symmetry.

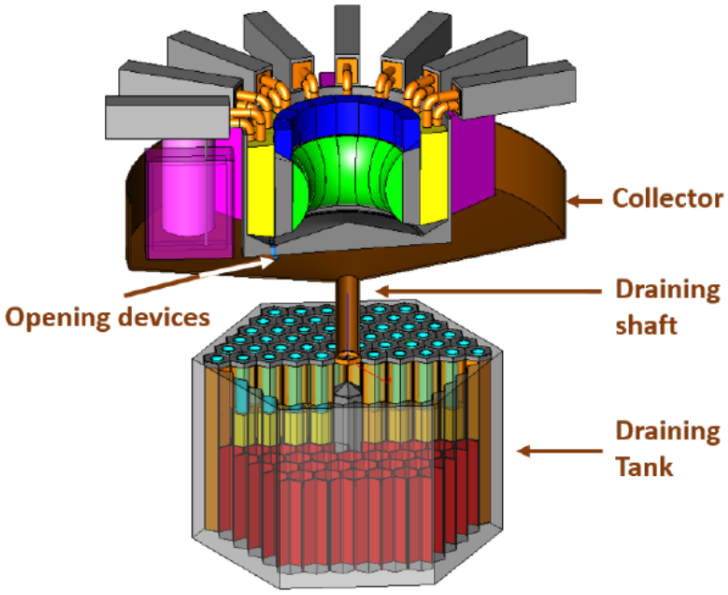

Figure 1.1: A Depiction of the SAMOSAFER MSFR and Drain Tank [10]

1.1.2. MOLTEN SALT COMPOSITION

Based on the work by Aufiero et al. for a similar MSFR, the salt is selected as LiF-ThF_4-$^{233}UF_3$ [12]. Lithium fluorides are a common component for molten salt fuels based on their properties that ad-

dress many constraints of molten salt reactors. The melting temperatures are sufficiently low and the boiling temperatures are sufficiently high to make them valid for moderate operational temperatures. They have low neutron absorption cross sections (i.e. they do not absorb many neutrons, so they are expected to have low impact on reactor physics) and thermal properties that allow them to be effectively used as coolants, due to the reduction in neutron parasitic absorption compared to other potential salt composites [13]. They allow for good solubility of fissile and fertile matters, and remain stable while undergoing irradiation [14]. Lithium-6 will interact with neutrons to form tritium, which can present radiation protection concerns for MSRs [15]. As ^{6}Li comprises 7.5% the natural abundance of Lithium with the remaining being ^{7}Li, it has been proposed that ^{7}Li be isotopically separated and used as the sole lithium component in MSRs [15][16]. Regarding the use of thorium, it is the fertile material for breeding, and the U-233 acts as the initial fissile material to start the reaction and breeding process.

1.1.3. SOLID PARTICULATE SELECTION

The properties of the solid particulates identified in this work were derived from two locations. The Joint Research Centre (JRC) Molten Salt Database (MSD) lists data for common compounds expected to occur in MSRs. This was used as a starting point to determine if any of the listed compounds could be solid at operational temperatures.

Secondly, a report previously prepared for a graduate level university course was sourced, and it included a review of the other likely elements that would form from transmutation and decay, and which compounds they would most likely form [17]. Those with melting temperatures higher than the expected operational temperature were recorded as likely to occur as solid precipitates. Those elements and compounds expected to be removed through helium sparging were not considered in this work.

1.2. INTRODUCTION TO OPENFOAM

OpenFOAM (Open-source Field Operation and Manipulation) is a software tool that can be used to solve differential equations for specific CFD problems as designed by the user. It is a C++ library in which executable applications are prepared to perform tasks to manipulate data and solve problems of continuum mechanics [18]. The capabilities of the solvers in OpenFOAM include multiphase flows such

as those that would be found in an MSR. Through simulation of two-phase liquid molten salt and solid precipitate flows in a partial MSR geometry, the behaviour of the particulate can be estimated such that experiments may be designed to demonstrate methods of managing this particulate.

1.3. REPORT STRUCTURE

The statement of work for this project is outlined in Chapter 2. Chapters 3 and 4 include the background required to understand the intent of this work, and the literature review details, respectively. Chapter 5 outlines the details of the first simulation performed. Chapter 6 includes the results of the parametric sensitivity analysis. Finally, the conclusions and recommendations for future work are captured in Chapters 7 and 8, respectively.

2

STATEMENT OF WORK

This chapter summarizes the problem being addressed by this work, the objective of this work, and the scope of the work in the form of a task list.

2.1. PROBLEM STATEMENT

There are a number of projects that have been completed or are in-progress related to the development of MSR technology, such as the Evaluation and Viability of Liquid Fuel Fast Reactor System (EVOL), and the SAMOSAFER project, which builds on the SAMOFAR project with focus on the development of safety barriers for MSRs in severe accident scenarios.

To demonstrate the feasibility of MSRs, experimental work is required to support the safety license effort. Performing experimental work for MSRs is costly and time-consuming and as such, simulations should first be performed to orient the focus of experimental work to ensure the greatest possible value is obtained. Simulation work is used to design experiments before they are performed, identify knowledge gaps, and prioritize experimental work to use resources more efficiently.

2.2. OBJECTIVE STATEMENT

The objective of this project is to improve understanding of the flow characteristics of solid particulates precipitated from the salt in an MSR core. The physics of this are important to understand, as solid particulate may collect in certain areas within the reactor core, or specific particulate may have negative impact on the reactor and its operation. Knowing where the particles collect and how they behave will allow designers to make decisions around reactor geometry and other technologies to avoid particulate accumulation.

This work is part of a larger effort to gauge characteristics of molten salt flow, specifically focused on phase changes and interaction between solids, liquids, and gases in MSRs.

2.3. TASK LIST

i. A literature review was performed to identify the information required to simulate the flow of molten salt with suspended solid particulates in an axially symmetrical "slice" of an MSFR. This included model geometry, mesh requirements, and the composition and physical characteristics of the salt and solid particulates (Chapter 4).

ii. The Computational Fluid Dynamics (CFD) code was selected and simulation options were identified to best simulate the flow of molten salt with suspended solid particulates in an MSFR (Chapter 4).

iii. The behaviour of solid particulates flowing in molten salt was simulated in 2-D and baseline data for the simulation results were documented (Chapter 5).

iv. A parametric sensitivity analysis was performed to identify and document changes in molten salt flow behaviour caused by variations in the size, density, and concentration of particulates, and compared against the baseline data (Chapter 6).

v. The importance of the findings and recommendations for future work based on these details of the interaction between solid particulates and molten salt were documented in this report (Chapters 6, 7, and 8).

3

BACKGROUND

This chapter outlines background details associated with the key elements of this work. This includes a review of the properties of the molten salt core and solid particulate, variable parameters used to perform a sensitivity analysis against a base case scenario, and the OpenFOAM software. This will provide the required information to understand the process used to perform this work, and interpret the findings of this report.

3.1. MOLTEN SALT REACTOR PROPERTIES

MSRs are named as such as the core uses molten salt as the coolant and moderator, where it also contains the fissile and/or fertile material used to create fission [19]. They operate at low pressure compared to conventional fission reactors, but outlet temperatures can be in the range of 700°C to 850°C [19]. The heat is transferred to a secondary loop, typically molten salt that contains no radioactive material that is intended to create separation between the radioactive elements and the power generation circuit [19]. Following the intermediary molten salt circuit, the power generation technology remains as the

same as other thermal reactors (e.g. natural gas) with a turbine-generator configuration that converts mechanical energy from pressurized steam into electrical energy. Returning to the reactor, a freeze plug and drain tank are generally included in designs as the shutdown systems for these reactors [19]. Where the lower pressure minimizes the need for extremely fast shutdown systems, if the salt becomes too hot, the freeze plug melts and the salt is drained [1]. A mechanical ball valve could also be installed for manual shutdown of the reactor [1]. Another common feature of MSRs is online fuel processing. Gaseous fission products can be removed from the salt core through online neutral gas bubbling (e.g. helium sparging), a process that bubbles a neutral gas from the base of the reactor and removes dissolved gases from the core that can then be siphoned away and safely stored [1]. A chemical processing plant could also be used to remove solid fission products through chemical and mechanical filtration methods [1]. Figure 3.1 depicts an example of a MSR with some of the features described above.

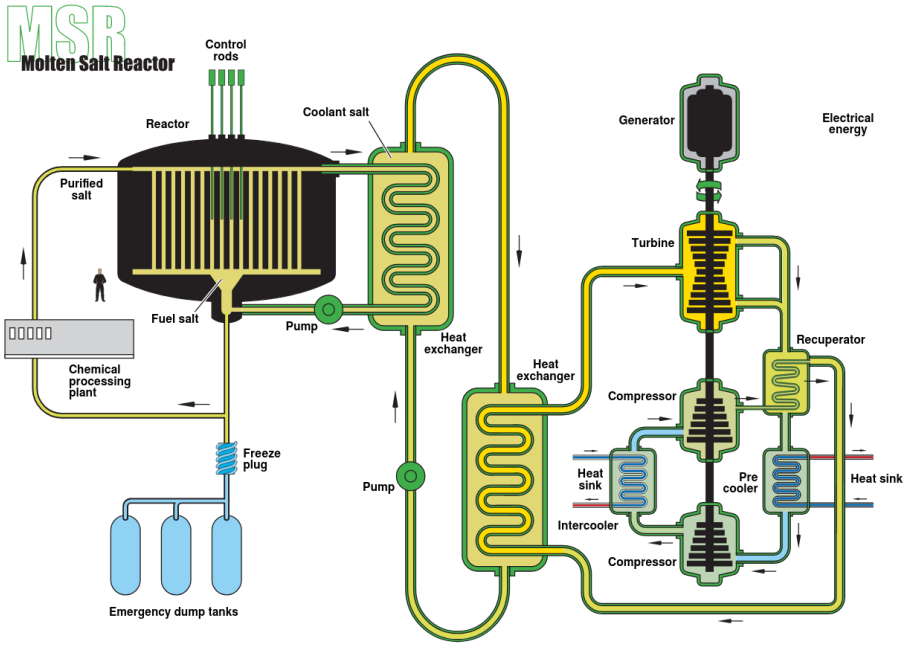

Figure 3.1: Example Molten Salt Reactor [19]

Benefits of MSRs include low operational pressure, the eliminated risk of melting fuel, and in some cases, on-line fuel processing. However, the chemistry of these reactors can present issues due to high operating temperatures and the corrosive nature of salts [1]. Managing the containment of the liquid fuel and gaseous fission products generated from operation also presents other challenges. There are various compositions of salt mixtures that can be used for MSRs that are conducive to the aforementioned

benefits, but must be selected to minimize the negative aspects of these reactors.

Commonly, molten salt fuels contain a lithium fluoride base. Some important parameters with regards to selection of a molten salt fuel includes the melting temperature, boiling temperature, neutron absorption cross sections, solubility for fuel components and being minimally impacted by irradiation that will be present in the core [14]. Lithium fluoride aligns with these properties, making it beneficial as a component for use in MSRs.

There are also different types of MSRs for which varied fuels would be more beneficial. Some are designed to operate with neutrons in the epithermal range and others in the fast spectrum [20]. In some cases, beryllium fluoride has been investigated as an alternate fuel base in conjunction with lithium fluoride in the form of LiF-BeF_2 (FLiBe) [20]. In addition, there are chloride salt-based fast MSR design concepts that are studied as a means of burning spent fuel from conventional reactors [20].

Oak Ridge National Laboratory (ORNL) performed a Molten Salt Reactor Experiment (MSRE), in which a thermal MSR was operated between 1965 and 1969 to study several properties of these reactors [21]. One finding was that the thermal neutron spectrum resulted in the need for higher effort processing of the salt so that fission products could be removed, and noted that using fast spectrum neutrons could alleviate this issue [1].

Partially based on those findings, the other more widely studied type of MSR today is a MSFR in which neutrons in the fast spectrum are used to breed fissile material from fertile isotopes. Here, U-233 is bred from Th-232. The work outlined in this report is based on MSFR technology, and as such has opted for a lithium fluoride based fuel. As laid out by Aufiero *et al.*, LiF-ThF_4-UF_3 (77.5-20-2.5 mol%) is one of the top candidates for MSR fuels [12]. It was selected as the fuel of focus for this report based on its prominence as a candidate for use in MSFRs and due to the high availability of data associated with its thermophysical properties.

Other relevant properties of the fuel required by OpenFOAM include the molecular weight, density, specific heat capacity, viscosity, and Prandtl number. These parameters and other conditions of the salt are reviewed in detail in Chapter 4. In this work, the salt properties are maintained constant as change in behaviour of the solid particulate is investigated. MSFRs tend to operate at approximately 700 °C (973 K)

and at somewhat near atmospheric pressure, which is reflected in the conditions of the simulations performed.

3.2. COMMON SOLID PARTICULATES

The Joint Research Centre (JRC) Molten Salt Database (MSD) is a collection of thermodynamic data associated with MSR technology, including data that can be used for phase diagram generation associated with key fuel components, fuel solvent and coolant components, and some fission and corrosion products [22]. The systems included in the JRC MSD include fluorine, iodine, and chlorine-based salts with fuel compounds such as uranium, thorium, and lithium. It also includes more prominent fission products such as zirconium, rubidium, molybdenum, iodine, and cesium [23] [24].

Other than the compounds included in the JRC MSD, previous investigatory work was performed in a project report titled "Knowledge Gap Assessment of the JRC Database for Irradiated Salts" prepared by Cole Arthurs [17]. This was used to identify other compounds that are likely to occur in higher, moderate, and lower concentrations within MSRs with a LiF-ThF_4-UF_3 fuel. This primarily includes fluorides and iodides, interacting with the primary fission products including cesium, lithium, thorium, zirconium, etc. The full composition is discussed in detail in the Literature Review.

Based on the identified compounds likely to occur in the MSFR, those that would remain as solids were identified based on their melting temperatures compared to the operational temperature of the reactor. In addition, the densities, approximate sizes, and concentration ranges were estimated and were the main focus of variable parameters in this work. The specific ranges and sources are outlined in the Literature Review.

3.3. OPENFOAM SOLVERS

OpenFOAM is a C++ library that is used for the solution of partial differential equations in the field of CFD [25]. Being open source, the original program has been split into at least two major variations. One is owned and managed by ESI Group/OpenCFD Ltd and the other is the OpenFOAM Foundation. They have many similarities and largely perform the same function, but there are some variations in the avail-

able options. Institutions and groups within them often select a variation initially to become familiar with the software, and it becomes the dominant variant used within that environment. Collaborators of the Nuclear Fuels and Materials Group of Ontario Tech University are using the OpenFOAM Foundation variation. As such, it was selected as the option of choice for this work. A benefit of performing this work using OpenFOAM is that there are no license fees given it is open-source.

A user generates a mesh either with the built-in meshing tools or with third party applications, which are then converted into the OpenFOAM meshing format. They then define the initial conditions, boundary conditions, and parameters to be calculated that align with the solver being used. This may include velocities, temperatures, pressures, turbulence properties, among others. In multiphase cases like those included in this report, volume fractions for the various phases are also tracked in each cell of the mesh. The solver then uses these inputs to resolve the basic equation that govern fluid mechanics: the Navier-Stokes equation. These are simplified into the mass continuity, momentum, and energy equations in OpenFOAM, which in this case are applied for two-dimensional incompressible flow of a Newtonian fluid.

The interface exists primarily through the terminal in a Linux operating system using the shell script generated within the OpenFOAM environment. It is run in C++ applications and employs "solvers" designed to include differential equations for step calculations of the aforementioned fields. This work included investigation into different solvers and ultimately opted to use *multiphaseEulerFoam*. This is a built-in multiphase Euler-Euler solver and was chosen over a Lagrangian particle tracking solver based on the computing resource requirements and the calculation methods used in related reports that this work draws upon. More details on the investigation and selection of this solver are discussed in the Literature Review including a description of the applications of the solver and contrasting it with others reviewed.

4

LITERATURE REVIEW

Captured in this chapter are the results of a literature review performed to identify related work completed to date, identify work not yet completed, and identify the properties of an MSR in the context of performing a CFD simulation. This includes details related to geometric modelling, mesh quality, MSR operational conditions, molten salt fuel, solid particulates, and CFD software including the applicable solvers and models. As no experiments have been performed that include details on the behaviour of solid particulates in MSRs, particularly of the configuration applied in this work, this literature review sources information primarily from work where simulations of MSRs were performed.

4.1. SUMMARY OF RELEVANT WORK

This section provides an overview of relevant works completed to date related to molten salt reactors with a focus on the MSFR model as it is used as a basis for the work in this report.

Cervi *et al.* have written two papers, presented by the same group of authors. The first was regarding a multiphysics model for fuel compressibility in the MSFR, and the second for a neutron transport

solver for the MSFR [26][27]. For the compressibility paper, they note that in cases where there are super-prompt-critical transients that occur rapidly, compressibility of the fuel can be important to understanding the behaviour of the system. It was found that compressibility of the fuel impacted the expansion of the fluid and that gas bubbles that occur in the fluid have a major impact on compressibility, meaning accurate two phase modelling is necessary to gauge the influence of compressibility during system transients. In the paper regarding neutron transport, Cervi *et al.* implemented a solver that interfaced with OpenFOAM to simulate neutron transport and determine how the physics of the two-phase liquid-gas flow influence reactivity. Specifically, it was identified that helium bubbling has a significant impact on reactivity, noting that helium sparging techniques will need to be carefully considered in MSFR control strategies.

Bajpai *et al.* simulated two-phase liquid-gas flow in an MSFR to predict the behaviour of inter gas bubbles that would occur in the core [28]. This was done using an Euler-Euler model to simulate the continuous (liquid fuel salt) and dispersed (small gas bubbles) phases. Similar to work by Cervi *et al.*, it was determined that the bubbles have significant potential to impact the reactivity of the system, depending on how they are dispersed.

Caruggi *et al.* developed a solver in OpenFOAM to investigate gaseous fission products and their influence on the reactor physics with specific focus on the helium bubbling system [29]. This included a multiphase Euler-Euler simulation of the continuous liquid phase and dispersed gaseous phases, but included functions to consider production consumption, transport, mass exchange, and removal of gases to the off-gas system. They successfully simulated this system in both 2-D and 3-D MSFR cases that further developed the study of two-phase flow in the MSFR concept.

The transient behaviour of the MSFR was considered and two models of the primary circuit in the reactor prepared by different institutional organizations were compared by Fiorina *et al.* [30]. The two models included turbulent fuel-salt flow, neutron diffusion, and delayed-neutron precursor diffusion and convection, using the Reynolds-Averaged Navier-Stokes (RANS) $\kappa - \epsilon$ model for turbulence in a 2-D mesh. The results indicated that the two models used were generally aligned, but had some variation in the temperature field that had impacts on dynamics of the reactor. They characterized both steady state and major accident scenarios, finding that the latter was largely benign as expected based on MSFR theory.

A method to identify Postulated Initiating Events (PIE) for the MSFR was prepared by Gerardin *et al.*, in which a Failure Mode and Effect Analysis (FMEA) and Master Logic Diagram (MLD) were employed [31]. They identified thirteen families of PIEs to be used as a basis for planning around failures and design basis accidents, such as reactivity insertion, loss of fuel circuit tightness, and loss of cooling.

Aufiero *et al.* [12] developed a multiphysics model using OpenFOAM to improve knowledge of transient scenarios in the MSFR. This included a 3-D model with coupling between neutronics code and the RANS equations for mass and momentum conservation, where a single pump failure accident scenario was simulated. The researchers found that the model functioned more suitably than existing techniques and that the approach may be useful during reactor design optimization for other transient scenario analysis.

Merle *et al.* analyzed the MSFR in an operational context, focusing on startup procedures and how the reactor would manage a load-following control scheme [14]. They outline the technique to load the reactor fuel, maintain its liquid state, reach criticality, and report on parameters such as temperature and reactivity throughout this sequence. Steps to control reactivity during operation are identified to allow for load-following operation. The paper notes that there control measures exist for the MSFR that allows for accurate control during start up procedures and fast load following during operation.

A preliminary design of the MSFR core in the context of thermal-hydraulics was prepared by Rouch *et al.* [32]. With the intent of accurately designing the core walls to ensure high quality of flow mixing and minimize peak temperatures in the model, the results found that the design features implemented were acceptable and achieved the stated objective. This was done with the use of a model that has curved walls and inlet/outlet legs, contrasted with other work that has employed a simplified rectangular model for computational efficiency.

Kamp prepared a thesis related to the freeze plug module in the SAMOSAFER MSFR and how the cooling requirements associated with this module [33]. Specifically, the cooling power required to solidify the fuel salt via the freeze plugs in an accident scenario necessitating use of the draining system was calculated, and design efficiencies were considered.

A large scale multi-year project entitled the Molten Salt Reactor Experiment (MSRE) was performed by Oak Ridge National Laboratory in which a research molten salt reactor was constructed and operated

to study this reactor design [2]. While research was extensive, the focus was on the fission products generated and how they influenced operational behaviour in a reactivity context. The design varied from the MSFR, but the experiment still considered gaseous fission products and use of an off-gas system. It also included a post-operation examination of the components of the reactor to gauge impact from extended operation.

Key trends are identifiable from these sources, namely the extensive investigation of multiphase flow for liquid-gas systems, the simulation and review of transient or accident scenarios for MSFRs, and basis technical feature design and analysis related to the MSFR concept. It is noted that there is limited research on the influence of solid particles in MSFRs. Based on this, documentation was reviewed outside of MSFR and generic molten salt reactor research to identify existing literature regarding solid particulates in molten salt in other applications and simple solid-liquid two-phase flow.

An article by Ong *et al.* performed a review of impurities expected to be found within molten salt in the application of Thermal Energy Storage (TES), specifically for concentrated solar power plants [34]. Common impurities or contaminants were identified and their influence on the operation of such a system were discussed. The primary focus was on the corrosive properties of the impurities, and how to purify the molten salt to avoid higher levels of contaminant concentration (heat processing and gas sparging). This is not directly related to the solid particulates considered in this report as the mentioned impurities are found either in the raw salt component, the atmosphere, or from the systems containing the salt. They tend to be low weight elements mixed into the salt, as opposed to larger solid particulates. While some can be found as solids, the article focuses on the impact on chemistry (i.e. corrosion, thermal stability).

Xu *et al.* looked at a model considering the heat transfer and fluid dynamics in a packed-bed molten salt thermocline TES system [35]. A transient 2-D model was prepared to review the heat transfer between the salt and spherical solid particles. However, the solid particles in this case are designed in the system to act as a means of increasing surface area between the two materials. This varies from the scenario considered in this report as the particles are much larger (1-25 cm compared to <3 mm) and they are not circulating within the system, not to mention they are part of the base design whereas fission products and the compounds they form are not.

Outside of molten salt applications, two-phase solid-liquid flow has been extensively researched, with focus on the fields of oil extraction, cement production, and processing of food and chemicals [36]. Mixing behaviour depends on key factors such as the density and viscosity of the continuous phase (generally the liquid), and the size, density, and concentration of the solid particles [36]. Peker and Helvaci review behaviour of particles in in book entitled "Solid-Liquid Two Phase Flow", in which they discuss the phenomenon of particle aggregation and the factors that influence it such as buoyancy and gravity (related to density variations between the particles and suspending medium), particle diameter, and forces between the particles [36].

It is apparent that there is little existing literature on the behaviour of solid particulates in molten salt, and more specifically two-phase solid-liquid flow in MSFRs. Noting that this report addresses the knowledge gap in the influence of solid particulates in the operation of molten salt reactors, the remaining sections of this literature review summarize reference information sourced largely from the works reviewed above, in order to identify properties of the MSFR used for the CFD simulations in this report. In addition, other sources are identified that were used to determine the properties of the solid particulates considered in this work.

4.2. GEOMETRIC MODEL

The elements of the geometric model researched for this report include general structure, dimensions, and the comparison of 2-D and 3-D simulations for similar work. Due to the focus on MSFRs similar to those used in the EVOL, SAMOFAR, and SAMOSAFER projects, papers and work employing the same general geometry were selected for comparison. Various sources contributing to those projects or similar work were sourced for dimensions. Cervi *et al.* provided relevant dimensions for a MSFR as follows: total diameter = 4.1 m (total radius = 2.05 m), core diameter = 2.26 m (core radius = 1.13 m), heat exchanger width = 0.22 m, and height = 2.26 m [26]. A two dimensional axially symmetric portion (i.e. a 2-D "slice") of the reactor core is used for OpenFOAM simulations in this paper, and it is stated that the SAMOFAR project framework was used to develop the work [26]. Bajpai et al. outlined details of a MSFR model in which geometric dimensions for a two-dimensional axially symmetric portion of the reactor core are also provided, with a core height of 2.255 m and a core plus heat exchanger radius of 2.0645 m [28]. The

width of the core is 1.1275 m and the width of the heat exchanger is 0.234 m. It is noted that the reactor concept used for this work was based on that initially used for research in the Euratom EVOL project, which was later applied to the SAMOFAR project. In another paper by Cervi *et al.*, a similar set up was arranged in which the 2D axial symmetric geometry is used again, with a total radius of 2.0645 m, a core radius of 1.1275 m, a heat exchanger width of 0.237 m, and core height of 2.255 m are applied [27]. This work was also modeled based on the SAMOFAR project. Fiorina *et al.* prepared a model based on the Euroatom EVOL project MSFR, in which approximate dimensions were determined, with a total radius of 2.125 m, a core radius of 1.125 m, a heat exchanger width of 0.25 m, and a height of 2.4 m is used [30]. This was also developed as a 2-D axial symmetric model.

A continued trend in reactor dimensions with a radius around 2.1 m and a height around 2.3 m was seen among other work including that done by Gerardin *et al.*, Kamp, and Merle *et al.* [14][31][33]. In the paper by Aufiero *et al.* related to development of an OpenFOAM model for the MSFR, both 2-D axial-symmetric and 3-D wedge symmetry models were applied [12]. While no specific dimensions were provided, the 3-D models provide a more detailed and realistic geometric shape of the reactor compared to other papers mentioned here. Caruggi *et al.* also performed 2-D and 3-D simulations for modelling of gaseous fission products, in which they provided a 3-D model of a MSFR, the cross section of which was used as a reference to generate the model used in this work to function as a 2-D model, symmetric about the central vertical axis [29]. A quarter core of the MSFR with four heat exchanger and pump loops from Caruggi *et al.* in shown in Figure 4.1, where for each heat exchanger and pump circuit, there is a symmetrical loop across the reactor core.

The trend of the focus on two-dimensional simulations for this type of work is based on the notion that the physics are not expected to vary in a significant manner from 2-D to 3-D simulations due to the symmetric nature about the vertical axis of the reactor.

4.3. MESH

Fiorina *et al.*, who used a 2-D mesh for the work, noted that 39,896 cells were used in the work in a triangular mesh for the core where rectangular elements were used closer to the walls [30]. Bajpai *et al.* used a similar approach of triangular elements and then refining the mesh as it approaches the walls, with the

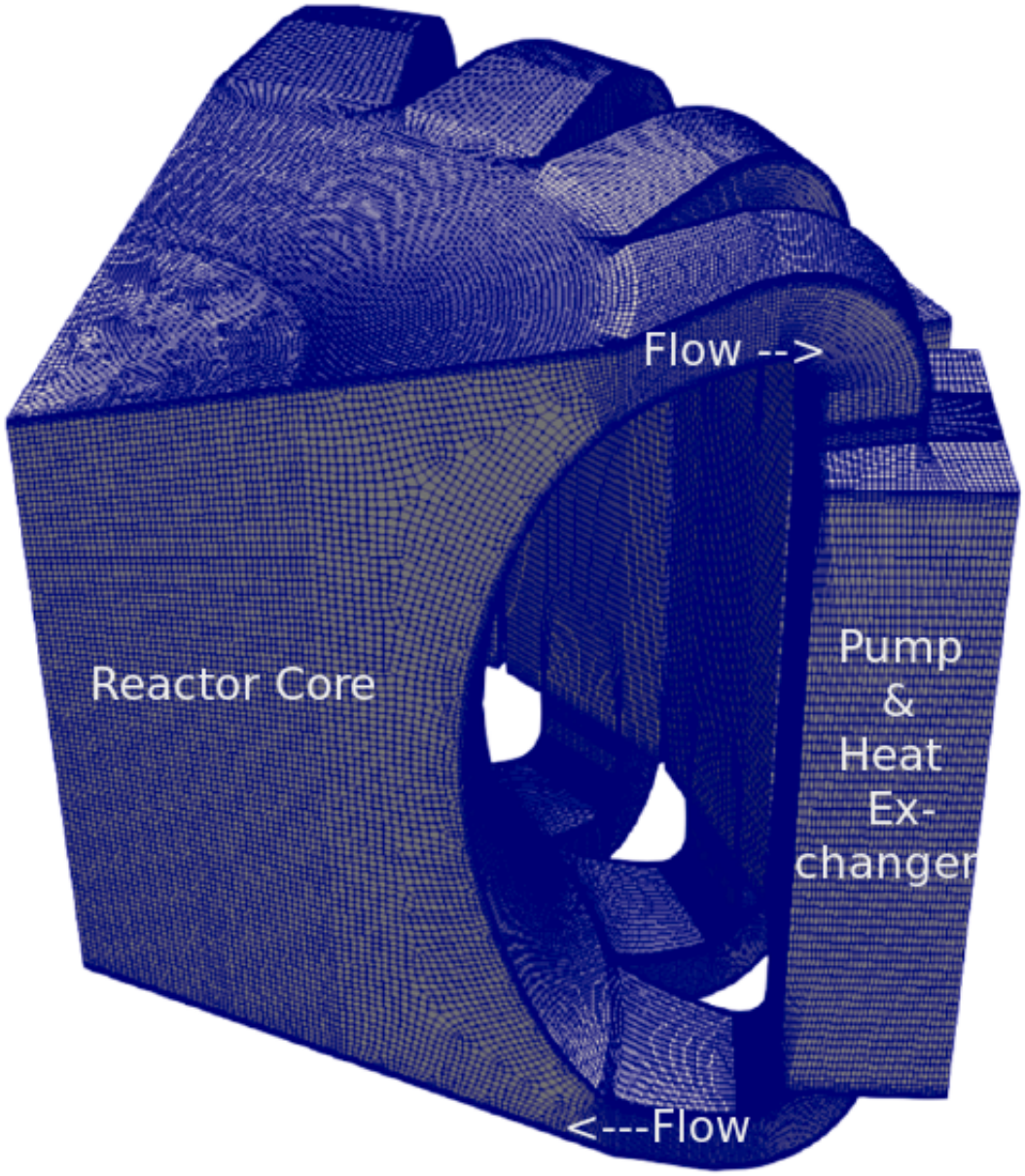

Figure 4.1: Computational mesh employed for 3-D simulations by Caruggi *et al.* [29]

intent of balancing computational demand with accuracy [28]. Hexahedra elements were created from the quadrilateral surface elements in the paper by Rouch *et al.*, where prism elements were created from triangle surface elements [32]. It is noted that a full 3-D mesh, which made up a quarter of the core, had around 5 to 6 million cells [32]. For a similar quarter core model, Caruggi *et al.* had a 3-D mesh that was made up of nearly 2 million cells. Cervi *et al.* similarly noted that a few million cells would be required for the full core model for a proper representation of the entire core of an MSFR [26]. It is also noted that while Caruggi *et al.* did not specify a number of cells for their 2-D model, a review of the number of cells in the x and y axes of Figure 4.2 would indicate that approximately 30,000 cells were used in this simulation.

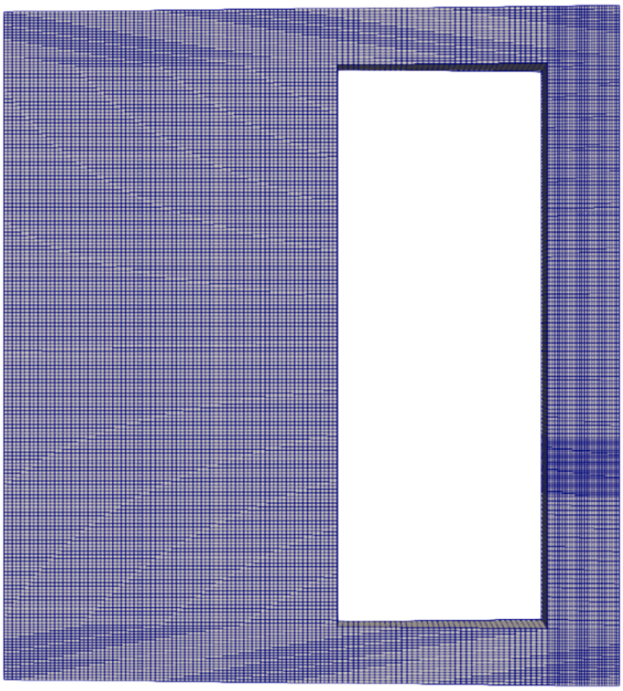

Figure 4.2: Computational mesh employed for 2-D simulations by Caruggi *et al.* [29]

4.4. MOLTEN SALT THERMOPHYSICAL PROPERTIES

4.4.1. FUEL SELECTION

The most prominent fuel composition outlined in the reviewed literature for related work included some form of LiF, typically at 77.5% of the mixture, and the remaining being a fluorine and actinide based compound. Specifically, Cervi *et al.* outline a fuel composition of LiF (77.5% mol) - ThF_4 (20.0% mol)

- $^{233}UF_4$ (2.5% mol) in both of the MSFR papers discussed previously [26][27]. Aufiero *et al.*, Tosolin *et al.*, and Carrugi *et al.* specify the same composition [12][13][29]. Das *et al.* outline a composition of LiF (77.5% mol) - ThF_4 (19.95% mol) - $^{233}UF_4$ (2.55% mol), which is nearly identical. Merle *et al.*, Bajpai *et al.*, Fiorina *et al.*, and Gerardin *et al.* have the same LiF mol percentage in the composition, with the same ratio for the mix of unspecified heavy nuclei fluorides [14][28][30][31]. Kamp's thesis deviated slightly with LiF-ThF_4 at 78-22 mol%. While the lithium fluoride-beryllium fluoride (a.k.a "FLiBe") was used in the ORNL Molten Salt Reactor Experiment, it contains beryllium, which is highly toxic and difficult to work with [37].

4.4.2. DENSITY

The density of the LiF (77.5% mol) - ThF_4 (19.95% mol) - $^{233}UF_4$ (2.55% mol) molten salt fuel ranges among the sources reviewed. Aufiero *et al.* specify a density of 4125 kg/m^3, as do Rouch *et al.* and Fiorina *et al.* based on average core temperatures of 973 K [12] [30] [32]. Equations provided were $\rho = 4094 - (8.82 \times 10^{-1}) \cdot (T[K] - 1008)$ and and $\rho = 4983.56 - 0.882 \cdot (T[K])$, for those two papers, respectively. The density specified by Das *et al.* was lower $\rho = (4176.8 \pm 5) - (1.08 \pm 0.005) \cdot T[K] \pm 1$, and it was only applicable from 843 K to 943 K, with a maximum value of 3244 kg/m^3 at 873 K [38]. Kamp had a value of 4094 kg/m^3 at 973 K based on $\rho = 4094 - (8.82 \times 10^{-4}) \cdot (T - 1008)$, which was also used by Merle *et al.* [14][33] . It is apparent that the equation used by Kamp and Merle *et al.* is much less sensitive to changes in temperature. This approximate range from 3100 kg/m^3 to 4200 kg/m^3 found across all papers reviewed indicates uncertainty in the values. Density selection and the implications are discussed in Section 5.2.3.

4.4.3. VISCOSITY

The dynamic viscosity of LiF (77.5% mol) - ThF_4 (20.0% mol) - $^{233}UF_4$ (2.5% mol) was identified with variations in the reviewed literature. Bajpai *et al.* provided a value of 0.01016 Pa-s, similar to that identified by Cervi *et al.* (0.01 Pa-s), Kamp (0.011 Pa-s), Merle *et al.* (0.00907 Pa-s), and Rouch *et al.* (0.01015 Pa-s) [14][26][28][33][32]. Each of these values were provided with reactor core temperatures in the range of 950 K - 1000 K. Das *et al.* calculated considerably lower dynamic viscosity values based on a range of temperatures. They identified a range of approximately 0.0045 Pa-s to 0.0053 Pa-s over temperatures from approximately 875 K to 925 K, where viscosity decreases based on an increase to temperature [38]. As this is an outlier compared to the other work reviewed, and the temperature ranges of the previously

cited dynamic viscosity values around 0.01 Pa-s, the value from Das *et al.* is not considered in this report. It is also noted that while viscosity changes with temperature, the application of a single viscosity in the mentioned reports is repeated in this work due to the relatively small temperature range being worked with and the corresponding impact on viscosity not being expected to considerably change the results.

4.4.4. VELOCITY

The literature review involved identification of velocities that would be expected at the inlet and outlet of the heat exchanger, and the average reactor velocity. Cervi *et al.* in their study on fuel compressibility specified an average fuel velocity of about 1.2 m/s [26]. In modelling MSFR transient behaviour, Fiorina *et al.* selected 2.78 m/s as the heat exchanger salt velocity on the primary side [30]. Kamp's work showed an average flow magnitude of 3.2 m/s when entering the core, compared to 5.2 m/s when immediately at the inlet and outlet of the heat exchanger [33]. In the work by Rouch, the 2-D model had an inlet velocity of 1.577 m/s [32]. Bajpai *et al.* also provided a contour plot of the velocity field in the core, which had approximate values of 4 m/s at the inlet and outlet of the heat exchanger, and ranged from 0.5 m/s to 3 m/s throughout the rest of the core [28]. Caruggi *et al.* also provided a contour plot with the liquid velocity ranging around 2-4 m/s on the heat exchanger outlet and inlet [29]. It is noted that velocity can vary significantly between reactor designs.

4.4.5. FLOW CHARACTERISTICS

Existing work was reviewed to determine the flow regime that would apply in this scenario. Aufiero *et al.* specifies the flow is turbulent under a k-epsilon model [12]. Cervi *et al.* calculated a Reynolds number in the order of 10^6 based on the average fuel density, average velocity, reactor diameter, and dynamic viscosity, which is well above the threshold for turbulent flow for a Newtonian fluid like molten salt ($Re > \approx 4000$) [26]. Kamp calculated a lower Reynolds number at 196,039 [33] based on a considerably smaller characteristic length in the outlet of the heat exchanger. Fiorina *et al.* identified a much lower Reynolds number of 4600 on the primary side of the heat exchanger [30]. These findings indicate that the molten salt flow will remain turbulent at all locations within the reactor.

4.4.6. TEMPERATURE AND PRESSURE

Due to the large number of sources identified with referenced temperature values, Table 4.1 specifies the temperatures identified in each of the sources. Values not identified in the respective source are indicated with a dash. It is apparent from Table 4.1 that reasonable targets for the core inlet and outlet temperatures are 923 K and 1023 K, respectively, with an average core temperature of 973 K.

Table 4.1 Temperature Values for MSFRs

Authors	**Reference**	**Core Inlet Temp. (K)**	**Core Outlet Temp. (K)**	**Avg. Core Temp. (K)**
Aufiero *et al.*	[12]	923	1023	973
Bajpai *et al.*	[28]	923	1023	-
Cervi *et al.*	[26]	923	1023	973
Cervi *et al.*	[27]	923	1023	-
Fiorina *et al.*	[30]	923	1023	-
Gérardin *et al.*	[31]	-	-	998
Gérardin *et al.*	[39]	-	-	998
Kamp	[33]	950	1021	-
Merle *et al.*	[14]	950	1021	-
Rouch *et al.*	[32]	-	-	948
Caruggi *et al.*	[29]	923	1023	-

A key benefit of the MSFR is that it operates at much lower pressure than conventional water cooled reactors. While Fiorina *et al* and Kamp refer to atmospheric or near atmospheric operating pressure of an MSFR, Cervi *et al.* specify an operating pressure of 2 bar [27][30][33]. It is noted that this is a closed system with an incompressible fluid, so the absolute value of the pressure is replaced by pressure differential in the solution of the Navier-Stokes equations, and the gauge pressure is provided in the simulation results. As such, atmospheric pressure can be specified as the reference pressure, similar to the work performed by Caruggi *et al.* [29]. It is also noted that the thermal power of the core in several cases is specified as 3000 MW, including by Aufiero *et al.*, Bajpai *et al.*, Cervi *et al.*, Fiorina *et al.*, Gerardin *et al.*, Merle *et al.*, and Caruggi *et al.* [12][14][26][28][29][30][31].

4.4.7. OTHER PERTINENT CHARACTERISTICS

The molecular weight for the LiF (77.5% mol) - ThF_4 (20.0% mol) - $^{233}UF_4$ (2.5% mol) salt composition is calculated by Das *et al.* as $M_w = 25.939 + 282.093 \cdot xThF_4 + 288.084 \cdot xUF_4$, where x is the percentage concentration of the molecule by number [38]. This equates to 89.56 g/mol. While no other sources

specify this, it is the standard method for calculating molecular weight.

Fiorina *et al.* use the formula $c_p = -1111 + 2.78 \cdot (T[K])$ J/kg-K for the specific heat capacity, which translates to 1594 J/kg-K at 973 K [30]. This same formula was used by Kamp and Rouch *et al.*, and a modified version was used by Merle *et al.* [14][32][33]. Capelli used a formula that results in 165.6 J/K-mol, which translates to 1849 J/kg-K based on a molar mass of 0.08956 kg/mol for the LiF (77.5% mol) - ThF_4 (20.0% mol) - $^{233}UF_4$ (2.5% mol) salt composition ($c_p = 91.011 + 7.891 \times 10^{-2} \cdot (T[K]) - 341290 \cdot (T[K])^{-2}$ J/kg-K) [40].

The average turbulent Prandtl number of 0.85 was specified by Aufiero *et al.* as being applicable to the whole domain [12]. Fiorina *et al.* also uses the turbulent Prandtl number of 0.85 [30]. Kamp calculates the Prandtl number of Pr = 15.95 based on the salt properties at an operating temperature of 950 K, but this is for laminar flow [33]. For the purposes of this work, it has been demonstrated that turbulent flow will be considered.

Similar to the approach taken with viscosity in which it remains constant across the reactor core and heat exchanger even with the variations in temperature, other properties discussed here are subjected to the same approach based on the small variations expected in the applicable temperature range. The values applicable to the average temperature are selected.

4.5. SOLID PARTICULATE THERMOPHYSICAL PROPERTIES

4.5.1. COMPOSITION

Previous research was performed as a graduate course report regarding solid particulate composites expected to be found within the LiF (77.5% mol) - ThF_4 (20.0% mol) - $^{233}UF_4$ (2.5% mol) MSFR to prioritize next steps for the Joint Research Centre (JRC) Molten Salt Database (MSD). While the JRC MSD had already included some of the most prominent compounds, such as CsF, CsI, LiI, ThI_4, and ZrF_4, that are liquid at the operational temperatures of the MSFR, five more compounds expected in moderate concentrations were identified by Arthurs which are solid above 800 °C: SrF_2, SmF_3, YF_3, NdF_3, and CdF_2 [17]. Other lower profile compounds that would also remain solid and are still expected to occur in lower concentrations include PrF_3, EuF_3, GdF_3, and PmF_4. These compounds are to be used for the basis of the

properties selected for the solid particulate in this work. To determine the proportional impact of these sets of compounds on the average particle sizes and densities, the yield of U-233 fission products is used. For the U-233 fission products, the yields applicable to the fragment mass (atomic number) value ranges are shown by Zhu *et al.* as follows: 88-100 & 132-144 are around 6.5%; 77-88, 100-132 & 144-155 average close to 1% with 110-122 at 0.07%; and outside of those ranges but above 72 and less than 160 average close to 0.01% [41]. Figure 4.3 shows the reference for this information. When those values are translated onto the compounds mentioned, noting that there will of course be significant amounts of Li, Th, and F within the salt to begin with, a reasonable proportional split between the three groups is 60% weighting for the high concentration components (CsF, CsI, LiI, ThI_4, and ZrF_4), 22% for the ones in moderate amounts (SrF_2, SmF_3, YF_3, NdF_3, and CdF_2), and 18% for the lower concentration components (PrF_3, EuF_3, GdF_3, and PmF_4). Since the fission product yield is by number of particles, the particle size and density will be weighted by the specified proprtions as applicable. The melting points for these compounds are listed in Table 4.2, and can be compared to the operational temperatures of the MSFR up to ≈800 °C.

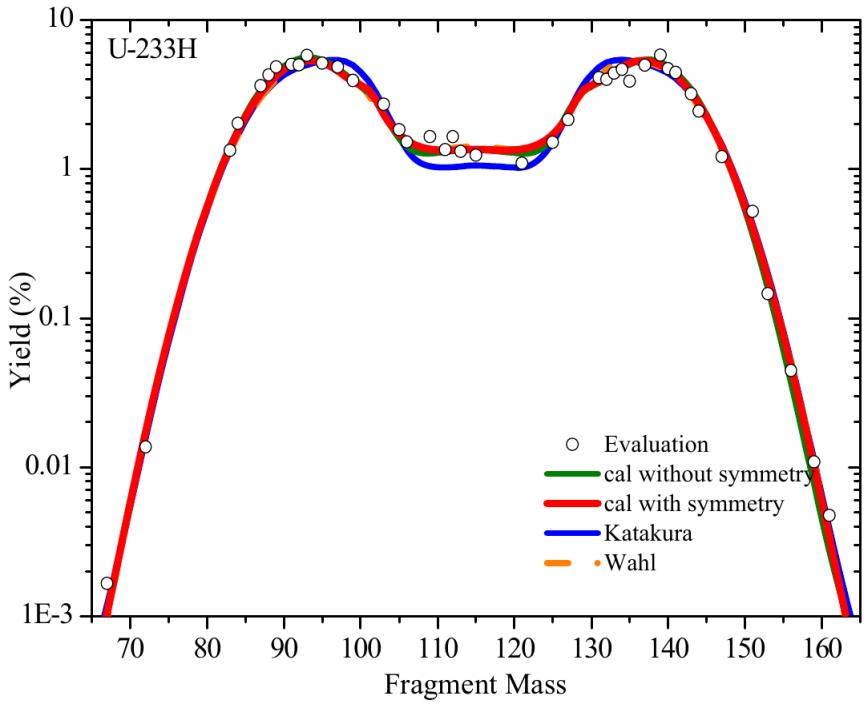

Figure 4.3: Fragment Mass Fission Product Yield from U-233 by 14 MeV Neutrons by Zhu *et al.* [41]

4.5.2. PARTICLE SIZE

The particulate diameter is expected to range from 0.02 mm to 3 mm per Cheng *et al.* in which the hydraulic characteristics of a molten salt pump were assessed with regards to transporting a solid-liquid two phase medium [42]. Poschmann *et al.* review a metal strip that was exposed in the MSRE pump and noted that the smallest particles had diameters at an estimated 100 micrometers, with most being considerably larger [4]. This is consistent with the sizes identified by Cheng *et al.*. Particle sizes used in this work were varied among the different simulations as specified in Table 6.1.

4.5.3. PARTICLE DENSITY

Based on the identified components of the solid particulate, densities range from 4.06 g/cm^3 to 8.2 g/cm^3 per the available information. Table 4.2 lists the known densities for each of the identified composites, recorded at 25 °C and 101.325 kPa unless otherwise noted. In addition, the percent yield of the cation component of the fluorides is specified based on the Japanese Elevated Nuclear Data Library (JENDL) data file from 2011, JENDL-4.0 [43]. Based on the notion that there will be sufficient fluorine for reacting with the fission products, and each of these compounds are fluorides, it is reasonable to assume that the average density of the particulate could be calculated based on the proportions of the fission product yields.

Table 4.2 Densities and Fission Product Yield for Solid Particulates

Compound	**Density (g/cm^3)[44]**	**Yield of Cation from U-233 Fission [a] [43]**
SrF_2	4.24	13.16%
SmF_3	-	0.09%
YF_3	8.20	12.15%
NdF_3	6.51	0.70%
CdF_2	6.33	3.51%
PrF_3	6.30	1.73%
EuF_3	-	0.03%
GdF_2	-	0.01%
PmF_4	-	0.27%

[a] From the fast neutron spectrum at 14 MeV.

Given the compounds for which the densities could not be identified only account for 1.26% of the expected concentration, the other four are used to calculated the average density of the solid particulate. This results in a value of 6.18 g/cm^3. Simulations will be performed for density ranges between the low-

est and highest expected density values based on those identified, resulting in high probability that the impact of densities for the other components will be captured in this work.

4.5.4. CONCENTRATION

The range of applicable concentrations of solid particulate can be determined based on the burnup rate of the fuel that leads to fission products, the percentage of fission products that lead to solid particulate, the mass of fuel in the reactor, and the timelines over which solid particulate could be removed from the core such that steady state concentrations can be approximated.

Constable *et al.* identified that the maximum theoretical burnup of U-235 enriched at 2.7% in a MSR was approximately 155 MWd/kg, which was compared to typical light water reactor burnup rates closer to 50 MWd/kg [45]. Burnup would be expected to be somewhat lower with steady state concentrations of U-233 closer to 0.7% to 0.95% per Betzler *et al.* [46]. That noted, using a constant thermal power of 3000 MW as previously identified, a decrease in the burnup rate would result in an decrease in the concentration fission products of the unit. Betzler *et al.* also listed the duration required to effectively remove fission products from a MSR, and the FP elements of the fluoride components are all listed. They range from 50 days to 3435 days to remove all the content for these compounds [46]. Section 5.2.3 includes a calculation of the expected range of particulate concentration.

4.5.5. OTHER PERTINENT CHARACTERISTICS

The specific heat at constant pressure for the solid compounds were determined using the FactSage 8.0 FactPS pure substances database and are documented in Table 4.3. These were calculated each at 973 K using the ranges and values provided by FactSage. An example calculation is shown below for strontium fluoride (II) where $C_1 = 60.0404$, $p_1 = 0$, $C_2 = 2.30 \times 10^{-2}$, and $p_2 = 1$:

$$C_p = \sum_{i=1}^{8} C_{(i)}\, T^{P(i)} = 60.0404(973)^0 + (2.30 \times 10^{-2})(973)^1 = 82.43\ \mathrm{J/mol \cdot K} \tag{4.1}$$

Table 4.3 Densities and Melting Temperatures for Solid Particulate

Compound	C_1	p_1	C_2	p_2	C_3	p_3	C_4	p_4	**Specific Heat, c_p (J/mol-K)**
SrF_2	94.32	0	-3.85×10^{-2}	1	-1394099	-2	3.095×10^{-5}	2	84.66
SmF_3	-200.5	0	2.14×10^{-1}	1	-99998740	-2	7.0198×10^{-8}	2	113.56
YF_3	111.1	0	-1702000	-2	-86.37	-0.5	-	-	135.84
NdF_3	74.98	0	-3.66×10^{-2}	1	2029240	-2	-	-	112.74
CdF_2	60.04	0	-2.30×10^{-2}	1	-	-	-	-	82.43
PrF_3	152.80	0	-4.88×10^{-3}	1	-1017	-0.5	-	-	115.45
EuF_3	122.61	0	-	-	-	-	-	-	122.61
GdF_2	122	0	-705700	-2	-441.2	-0.5	-	-	107.11
PmF_4[a]	-	-	-	-	-	-	-	-	-

[a] No data was available for PmF_4.

It is noted that while no data was available for PmF_4, Pm accounts for 0.86% of the solid fission product feeder elements and as such has a small overall impact on the average specific heat capacity. Assuming the average heat capacity of the other elements applies for the weighted amount, the average specific heat capacity for these compounds is 106.7 J/mol-K. Using the same proportions as before for the fission product elements for the corresponding solid compounds, the molar masses of these compounds, and the same approach for weighting of PmF_4, the weighted heat capacity is calculated as 750 J/kg-K.

4.6. OPENFOAM APPLICABILITY AND OPTIONS

4.6.1. USE OF OPENFOAM

Several authors of the reviewed work used OpenFOAM in their applications. Specifically, Aufiero *et al.*, Cervi *et al.*, and Caruggi *et al.* used OpenFOAM [12][26][29]. Kamp, Fiorina *et al.*, and Bajpai *et al.* each used COMSOL (a finite element analysis, solver and multiphysics simulation software) [28][30][33]. Rouch *et al.* used FLUENT [32]. In addition, other members of the laboratory to which this work is contributing use OpenFOAM for CFD simulations, and this work can contribute to other related activities.

4.6.2. OPENFOAM SOLVER SELECTION

The solver selected for OpenFOAM simulation work had to support multiphase flows, specifically solid-liquid mixtures with a liquid continuous phase and a solid dispersed phase. Of the standard solvers provided by OpenFOAM, three were reviewed in detail before making a selection: *multiphaseEulerFoam*, *multiphaseInterFoam*, and *DPMFoam* (discrete particle modelling).

For *multiphaseEulerFoam*, the OpenFOAM Foundation describes the solver as one that is to be used in a system where there are multiple compressible fluid phases with common pressure, but have differing properties [47]. That noted, the OpenFOAM Foundation tutorials make use of this solver on the *fluidisedBed* tutorials, in which a fluid (air) continuous phase interacts with a solid particulate phase.

The *multiphaseInterFoam* solver is described in OpenFOAM as a "solver for *n* incompressible fluids which captures the interfaces and includes surface-tension and contact-angle effects for each phase, with optional mesh motion and mesh topology changes." This is similar to *multiphaseEulerFoam*, but it does not capture the dispersion between the liquid phases to the same degree as *multiphaseEulerFoam* [48].

Discrete particle modelling was performed with the Lagrangian solver *DPMFoam*, which is described as "Transient solver for the coupled transport of a single kinematic particle cloud including the effect of the volume fraction of particles on the continuous phase, with optional mesh motion and mesh topology changes" [49]. This proved to require very large amounts of processing power for particle tracking, and as such, was disregarded as an option for this work. *DPMFoam* was replaced in newer OpenFOAM versions with the *denseParticleFoam* solver, but the same demand for resources for similar simulations applied. As noted by Cervi *et al.*, the Euler-Euler method, which treats each phase as having its own uniform properties instead of tracking individual particles, does not demand as much in the way of computational resources compared to Lagrangian-Lagrangian or Eulerian-Lagrangian approaches, making it a good candidate for systems that have high Reynolds numbers (turbulent) and are larger in scale [26]. Shi *et al.* also validated use of Euler-Euler modelling for solid-liquid flow [50]. The MSFR is a turbulent system and the simulations in this work include solid-liquid two phase flow. As *DPMFoam* and *denseParticleFoam* are not Euler-Euler Solvers, other solvers were investigated.

Caruggi *et al.* used the solver *reactingTwoPhaseEulerFoam*, also based on the Euler-Euler approach, for their modelling of gaseous fission products in the MSFR [29]. Cervi *et al.* used the *twoPhaseEulerFoam* for their MSFR work in 2019, where *twoPhaseEulerFoam* is a precursor to the *multiphaseEulerFoam* solver as noted in the OpenFOAM literature which states that the "twoPhaseEulerFoam solver has been replaced by the more general multiphaseEulerFoam solver." [26]. Aufiero *et al.* prepared a model using *buoyantBoussinesqPimpleFoam*, but their focus was on a transient analysis as opposed to multiphase flow [12]. Due to the prevalence of solvers similar to *multiphaseEulerFoam* and successful use in performed simulations, it was ultimately selected as the solver for this work.

4.6.3. TURBULENCE MODEL

There are four methods available for selection in OpenFOAM: Reynolds Averaged Simulation (RAS), Large Eddy Simulation (LES), Detached Eddy Simulation (DES), and Direct Numerical Simulation (DNS) [51]. Each of these have a number of models associated with them. The RAS method is also known as the Reynolds-Averaged Navier-Stokes (RANS) model, which is the simplest and fastest of these methods. It is used to determine behaviour of eddies in a representative manner through averaging calculations over time [52]. Large eddies contain most of the turbulent kinetic energy and have more complex behaviour, and as it does not employ averaging as RANS does, LES is requires considerably more resources to employ [52]. Detached Eddy Simulation is used as an alternative here to minimize resource use in the boundary layer where swirls tend to be computationally demanding [52]. DNS is the most computationally demanding as it captures all velocity fluctuations associated with larger eddies [52]. Kamp used the RANS method in his work, as did Fiorina *et al.*, and Cervi *et al.* cited use of the averaged conservation equations [26][30][33]. As such, the RAS method is employed in the work presented in this report.

There are several turbulence models that can be used for RAS simulations. The realizable k-Epsilon model was used by Aufiero *et al.*, who also used OpenFOAM in the work [12]. The OpenFOAM *realizableKE* model is described as the "realizable k-epsilon turbulence model for incompressible and compressible flows" [53]. For Rouch *et al.*, the RNG (ReNormalization Group) k-epsilon turbulence model was employed to solve the Navier-Stokes equations, however, FLUENT was used in that work as previously noted [32].

The *kEpsilon* model is described as being the standard k-ϵ model applicable to incompressible and compressible flows [53]. For additional context, the k-ϵ model refers to the turbulent kinetic energy (k), and the turbulent dissipation rate (ϵ), where the turbulent dissipation rate is defined as the negative rate of change in the kinetic energy with respect to time [52]. Turbulent kinetic energy tends to decrease with time as kinetic energy is converted from the turbulent eddies into thermal internal energy [33][52]. In the case of the MSFR, as noted by Kamp, the turbulent kinetic energy ranges from approximately 0.017 m^2/s^2 to 0.057 m^2/s^2 depending on the height of the reactor, where the turbulence dissipation rate ranges from 0 m^2/s^2 to 20 m^2/s^2 based on the same height [33]. As the Reynold's number may vary across the reactor based on the decrease in energy and corresponding reduction in velocity, but the use of the pump maintains the average velocity in a range that results in continued turbulent flow in the simulations, as noted in Section 4.4.5.

It is noted that OpenFOAM does have an available *RNGkEpsilon* model, which is described as a "Renormalization group k-epsilon turbulence model for incompressible and compressible flows" [53]. Fiorina *et al.* used the standard k-ϵ model with logarithmic wall functions for calculation of the local turbulent viscosity [30]. Kamp also used the standard k-ϵ model for MSFR simulations [33]. Rodriguez provides guidelines for selecting turbulence models, in which the standard k-ϵ model is good with isotropic flows that have high Reynolds numbers and simple flows, but might have poor results for round jets, strongly curved surfaces, high swirl, flow separation, and low Reynolds number flows [52]. RNG k-ϵ is described as improving upon the standard k-ϵ model through reducing dissipation, which is more beneficial for flows with low Reynolds numbers, separation, and swirls [52]. Finally, realizable k-ϵ is also noted as being useful for separate and swirling flows, but has stability issues [52]. Given this work includes a high *Re*, and is relatively simple, the standard k-ϵ model is employed.

4.6.4. RENDITION OF PHYSICS

Initial conditions used by Caruggi *et al.* followed a uniform temperature distribution across the reactor and fixed pressure gradient across the width of the reactor [29]. The phase fraction of the components were initialized with the same distribution throughout the core [29]. The initial velocity was set to the expected average and the velocity for the walls was set with a no-slip condition [29]. No other sources reviewed provided detail on the initial conditions of the simulations. For boundary conditions, Cervi *et*

al. specified that the structure containing the fluid would be rigid, and used albedo boundary conditions at the top and bottom walls of the reactor which is manifested as axial reflectors [26]. Aufiero *et al.* also used albedo boundary conditions [12]. Rodriguez noted that wall functions can decrease computational demand in RANS models, and Kamp employed their use stating that otherwise a highly refined mesh would be required resulting in longer computing times, and since the velocity at the wall is zero, so are the variables for turbulent kinetic energy and turbulent viscosity [33] [52]. The application of these physical conditions, and all findings of the literature review are applied to the base case simulation as discussed in Chapter 5.

4.6.5. PROGRESS ON RELEVANT WORK

Related work is being carried out by Scuro *et al.* in which OpenFOAM is being coupled with the open source computational thermodynamic software Thermochimica [54]. As of 2022, Scuro *et al.* have successfully performed one-way numerical coupling from OpenFOAM to Thermochimica [54]. In simulating a MSFR as part of the SAMOSAFER project, they obtain data from OpenFOAM associated with the phases and moles being transported at the end of a given time step and transfer that data to Thermochimica in order to calculate the chemical equilibrium and determine how many mols of each relevant phase exist in the molten salt at that time [54]. Future work they will perform includes two-way coupling in which the results of the Thermochimica calculations are provided as inputs to OpenFOAM to support the solutions performed in the next time step [54]. This is related to the work in this report as some phases are expected to occur as solid particulates, meaning this work could provide insights into OpenFOAM configuration that captures flow with solid particulates.

5

SOFTWARE SETUP AND SIMULATION OF SOLID PARTICULATE IN MOLTEN SALT FLOW

This chapter summarizes the physics of the simulation performed as a base case for which a sensitivity analysis was executed related to the behaviour of the solid particulate in the molten salt solution. The details of the cases used for the sensitivity analysis are documented in Chapter 6. In this chapter, the physical phenomena will be summarized, the geometry and mesh for the model used are defined, and the details of the simulation set up in OpenFOAM are provided. The combination of the selected schemes and solvers results in a stable simulation that converges. Those results are presented at the end of this chapter.

5.1. PHYSICS SUMMARY AND COMPUTATIONAL SOLVERS

5.1.1. OVERVIEW

The CFD simulations in this work involve a closed loop system for two-phase flow including liquid salt and solid particulate phases. A model and mesh have been generated to which boundary and initial

conditions have been applied, and properties of the molten salt and the solid particulate have been specified. The model and mesh are described below. The simulation includes the application of a heat source and heat sink to act as the thermal energy from fission and a heat exchanger, where equal amounts of heat energy are added and removed in this adiabatic case (i.e no heat added to or removed from this closed system). A force is applied to the flow near the heat exchanger inlet to act as a pump in the configuration. This section discusses the mathematics involved in the case file and summarizes the functions of the overarching multiphase solver and the specific solvers applied to individual parameters of the simulation.

5.1.2. SOLUTION SCHEMES

The OpenFOAM *fvSchemes* file is used to specify how the integrals will be approximated in the calculations. There are a series of discretization schemes used for the calculation: the temporal *ddtSchemes*, and the spatial *gradSchemes*, *divSchemes*, *laplacianSchemes*, *interpolationSchemes*, and *snGradSchemes*. The *ddtSchemes* is for the differential with respect to time, otherwise known as a time scheme. For this work, the Euler time scheme is used, which is an implicit first order time scheme used for transient applications [55]. Others examples include *CrankNicholson* (second order) and *steadyState* schemes, but Euler was opted for use in this work as it achieved sufficient convergence and was capable of producing results efficiently for a large model with a high number of cells.

For *gradSchemes*, it is the method applied for calculation of gradients of functions. The *Gauss linear* option was selected, which calculates the gradient using Gauss' theorem [56]:

$$\int_V (\nabla \cdot \mathrm{u}) \mathrm{dV} = \oint_S (\mathbf{n} \cdot \mathbf{u}) \mathrm{dS} \tag{5.1}$$

Where $\nabla \cdot \mathrm{u}$ is the divergence of velocity, V is volume of the cell to which the calculation is performed, $\mathbf{n}$ is the outward pointing normal at points along the volume boundary, $\mathbf{u}$ is the velocity vector, and S is the surface area of the volume boundary. The linear interpolation scheme is also applied.

There are also the divergence schemes (*divSchemes*), which capture the net rate of change for a certain property into or out of cells used to predict the properties applicable to the cell at the next time step. The

Gauss divergence theorem is applied for all solution schemes used in this work with varying interpolation schemes.

$$\int_V \nabla \cdot (\vec{u}\vec{u}) dV = \oint_S \vec{u}\vec{u} \cdot dS \tag{5.2}$$

The *limitedLinearV*, *vanLeer*, and *linear* interpolation schemes are used, where the schemes are compared in Figure 5.1. The linear interpolation scheme is a standard calculation of a point along a line. The limited linear interpolation scheme tends towards linear in areas with a slowly changing gradient, but has a bias toward upwind regions of the flow and is limited when a gradient exists that is changing quickly [57]. VanLeer is limiting as well, but not as intensely as limited linear as depicted in Figure 5.1[57]. Note that for *limitedLinearV*, it is an improved version of *limitedLinear* meant to apply to vector fields.

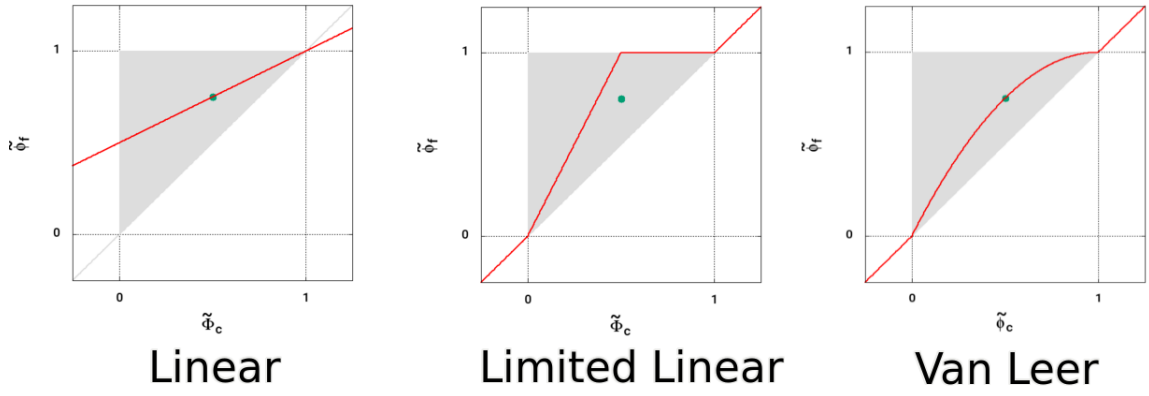

Figure 5.1: Divergence Schemes [58][59][60]

The *Gauss vanLeer* approach is used for the integral of the divergence of the volume phase fraction. This is because the scheme is second-order accurate and can handle the sharp gradients that would be expected in two-phase flow. The internal energy (e), enthalpy (h), kinetic energy (K), and pressure (p) use *Gauss limitedLinear* as they are scalars, and are expected to vary less between nearby cells than phase fraction. The *Gauss limitedLinear* divergence scheme is more suitable to these lower gradient cases. The *Gauss limitedLinearV* approach is used for velocity because it is a vector field. *Gauss linear* is used for viscosity scheme, in addition to the granular temperature of the particles (θ) and the turbulent kinetic energy of the salt (κ) as there is very little change between cells for these parameters. The

Laplacian schemes are used to approximate the Laplacian integrals. The Gauss divergence theorem is applied here, which uses a surface integral of a dot product of a gradient and a surface normal vector, necessitating the use of an interpolation scheme and a surface normal gradient scheme. All cases in this report use the *Gauss linear uncorrected* option as the default for Laplacian schemes. For surface-normal gradient schemes (*snGradSchemes*), the default *uncorrected* scheme is simply applied. The application for *snGradSchemes* is to address non-orthogonality, which for this work, is already very low as specified in section 5.2.2. This allows the *uncorrected* scheme to be used. In reference to the Laplacian scheme and surface normal gradient schemes, they are set as uncorrected by default in this solver as it has been found to be computationally efficient and the results remain satisfactory under the conditions of this report.

5.1.3. SOLVERS

The *multiphaseEulerFoam* solver is described in the OpenFOAM documentation as being capable of representing multiple species, where it also address the physical interactions between different phases [47]. The justification for its selection for application in this work was outlined in Chapter 4.

Within the *fvSolution* file, specific solvers are used for the various parameters. The Preconditioned Bi-Conjugate Gradient Stabilized method (*PBiCGStab*) is used for the volume phase fraction (α), the granular temperature (θ), the turbulent kinetic energy, the turbulence dissipation rate (ϵ), and the turbulence specific dissipation rate (ω). *PBiCGStab* is used for the solution of nonsymmetric linear systems which can help reduce the processing power and time required to perform simulations [61].

The Geometric Agglomerated Algebraic Multigrid (*GAMG*) solver is used for the alternative pressure (p'), referred to in OpenFOAM solver applications as *p-rgh*. The *GAMG* solver can be used for symmetric or asymmetric matrices and has a run-time selectable smoother [62]. For the velocity (U), enthalpy (h), and internal energy (e), a smooth solver is used. Similar to GAMG, it can be used for symmetric or asymmetric matrices and has a run-time selectable smoother [63]. The combination of these solvers has resulted in a converging simulation and is aligned with similar CFD work performed or OpenFOAM tutorials with similar applications.

5.2. SIMULATION DETAILS

5.2.1. MODEL

The model design used for this work is based on dimensions approximated from the MSFR dimensions specified in the literature review for 2-D block simulations, but following a more realistic geometry similar to that found in the work by Caruggi *et al.* [29]. Figure 5.2 outlines the dimensions in metres used in the 2-D model for this work, which was generated in ANSYS Workbench DesignModeler, depicting a cross sectional view of a primary circuit MSFR loop. The left hand side is where the heat exchanger and pump would exist, cycling the salt through the right hand side which represents the core. Section 4.2 specifies the values for the other MSFR dimensions and Figure 4.1 includes the basis for the model.

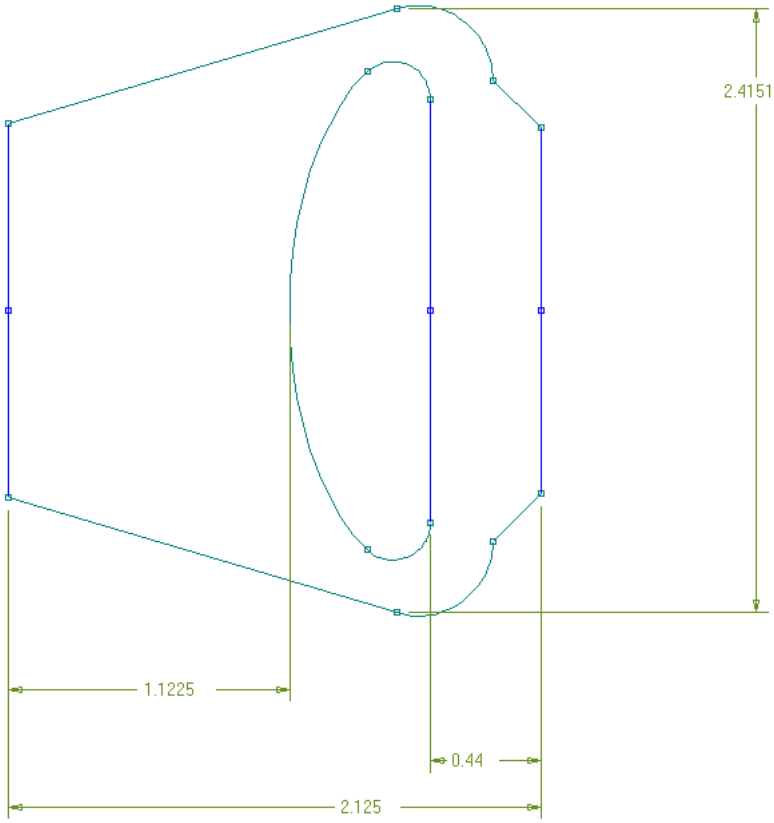

Figure 5.2: MSFR Model Dimensions

The dimensions align closely to the models identified in Section 4.2, using the largest height and width for the reactor based on the fact that the majority of the 2-D simulations use a plain rectangular prism as shown in Figure 4.2, but this model followed a more realistic slice of the MSFR which reduces the height

toward the centre of the reactor, reducing total surface area in a 2-D model. Given the use of the largest reference height and width for the outer edges of the core, the average height and width of this reaction are similar to the average model reviewed. In addition, the heat exchanger width is greater, about double the average, based on the fact the more realistic model has a wider overall heat exchanger as taken from the 3-D model from Caruggi *et al.* [29].

5.2.2. MESH

The mesh was generated to have in the range of 30,000 to 40,000 cells based on the notes from Fiorina *et al.* and Caruggi *et al.* [30][29]. Figure 5.3 shows the mesh created for this work, which has 34,848 cells. The mesh was generated in ANSYS Workbench consistent of a single division along the z-axis for the 2-D mesh, and the remaining cells were set to an element size of 0.01 m.

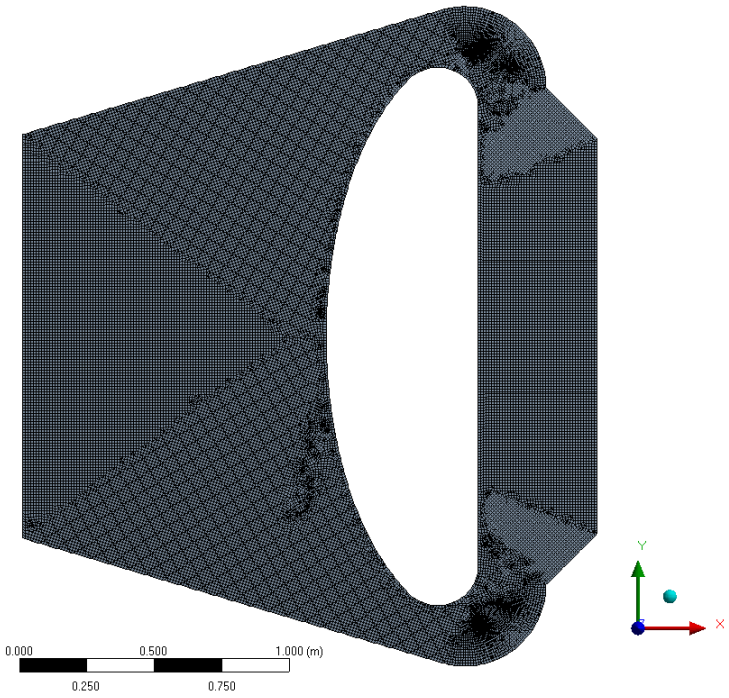

Figure 5.3: MSFR Mesh of 34,848 Cells

With regards to mesh quality, 34,812 of the cells were hexahedra in shape with prisms for the remaining 36. Skewness, which is the ratio of maximum and minimum corner angles within a cell, is a measure of mesh quality where low skewness is better. The average skewness was 2.8×10^{-2}, with a maximum of 0.67 and a minimum of 1.3×10^{-10}. The skewness has a standard deviation of 7.5×10^{-2}. As skewness in

the range of 0-0.25 is excellent quality, skewness is not an issue in this instance [64]. The average corner angle is 92.3°. While there is a maximum of 149.3°, the standard deviation is 6.2°, indicating that the vast majority (in the range of 31,500) of the cells have angles between 82° and 99°, which is the optimal corner angle for quadrilateral meshes [65]. The average orthogonal quality was 0.995 with a maximum of 1 and a standard deviation of 2×10^{-2}. Where 0.95 - 1.00 is excellent orthogonal quality, it is confirmed there is very low non-orthogonality in this mesh [64]. This allows the uncorrected discretization scheme to be used for the surface-normal gradient schemes (*snGradSchemes* that address non-orthogonality) as described in Section 5.1.2.

For this 2-D mesh, a depth equal to the selected cell size of 0.01 m was selected during the modelling phase to provide accurate data with regards to aspect ratio where a deeper model would skew the results. The average aspect ratio is 1.09, with a standard deviation of 0.25, indicating high levels of consistency among the cells. The minimum aspect ratio is 1, as expected given the depth, and the maximum is 8.15. With approximately 33,800 cells in the range of 1 to 2 for the aspect ratio, and less than 100 being desirable, aspect ratio quality is good [65]. There is no concern with regards to element shapes degrading the quality of the simulation results.

5.2.3. CASE SETUP

MOLTEN SALT

Properties of the molten salt fluid were determined based on the findings from the literature review. Table 5.1 outlines the parameters of the molten salt. Selected values reflect the most recurrent or consistent values seen among other work per Chapter 4. The wide range in density values observed in the literature means there is uncertainty and error in the calculations based on the selected value. 4125 kg/m^3 was selected based on its prevalence among literature and close proximity to other identified values.

Table 5.1 Physical Properties of the MSFR

Property	**Value**
Fuel Composition	LiF (77.5% mol) - ThF_4 (20.0% mol) - $^{233}UF_4$ (2.5% mol)
Density	4125 kg/m^3
Viscosity	0.01 Pa·s
Core Inlet Temperature	923 K
Core Outlet Temperature	1023 K
Avg. Core Temperature	973 K
Inlet Velocity	3.3 m/s
Outlet Velocity	3.3 m/s
Avg. Velocity	2 m/s
Initial Pressure (abs.)	1 atm (101.3 kPa)
Molecular Weight	89.56 g/mol
Specific Heat Capacity	1594 J/kg-K
Pr	0.85
Turbulent Kinetic Energy	0.037 m^2/s^2
Turbulence Dissipation Rate	10 m^2/s^2

The values for density, viscosity, pressure, molecular weight, specific heat capacity, Prandtl number, turbulent kinetic energy, and turbulence dissipation rate are simply input as elements in the OpenFOAM case files. The velocity and temperature are controlled through defining sets of cells (using the *topoSet* dictionary) that act as sources of thermal energy and acceleration, and specifying how energy is added through the *fvModels* ference file. The thermal energy is added and removed through use of a *massSource* which can add enthalpy to the cells. Figure 5.4 outlines the cells defined as the heat source and the heat exchanger, where Section A is the generation field and Section B is the sink.

The fluid is accelerated through creation of a virtual "pump" where cells near the bottom of the heat exchanger (i.e. near the inlet) have a force applied to them. The selected cells are shown in Figure 5.4, showing Section C as the pump. To ensure accurate calculations, the maximum Courant number was calculated and specified in OpenFOAM using the average velocity of 2 m/s, the base time step of 2×10^{-3} seconds, and the characteristic length of a given cell at 0.01 m. This is shown in equation 5.3. It is noted that this is a low maximum Courant number for this type of simulation. The reasoning behind this is explained in Section 5.2.5.

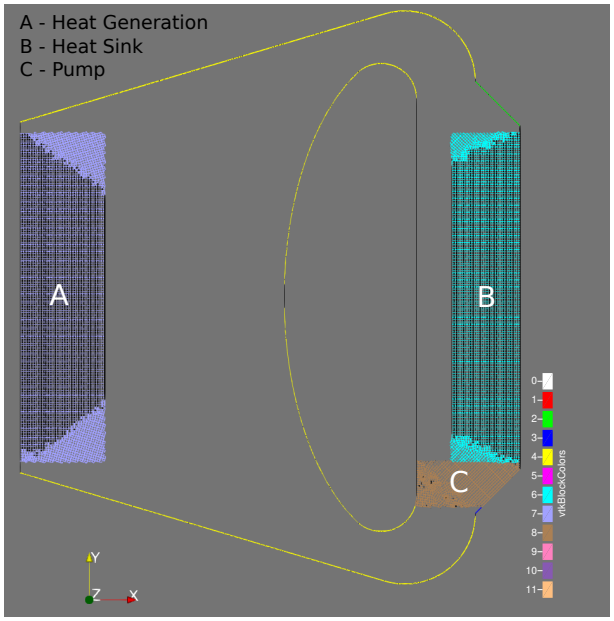

Figure 5.4: Cells Selected to which Heat Generation, Heat Removal, and Force is Applied to Act as a Fission Source, Heat Exchanger, and Pump

$$C = \frac{U \cdot \Delta t}{\Delta h} = \frac{(2\text{m/s})(2 \times 10^{-3}\text{s})}{0.01\text{m}} = 0.4 \tag{5.3}$$

SOLID PARTICULATE

Using the values associated with burnup and fission product removal identified in Section 4.5.4, the values for core dimensions per Section 4.2, fuel and solid fission product densities, a sample calculation of solid fission product concentration is provided, where Table 5.2 lists the results. Using a burnup value of 100 MWd/kg to achieve somewhat more realistic values for the concentration of solid particulate over time, the mass output of all fission products per day is roughly calculated as follows:

$$\dot{m}_{FP} = \frac{3000MW}{100MWd/kg} = 30kg/d \tag{5.4}$$

Then, using the sum of the fission product yield from U-233 fission for the cation elements of the compounds listed in Table 4.2, which sums to 31.66% of the fission products, this is loosely translated to 9.5 kg/day, most of which will combine with fluorine to generate the fluorides. While this value is roughly calculated, it is used to obtain an approximation of the solid content as no experimental data exists to validate what would occur. Since fluorine will generally contribute a much smaller portion to the density

of the compounds, this value is taken as the daily mass output of solid fission products.

Using dimensions from Bajpai *et al.*, which are close to those of other papers reviewed, the approximate volume of the salt in the core can be calculated. This is calculated through determining the volume of the cylinder and then subtracting the approximate "ring" representing the fertile blanket and neutron absorber that creates a gap between the core and heat exchanger.

$$A_{reactor} = \pi r_{reactor}^2 = \pi(2.064m)^2 = 13.4m^2 \tag{5.5}$$

$$A_{blanket} = \pi r_{blanket}^2 - \pi r_{core}^2 = \pi(1.827m)^2 - \pi(1.127m)^2 = 6.50m^2 \tag{5.6}$$

$$V_{reactor} = A_{reactor} \times h_{reactor} = 13.4m^2 \times 2(0.1875m) = 5.02m^3 \tag{5.7}$$

$$V_{blanket} = A_{blanket} \times h_{blanket} = 6.50m^2 \times 1.88m = 12.94m^3 \tag{5.8}$$

$$V_{effective} = V_{reactor} + V_{blanket} = 5.02m^3 + 12.94m^3 = 17.96m^3 \tag{5.9}$$

The fuel density is calculated as follows, where density values are sourced from the CRC Handbook of Chemistry and Physics [44]:

$$\rho_{fuel} = \rho_{LiF} \cdot (77.5\%) + \rho_{ThF_4} \cdot (20.0\%) + \rho_{UF_4} \cdot (2.5\%)$$

$$\rho_{fuel} = (2.64\ \mathrm{g/cm^3})(0.775) + (6.10\ \mathrm{g/cm^3})(0.20) + (5.09\ \mathrm{g/cm^3})(0.025)$$

$$\rho_{fuel} = 3.393\ \mathrm{g/cm^3} \tag{5.10}$$

With an average fuel density of 3393.25 kg/m^3, the fuel mass is determined to be 60,900 kg with the previously calculated volume.

To approximate the quantity of particulate in the core, the times at which low, average, and high particulate concentration would occur need to be determined. As different compounds will be produced at varying rates, an effective time ($t_{effective}$) can be assigned to a certain time that captures the blended rate of solid particulate production. The *cycle time* for certain elements or compounds containing them is defined as the expected time at which they would be removed from the core by recirculating a portion of the flow through a processing plant [46]. The rare earth elements include Yttrium, Praseodymium,

Neodymium, Promethium, Samarium, and Gadolinium with a 50 day cycle time, and Europium with a 500 day cycle time. Cadmium is the only seminoble metal with a 200 day cycle time, and Strontium is marked for discard with the 3435 day cycle time [46]. These cycle times are halved to select four times at which the concentrations of solid particulate can be calculated (25 days, 100 days, 250 days, and 1717.5 days). In addition, it is noted that with the two groups of rare earth metals, the first creates 47.27% of the solid particulate, the second only 0.10%. The seminoble metal (Cadmium) feeds into 11.09%, and the strontium feeds into 41.55%. These are listed in Table 5.2. An example concentration calculation at 25 days (effective time) is provided:

$$t_{effective} = [(0.473)(\frac{25d}{50d}) + (0.111)(\frac{200d-50d}{200d}) + (0.001)(\frac{500d-50d}{500d}) + (0.415)(\frac{3435d-50d}{3435d})] \times 25d$$
$$t_{effective} = 18.25d \tag{5.11}$$

This effective time of 18.25 d is then multiplied by the estimated solid FP mass output per day (9.5 kg/day) to obtain the total mass of 173.3 kg after 25 days. This equates to a mass concentration of 0.28% of solid fission product. The same approach is applied to the other three durations as shown in Table 5.2.

Table 5.2 Concentration of Solid Particulate in Molten Salt Over Time

Processing Group	**Cycle Time (d)** [46]	**Calc. Time (d)**	**Group FP Yield**	**Effective Time (d)**	**Solid FP Mass (kg)**	**Mass Concentration (kg/m^3)**
Rare Earth Elements Time 1	50	25	47.27%	18.25	173.3	0.28%
Seminoble Metal Time	200	100	11.09%	44.73	424.9	0.70%
Rare Earth Elements Time 2	500	250	0.10%	88.88	844.1	1.38%
Discard Time	3435	1717.5	41.55%	356.81	3389.0	5.56%

These values can then be translated into volume concentrations using the average density of 6180 kg/m^3 and the core volume of 17.96 m^3 to obtain values of 0.16%, 0.38%, 0.76%, and 3.05% at the times of 25 days, 100 days, 250 days, and 1717.5 days, respectively. As such, an appropriate range of concentrations to apply for these simulations is between 0.15% and 3.5% by volume, with an average closer to a steady state value around 1.0%. This average value, along with other properties of the solid particulate are listed in Table 5.3, which establishes the base case conditions for the simulations performed in this work. The values were determined from the averages of the most common properties identified in the

literature review, noting the proportional nature of the solid productions of fission and transmutation being applied to the properties in a weighted manner. With regards to temperature, pressure, and velocity, the particles are acted upon by the salt and have the same values for these properties.

Table 5.3 Physical Properties of Solid Particulate in the MSFR

Property	**Value**
Density	6180 kg/m^3
Diameter	1.5 mm
Molecular Weight	99 g/mol
Specific Heat Capacity	750.2 J/kg-K
Volumetric Concentration	1%

OpenFOAM calculates effective conductivity of enthalpy as the sum of laminar and turbulent conductivities [66]. The laminar portion is calculated as the dynamic viscosity divided by the Prandtl number. For the solid phase particles, the dynamic viscosity is set to zero, so the Prandtl number can simply be input as 1, resulting in the laminar portion of the effective conductivity of enthalpy being calculated as zero. The liquid phase captures this aspect of the simulation. The density, molecular weight, and specific heat capacity are set via the *thermophysicalProperties* file for the particles. The diameter is set using the *phaseProperties* file, where the volumetric phase fraction is set using the *setFieldsDict* dictionary in the *system* folder, and the field is applied to the full volume where the salt is 99% and the particles are 1%.

OPENFOAM SETUP

OpenFOAM cases are structured with three standard subdirectories: *0/*, *constant/*, and *system/*. The *0/* folder includes the initial conditions for each of the variables for which calculations are performed during the simulation. The *constant/* folder includes the geometry, thermophysical properties, momentum transport properties, and phase properties, in addition to any other constant functions such as field details for heating, cooling, and force addition. The *system/* folder specifies various elements of the simulation through dictionaries. In this case, duration, base time step, and maximum Courant number of the simulation in the *controlDict* dictionary. As noted, the *setFieldsDict* dictionary includes the initial volume phase fraction details. The *fvSchemes* and *fvSolution* files specify the methods used for derivation for the prediction calculations. The *topoSetDict* dictionary specifies cell boundaries used to create other energy sources (e.g. heat generation, force generation) in the simulation.

The *0/* folder contains files for *alpha*, the volumetric phase fraction, specified for both the *particles* and *salt* (the two phases in this simulation). It also contains files for *alphat* (thermal diffusivity), *epsilon* (turbulence dissipation rate), *k.salt* (turbulent kinetic energy), *nut.particles/salt* (turbulent viscosity), *p* (pressure), *p_rgh* (modified/alternative pressure), *T.particles/salt* (temperature), *Theta.particles* (granular temperature), and *U.particles/salt* (velocity). Where the volumetric phase fraction is specified by the *setFieldsDict* mentioned previously, the other initial conditions are specified as per Table 5.4.

Table 5.4 Initial Conditions in OpenFOAM Case

Name	**Property**	**Value**
alphat.particles	Particle Thermal Diffusivity	0 kg/m-s^3 [a]
alphat.salt	Molten Salt Thermal Diffusivity	0 kg/m-s [a]
epsilon.salt	Turbulence Dissipation Rate	0.001 m/s^2
k.salt	Turbulent Kinetic Energy	0.037 m^2/s^2
nut.particles	Particle Viscosity	0 m^2/s[a]
nut.salt	Molten Salt Viscosity	1.8 $\times 10^{-8}$ m^2/s
p	Pressure	1 $\times 10^5$ Pa
p_rgh	Modified/Alternative Pressure	1 $\times 10^5$ Pa
T.particles	Particle Temperature	973 K
T.salt	Molten Salt Temperature	973 K
Theta.particles	Granular Temperature	0 m^2/s^2 [a]
U.particles	Particle Velocity	0 m/s [a]
U.salt	Molten Salt Velocity	0 m/s [a]

[a] The initial value for this parameter is zero as it is always calculated based on other elements of the simulation and does not impact the final value.

The constant folder contains six elements of the simulation: the mesh (*polyMesh/*), specified values for energy sources (*fvModels*), gravity details (*g*), turbulence and momentum properties of the phases (*momentumTransport.**), additional properties of the different phases (*phaseProperties*), and thermophysical properties of the phases (*thermophysicalProperties.**). The *polyMesh/* folder outlines the boundaries and details of the mesh (cells, points, etc.), and the sets specified by the *topoSet* file, where the dimensions for the model were outlined in Figure 5.2 and the topoSet boundaries are shown in Figure 5.4. The *fvModels* file specifies the details of the heat source, heat sink, and momentum source, namely the rate of energy addition and direction and magnitude of the force applied to the regions. The heat source and sink had equal and opposite values of 5.5 $\times 10^6$ W, which was found to yield inlet and outlet temperatures very close to that found in the literature. The pump section had a force of 75 N applied in the negative-y

direction. Test simulations indicated this force resulted in flow velocities that aligned with the literature review. In all three cases, the energy is continuously applied throughout the simulation. The *g* file simply specifies the gravity value and orientation, which was in the negative-y direction for this work. There are two *momentumTransport* files: one for each of the particles and salt phases. These specify that the RAS kEpsilon turbulence model is used. The *phaseProperties* file was used to define the particle diameter (1.5 mm per the literature review), blending method (continuous), drag model (Ergun), and heat transfer type (Ranz Marshall). The *thermophysicalProperties* file defines the molecular weight, density, specific heat capacity, viscosity, and Prandtl number as indicated in Table 5.3.

The system folder is used to define the time elements of the solution, in addition to the solver and schemes, the cell sets identified for the heat source, heat sink, and momentum source, and the initial volume phase fraction of the two phases. The *controlDict* dictionary is used to define the solver used, the start and end times, time step, precision of the data, the maximum courant number, among other data management elements of the simulation. The *fvConstraints* file applies a limit on the pressure so there is a minimum of 1×10^4 Pa. The *fvSchemes* and *fvSolution* file elements are described in Sections 5.1.2 and 5.1.3. The *setFieldsDict* dictionary specifies the initial distribution of particles and salt throughout the mesh. As previously noted, the *topoSetDict* dictionary specifies the range of cells that are used to create the heat source, heat sink, and momentum source.

With this set up complete, the case was run to a converged, steady state condition, with solid particulates dispersed in the molten salt. The convergence was defined primarily based on the residuals of the simulation, as described in Section 5.2.5. The results are documented in Section 5.2.4.

5.2.4. SIMULATION RESULTS

The results of the simulation are summarized for the particulate distribution, heat transfer, and flow behaviours. The intent of this section is to establish the details of a base case scenario with approximate average values for variable properties in the molten salt simulation with particulate. A sensitivity analysis was subsequently performed on the particulate concentration, density, and diameter, where the results are captured in Chapter 6. The instantaneous data provided is taken at steady-state conditions, at 300 seconds into the simulation unless otherwise specified. At times, details at earlier time stamps in

the simulation are provided to explain the behaviour of the salt and particulate flow as the simulation achieves steady-state conditions. The details of convergence time are provided in Section 5.2.5.

PARTICULATE CONCENTRATION

The particles were initially evenly distributed over the mesh, at a 1% concentration by volume. Figure 5.5 shows that the particles collected along the outer edges of the mesh, where the highest concentration was found near the base of the centre of the reactor. The concentration reached nearly 51% by volume at this location at a very localized area, where the average in this peak was closer to 35-40%. This is likely caused by a combination of of gravity, flow coming from along the negative-x axis, and the slip conditions in the core centre representing counteracting forces from the converse loop.

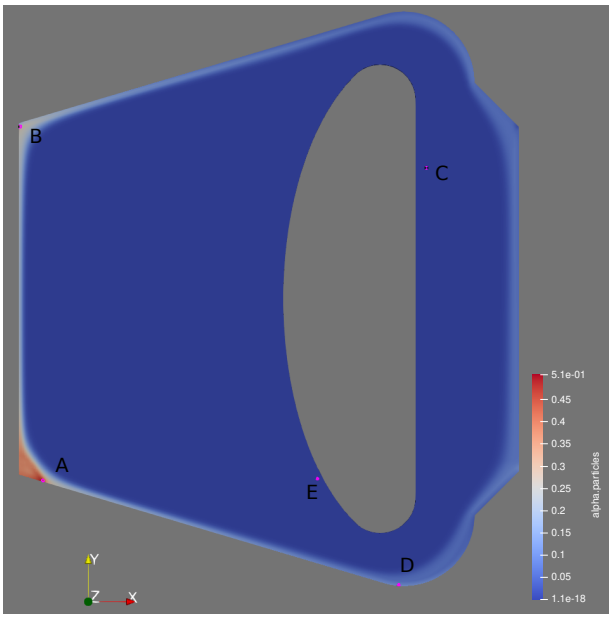

Figure 5.5: Particle Distribution

Figure 5.6 shows the concentration associated with five points in the model as indicated in Figure 5.5. The majority of the body contains negligible particulate content, with a slight increase surrounding the vortex at the outer portion of the core. Point A is where the highest collection of 51.7% by volume occurred. Point B is upper edge of the core centre, where the second highest concentration is seen. Point C is where an increase had been observed earlier in the simulation, but reduced to much less than initial concentration near steady state. Point D captures the concentration near the bottom of the reactor, and Point E is where the lowest concentration occured at the end of the simulation.

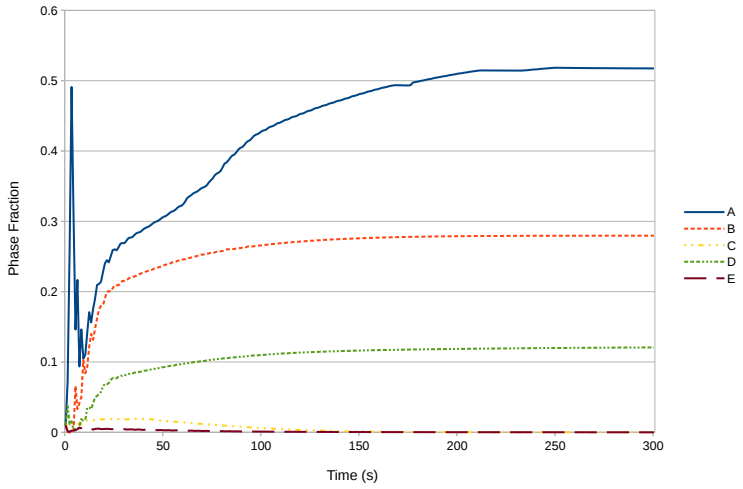

Figure 5.6: Particle Concentration over Time (5 min)

To allow for a focused look at what occurs in the lead up to steady state, a second plot is shown in Figure 5.7 which outlines the first 30 seconds of the simulation. It is apparent that Point A, which has the highest concentration collected at the end of the simulation, had an initial concentration increase and decrease as the fluid flow began and carried the particulate into that central area of the core. However, it is noted that the outputs from the early portion of the simulation are not realistic. The simulation is still converging at this time and and significant changes in the particulate concentration over such short time periods is not physically realistic.

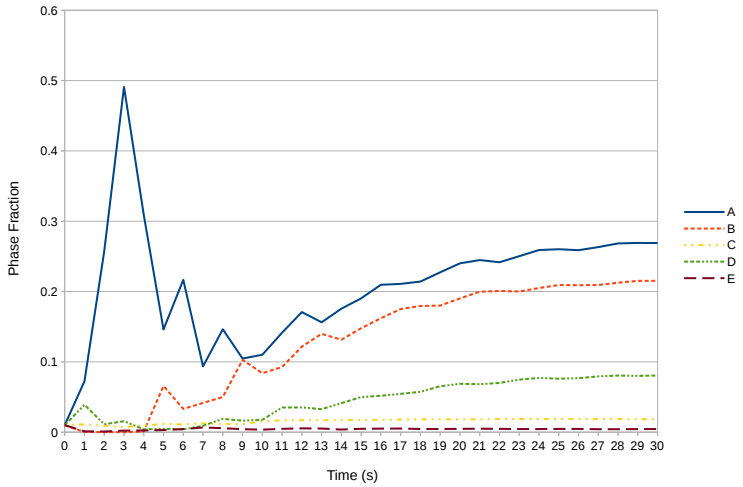

Figure 5.7: Particle Concentration over Time (30 sec)

In addition, another contour plot image was generated where all points with concentrations higher than

the initial concentration of 1% are highlighted, as shown in Figure 5.8. It is further evidence that all the particles collected on the outer edges of the reactor based on the flow profile.

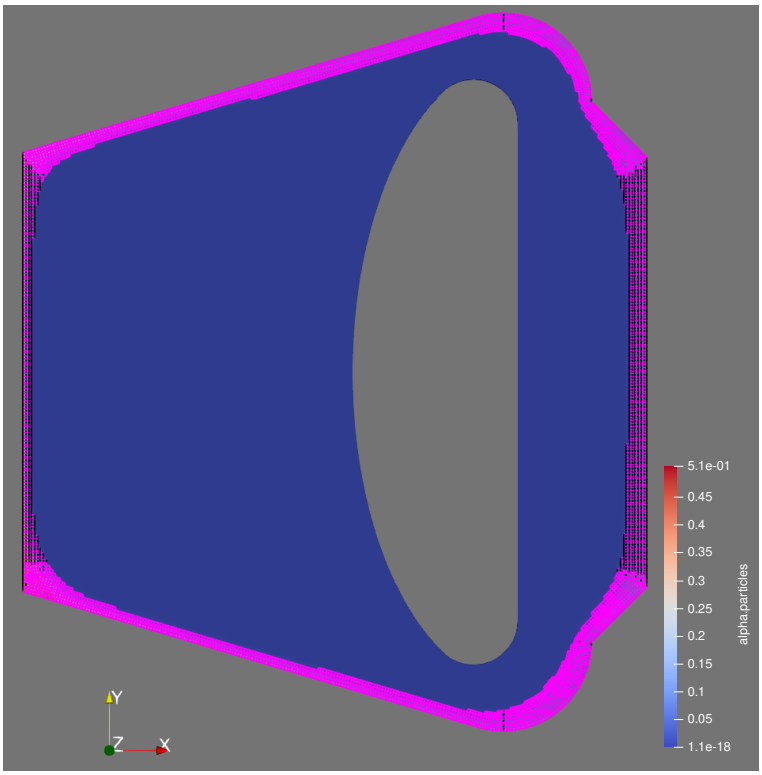

Figure 5.8: Concentrations Above 1% by Volume

TEMPERATURE

The temperature contour plot at 300 seconds can be seen in Figure 5.9. Six point monitors (Points A-F) were selected to be used as comparison points between this base case and the six cases reviewed in Chapter 6: Point A - Core Outlet, Point B - Start of Heat Exchanger, C - End of Heat Exchanger, D - Core Inlet, E - Core Centre, and F - Outer Core. The core inlet temperature is approximately 883 K (Point D), and the outlet temperature is 1021 K (Point A), compared to the literature review values of 923 K and 1023 K, respectively. With a melting temperature of 837 K, the salt is liquid throughout the model where the lowest temperature is above 860 K, but it is noted the margin to freezing is small.

There is an apparent increase in temperature at the bottom of the centre of the reactor prior to entering the zone of heat generation (bottom left hand corner below Point E). Along the upper edge, the particulate does not contain as much thermal energy as the free flow as the boundary temperatures are in the

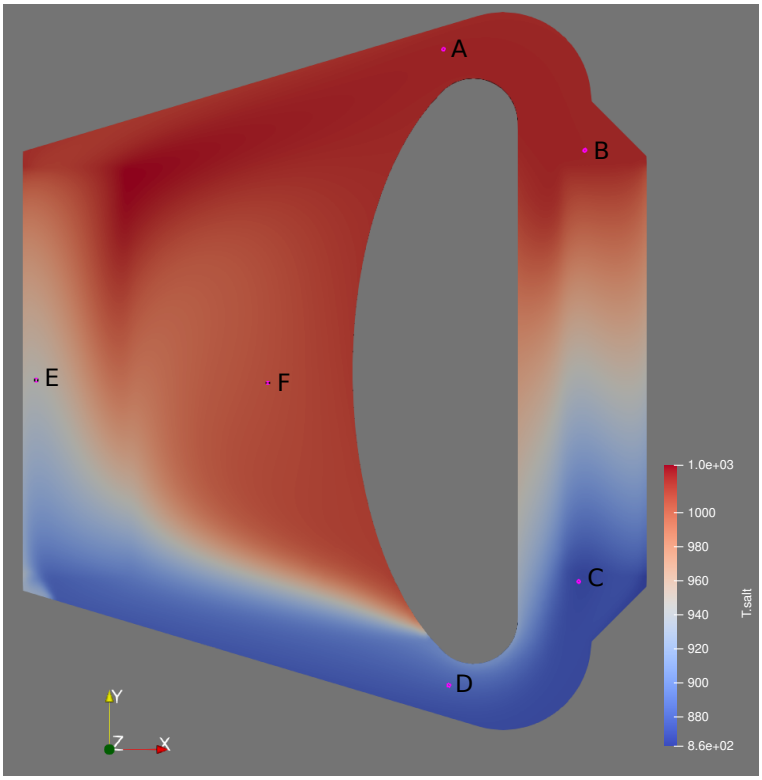

Figure 5.9: Temperature Contour Plot

980 K - 1000 K range compared to the free flow 1020 K to 1025 K range. Figure 5.10 shows point monitor data for six points throughout the duration of the simulation.

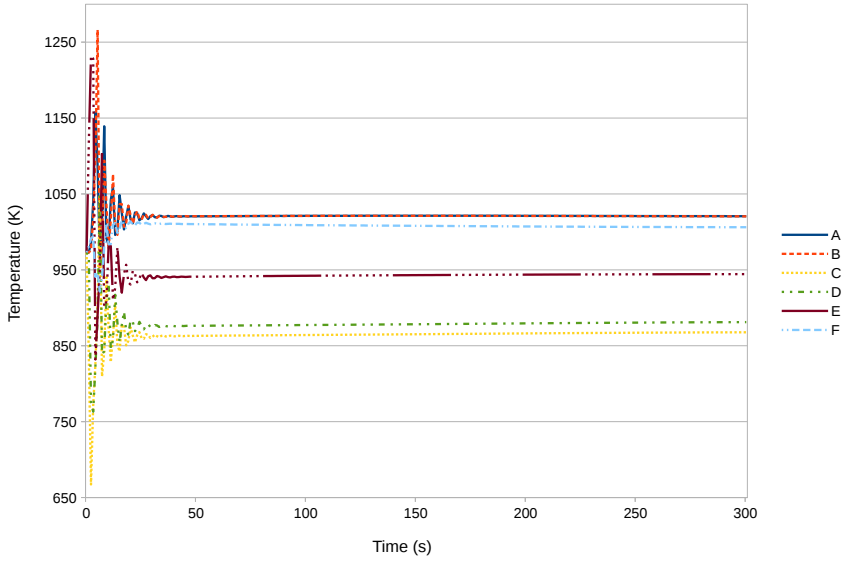

Figure 5.10: Temperature Monitor at Key Points

There are major fluctuations in the temperature at the specified points as the generated heat and heat sink create large temperature differentials before the fluid flow has sufficiently created a mixed environment. As the lower and higher temperature portions of the fluid mix, they achieve a steady state.

VELOCITY

The velocity profile at the end of the simulation is obtained at approximately 5 seconds into the simulation, as indicated in Figure 5.11. The profile allows the heat transfer between the heat sink and core to obtain the steady state conditions.

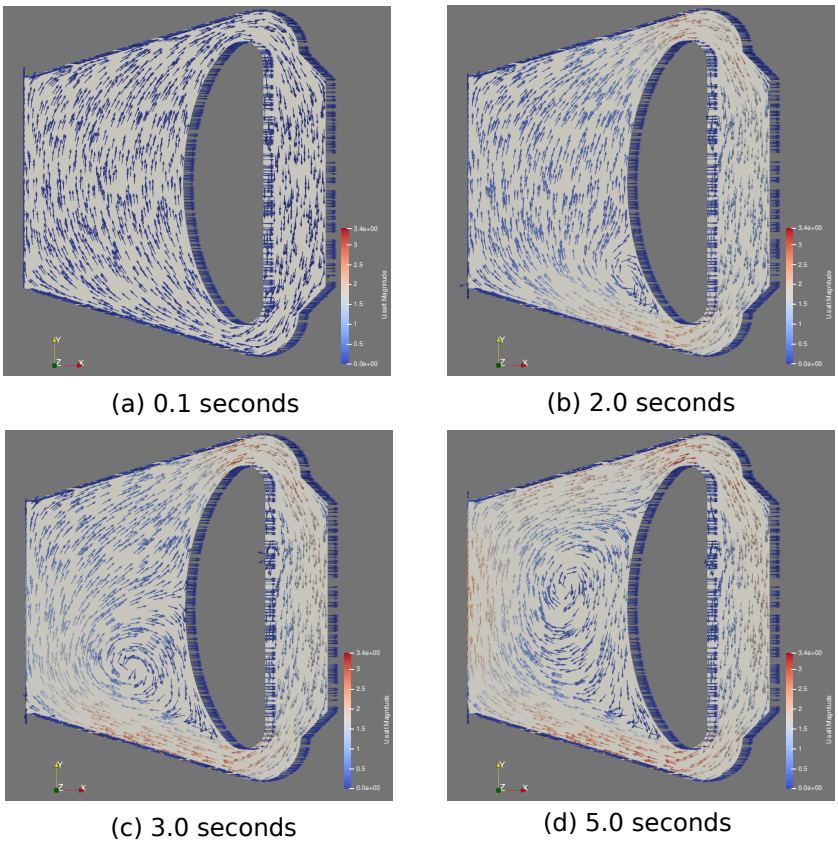

(a) 0.1 seconds (b) 2.0 seconds

(c) 3.0 seconds (d) 5.0 seconds

Figure 5.11: Velocity Profile Progression

The vector plot for velocity is shown in Figure 5.12, where colour indicates magnitude and the direction is given by the vectors on the plot. The flow progresses around the body as expected through the heat exchanger and into the core, where the slip condition at the core centre (seen as the right side boundary) represents the collision and counteracting forces of the flow from the symmetrical circuit as described in Section 4.2. The flow up the centre of the reactor results in a large vortex occurring in the core, but

more toward the outer edge. There is a possible, but marginal impact on the flow by the particulate in the corners where it resides, but generally the particulate collection will be based on the flow itself, the geometry of the model, and the properties of the particulate. The peak velocity is 4.51 m/s at the inlet into the heat exchanger in the upper right corner of the model.

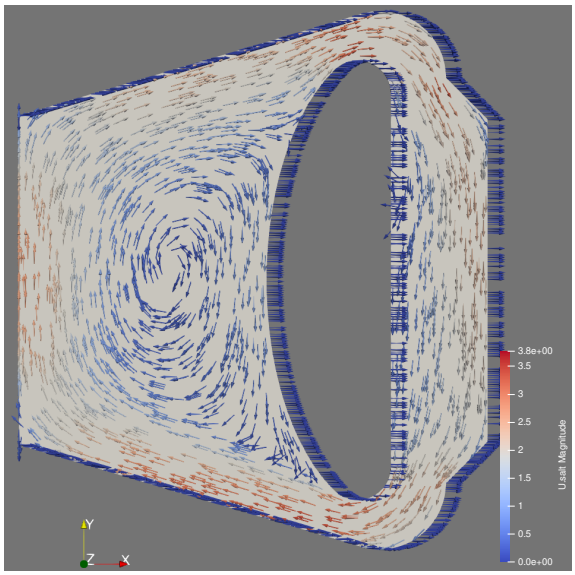

Figure 5.12: Steady State Velocity Vector Plot (300 s)

Figure 5.13 shows the peak and minimum velocity, where the minimum occurs at 0.006 m/s on the inner wall of the heat exchanger. 3.8 m/s appears as the peak as the legend shows point data, not cell data.

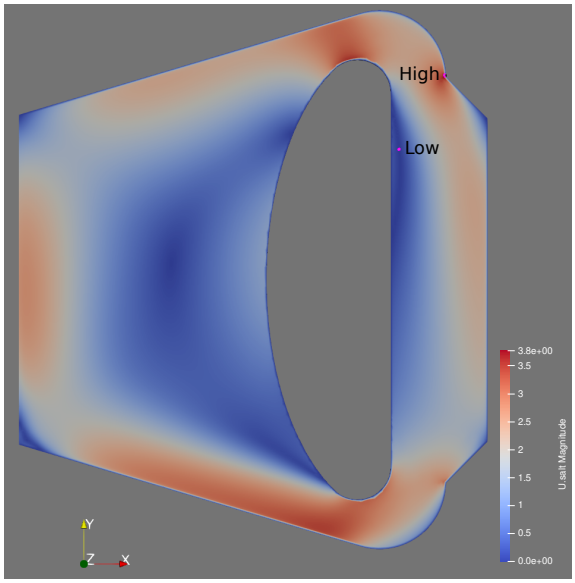

Figure 5.13: Minimum and Maximum Velocity Cells

5.2.5. CONVERGENCE DETAILS

Key contributors to achieving convergence aside from stability in the physics set up include a sufficiently fine mesh and a sufficiently small time step. The mesh quality details are outlined in Section 5.2.2. The time step initially specified for the simulation was 2×10^{-3} s, and a maximum Courant number of 0.4 was selected based on an approximate average velocity of 2 m/s based on the literature review, a characteristic length of 0.01 m for the cell size, and a time step of 2×10^{-3} s. The Courant number is calculated in Equation 5.3. The time step was allowed to be adjusted to maintain the Courant number below 0.4 to ensure sufficient convergence. While the time step of 2 ms was use for the first several steps in the simulation, as velocity increased, the time step reduced to approximately 2×10^{-4} s for the majority of the simulation to maintain the Courant number below the maximum.

Figure 5.14 shows the initial residuals for the granular temperature, phase fraction, particle and salt energy, turbulence dissipation rate of the salt, turbulent kinetic energy of the salt, and the modified/alternative pressure.

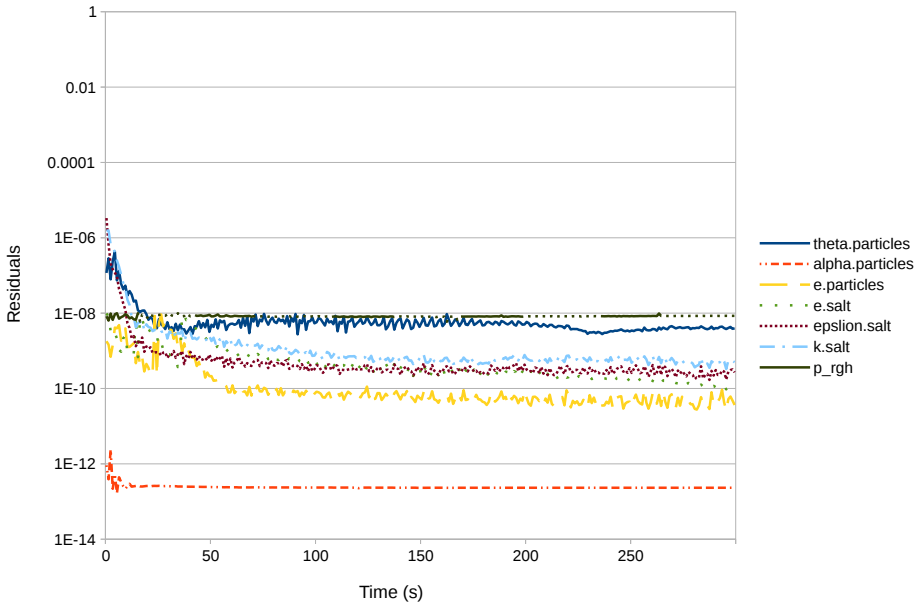

Figure 5.14: Residuals of Key Parameters

In OpenFOAM, residuals are calculated iteratively within each time step. As such, there are "initial" and "final" residuals determined for each parameter at each time step. The initial residual is meant to gauge

stability of the previous iteration. The final residual is the residual when the solver has finished calculations for that time step (i.e. after all iterations are complete), which can be used to gauge convergence of the simulation. Because of this, the final residuals will be considerably lower than the initial residuals. When the maximum Courant number was initially determined for this work, it was calculated based on a time step of 2×10^{-3} s, as a series of test simulations indicated that this time step was required to achieve convergence in the simulations. To determine this, the initial residuals were targeted in the range of 1E-04 to 1E-06. As an indicator of convergence, residuals in the range of 1E-05 demonstrate good convergence, and those close to 1E-06 are tightly converged [67]. Nearing completion of this work, it was identified that the final residual was to be used as an indicator of convergence, and the values observed were closer to 1E-08 to 1E-11 in most simulations performed for this report. Based on this, it is noted that the initial time step and the maximum Courant number could have been increased to reduce resource requirements and/or the duration to complete the simulations. A maximum Courant number could have been in the range of 5 to 10 based on review of additional literature [52]. Since the simulations had already converged very well, the original results were kept and presented in this report.

The continually decreasing trend of the residual calculations leads to the indication that the simulation is converging. Since the residuals are in the range of 1E-08 to 1E-13 for most of the parameters for which the value is calculated, it is apparent that a simulation with low error margins has been carried out. While residuals for values such as temperature and velocity were not directly calculated in the solver, items like the granular temperature, turbulence dissipation rate, and turbulent kinetic energy are drawn from these values, which would require the previously mentioned parameters to have even smaller residuals than those shown here. Given the residuals indicate good convergence, and other parameters remain unchanged based on initial pressure in this incompressible closed system, the sensitivity analysis discussed in Chapter 6 continued based on these results from the base case.

6

SOLID PARTICULATE PARAMETRIC SENSITIVITY ANALYSIS

A parametric sensitivity analysis was performed to assess the impact and influence of solid particulates on molten salt flow. This chapter summarizes the results of the cases in which parameters of the solid particulate were varied. Three parameters were evaluated: Particulate Diameter, Particulate Density, and Initial Particulate Concentration. The upper and lower bounds of expected values were incorporated into the calculations where for each individual variation of the three parameters, a new simulation was performed. This chapter includes the results for the six simulations performed for the sensitivity analysis and comparisons against the base case.

6.1. COMPUTATIONAL DETAILS

6.1.1. GEOMETRIC MODEL & MESH

The model and mesh used for the sensitivity analysis are unchanged from those used for the base case described in Chapter 5. Refer to Sections 5.2.1 and 5.2.2 for details.

6.1.2. CASE SETUP

Table 6.1 shows the case matrix, showing the comparison of the sensitivity analysis cases to the base case (Case 1) outlined in Chapter 5. The cases are ordered such that cases 2 and 3 are for the lower and upper variations in particulate diameter, cases 4 and 5 list the lower and upper bounds for density, and cases 6 and 7 are for the lower and upper bounds on initial particulate concentration. It is noted that for case number 1, the approximate average values were taken for each of these parameters based on the literature review and the other cases are meant to gauge the impact of the extremes of these parameters on the molten salt behaviour. All elements of the simulation not listed in the table remain unchanged from the conditions defined in Chapter 5.

Table 6.1 Variable Scenarios for Simulation of Particle Transport in MSR Core

Case No.	**Particulate Diameter (mm)**	**Density (kg/m^3)**	**Initial Concentration (% vol)**
1	1.5	6180	1.0%
2	0.02	6180	1.0%
3	3.0	6180	1.0%
4	1.5	4240	1.0%
5	1.5	8200	1.0%
6	1.5	6180	0.15%
7	1.5	6180	3.5%

The base case (Case 1), was defined in Chapter 5. The simulation results of the remaining cases are outlined in Section 6.2, where the focus is on what impact the parameter adjustment has on particulate concentration, temperature, and velocity.

6.2. SIMULATION RESULTS

The results presented in this chapter have not been validated with experimental work. Statements made based on the outcomes are only in reference to the predictions made by the simulations.

6.2.1. CASE 2: LOW PARTICULATE DIAMETER

PARTICULATE CONCENTRATION

Points of interest for particulate concentration were determined by selecting those with the highest (Point A) and lowest (Point E) concentrations, points in the second (Point B) and third (Point D) highest areas of concentration, and one point where the concentration initially increased but decreased to a negligible amount by the time steady state was reached (Point C). The points are identified in Figure 6.1.

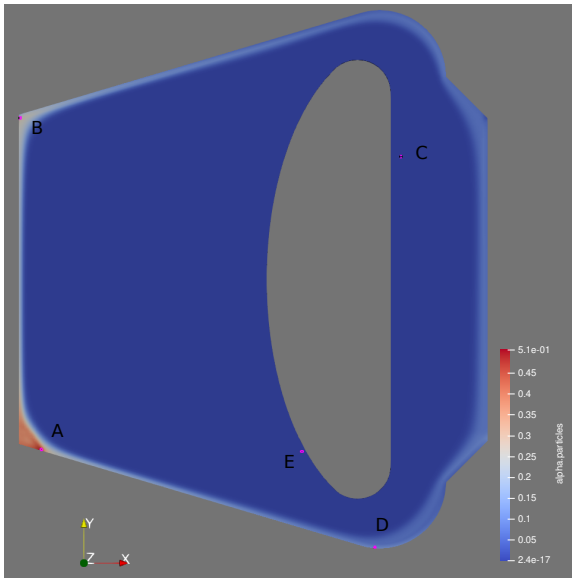

Figure 6.1: Particle Distribution - Case 2

Per Figure 6.2, the highest point of concentration is seen as Point A, which reached a maximum concentration of 52% by volume. While the area with this peak concentration is small, it is a very high concentration of particulates at one location. Point B, located at the top of the core, was selected as the particulates are caught in that location as the centrifugal force of the flow pushes the particulate to the outer edge.

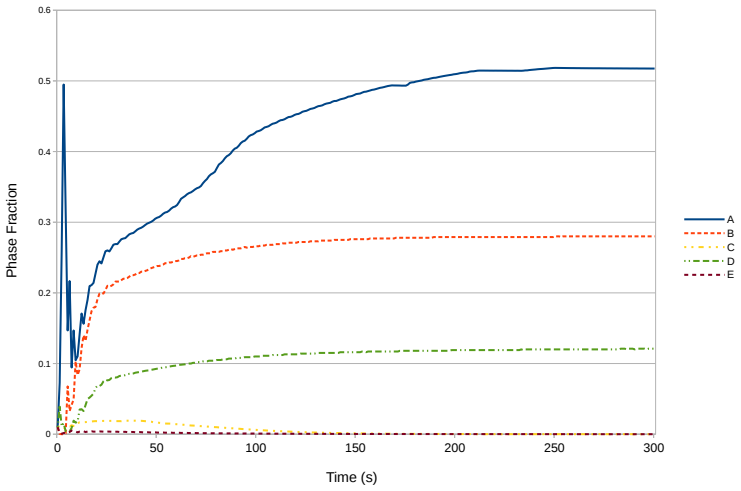

Figure 6.2: Particle Concentration over Time (5 min) - Case 2

There was some collection at Point C as the flow had low impact on that location for a period of about a minute, but the particulate was ultimately dispersed from here. Point D also had a high concentration, around 12%, where a combination of gravitational and centrifugal forces maintained more particulates

at that location. Finally, the lowest concentration was seen at Point E as the "pump" circulated particulates away from this location throughout the entire simulation duration. The same behaviour around particulates collection around the outer edges was seen in this case as in the base case. This is apparent in Figure 6.3.

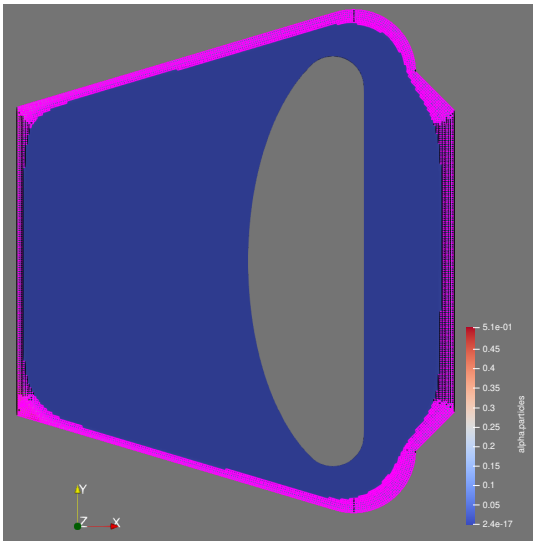

Figure 6.3: Concentrations Above 1% by Volume - Case 2

TEMPERATURE

Data for the same six points as identified in the base case was extracted from this simulation for temperature, where similar results were found. Figure 6.1 shows the contour plot for Case 2.

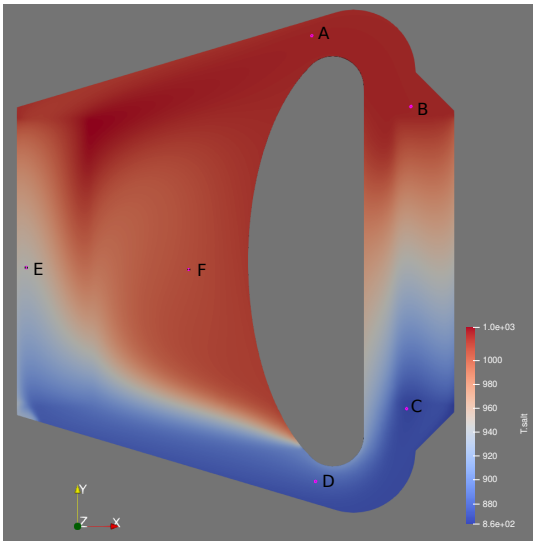

Figure 6.4: Temperature Contour Plot - Case 2

The steady state peak temperature was about 1028 K, with the heat exchanger inlet temperature at 1020 K, which is very close to that of the literature. The heat exchanger outlet temperature remained about 881 K, with the lowest still above the melting temperature of 837 K at 863 K.

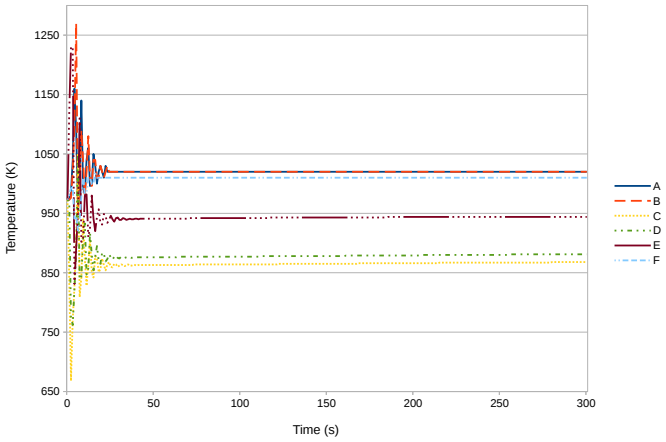

Figure 6.5: Temperature Monitor at Key Points - Case 2

The temperature also reached a steady state at approximately the same time as the base case, at approximately 30 s after the start point, and remained steady for the duration of the simulation. This can be viewed in Figure 6.5.

VELOCITY

The peak velocity of 4.51 m/s occurs near the heat exchanger inlet, similar to the base case.

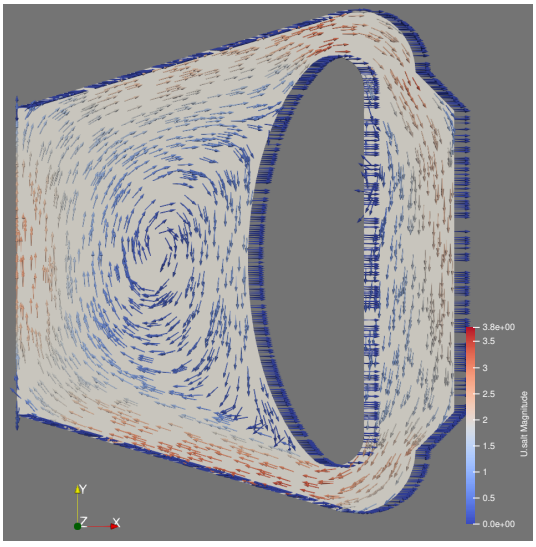

Figure 6.6: Steady State Velocity Vector Plot - Case 2

The pattern continues from the base case in which the flow progresses around the outer edges of the core, with a large vortex in the outer section of the core proper. This is depicted in Figure 6.6. The lowest velocities were seen near the heat exchanger outlet, where the vectors leaving the pump collide with the flow returning from the large vortex in the middle of the model.

RESIDUALS

Residuals remained low for all parameters, indicating good convergence. This is shown in Figure 6.7.

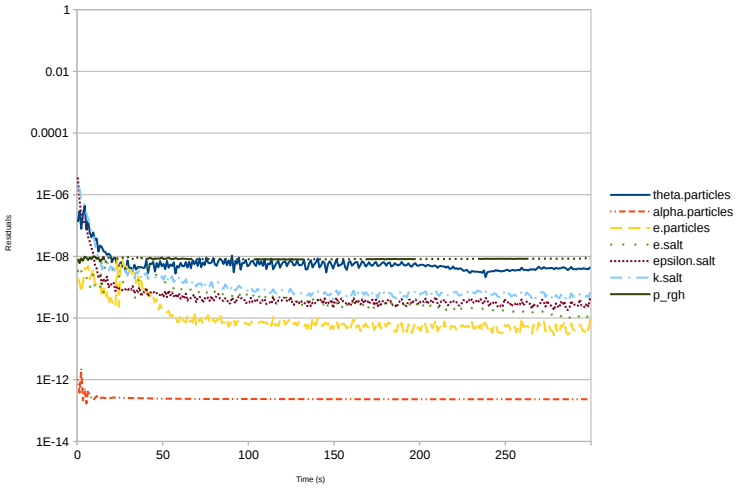

Figure 6.7: Residuals Plot - Case 2

There were some variations on the values, but the trend remained largely the same, where all residuals were in the range of 1×10^{-8} to 1×10^{-13}.

6.2.2. CASE 3: HIGH PARTICULATE DIAMETER

PARTICULATE CONCENTRATION

For the high particulate diameter simulation (Case 3), the maximum particulate concentration of 52% occurred near the bottom of the core centre. Similar to the previous cases, concentration remained around the outer edges of the core. This is apparent in Figures 6.8 and 6.10. Figure 6.9 shows consistency between the previous cases as well for the cells specified about the model.

This level of similarity indicates that the particulate diameter has little effect on the particulate distribution within the molten salt flow. The same centrifugal force results in the particles lining the outer edges

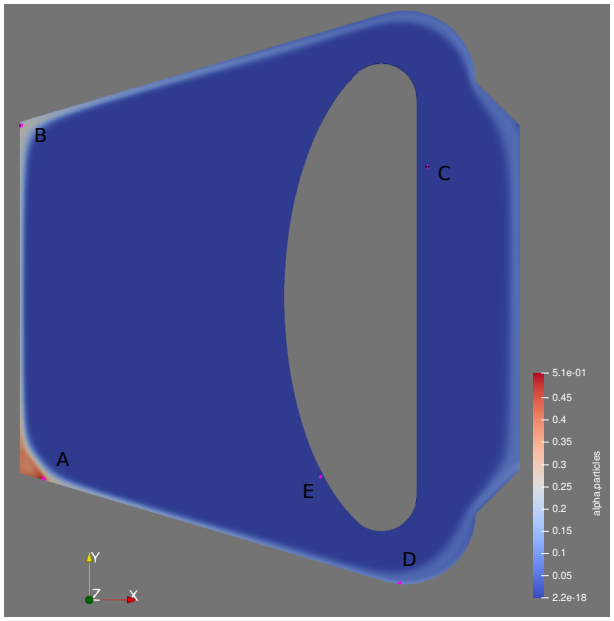

Figure 6.8: Particle Distribution - Case 3

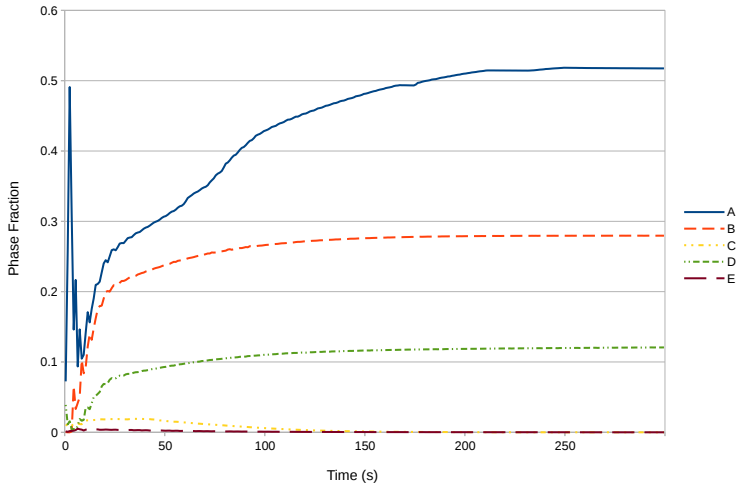

Figure 6.9: Particle Concentration over Time (5 min) - Case 3

of the reactor.

While all the cells containing particle concentrations above the initial concentration of 1% are along the outer edges, most places remain relatively low in the range of 5%. In reality, these are fairly high concentrations of particulates, it indicates that particulates of an approximate density of 6180 kg/m^3 or higher could be drawn from the reactor around the outer edges.

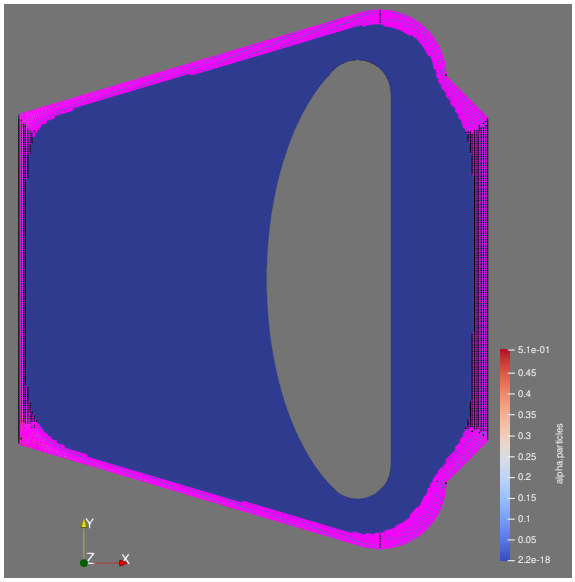

Figure 6.10: Concentrations Above 1% by Volume - Case 3

TEMPERATURE

The minimum and maximum temperatures seen in Case 3 are the same as those seen in the previous cases, further reinforcing the notion that particulate diameter has little influence on the thermal properties and fluid dynamics of this scenario. Figure 6.11 depicts the temperature across the core and Figure 6.12 shows the time dependent temperature for the indicated points.

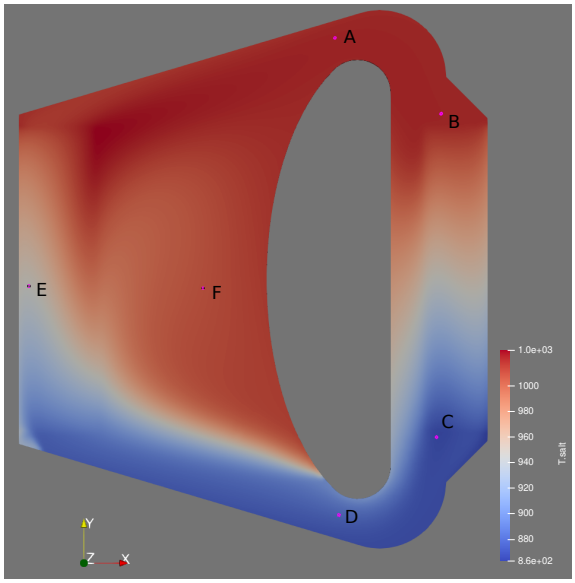

Figure 6.11: Temperature Contour Plot - Case 3

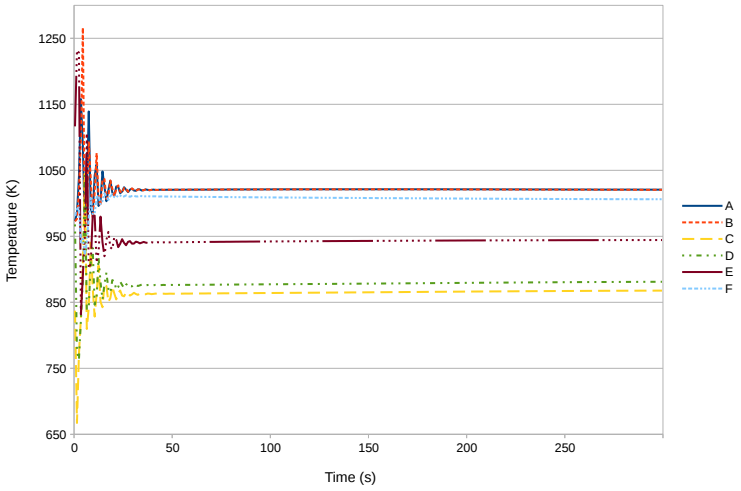

Figure 6.12: Temperature Monitor at Key Points - Case 3

VELOCITY

The maximum velocity is maintained at 4.51 m/s with a near identical velocity contour plot as in Cases 1 and 2. Figure 6.13 shows the contour plot for Case 3.

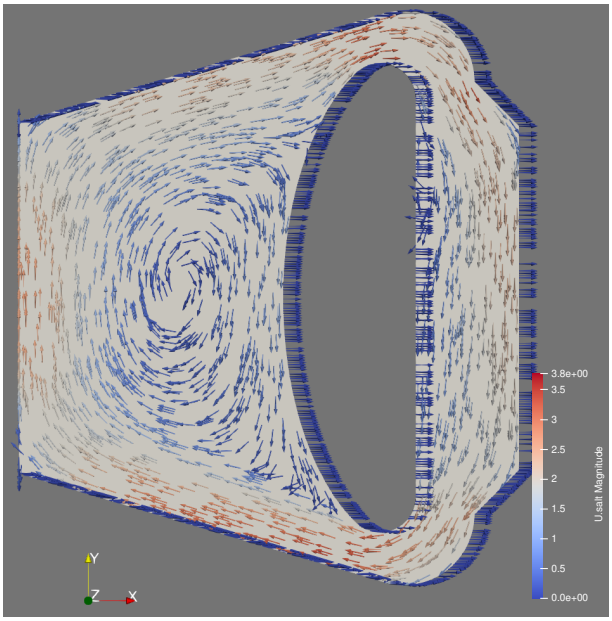

Figure 6.13: Steady State Velocity Vector Plot - Case 3

RESIDUALS

The convergence of the high particulate diameter case was similar to that of the base case and the low particulate diameter case. As observed in Figure 6.14, minor variations occurred, but the residuals were

generally between 1×10^{-8} and 1×10^{-13} and they were continuing to trend down at the end of the simulation.

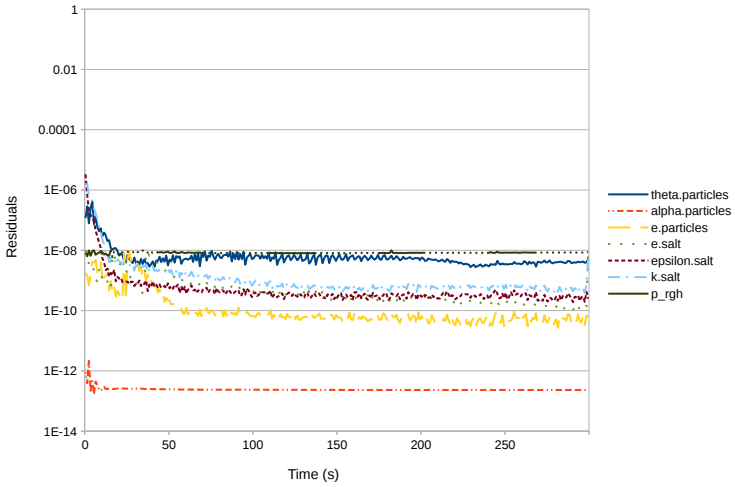

Figure 6.14: Residuals Plot - Case 3

6.2.3. CASE 4: LOW PARTICULATE DENSITY

PARTICULATE CONCENTRATION

As the density was reduced from 6180 kg/m^3 to 4240 kg/m^3 in Case 4, compared to the salt density of 4125 kg/m^3, there is an obvious variance in the particulate distribution as depicted in Figure 6.15.

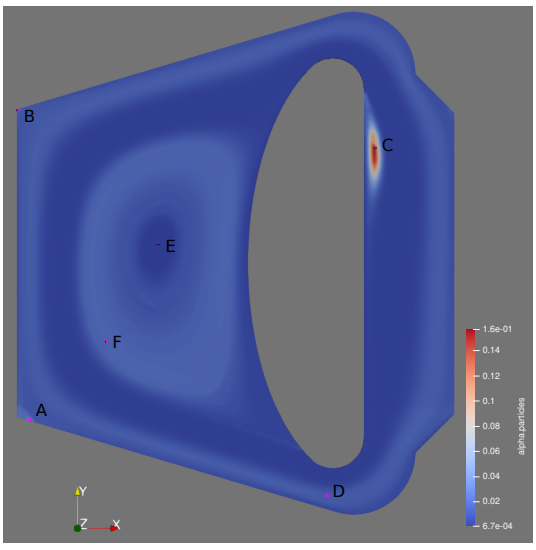

Figure 6.15: Particle Distribution - Case 4

While the effect of the centrifugal force is still apparent, the distribution is not nearly as stark as the previ-

ous cases. Point C which was shown as having a local peak in the previous cases for the first 100 seconds of the simulation not only maintains its peak for the full duration of the simulation, but it is the highest concentration location across the model. It is noted that this peak is only 16% compared to 52% in the previous cases. This indicates that it would be preferential to remove as many high density particulates as possible during operation of an MSR to avoid localized areas of extremely high concentration. In addition to the benefit of a more gradual temperature gradient that would be expected to result in a longer overall reactor life, it allows for the removal of long-lived, higher activity fission products.

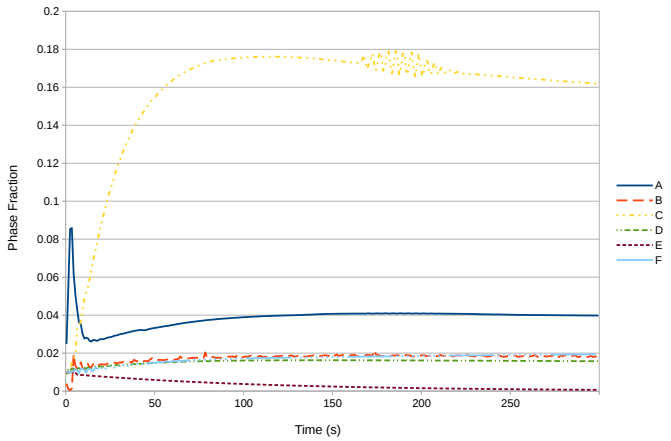

Figure 6.16: Particle Concentration over Time (5 min) - Case 4

Reinforcing the point, it can be seen in Figure 6.17 that there is a much more broad distribution of particulates being over 1%, but from reviewing Figure 6.16, the vast majority of locations are under 5%.

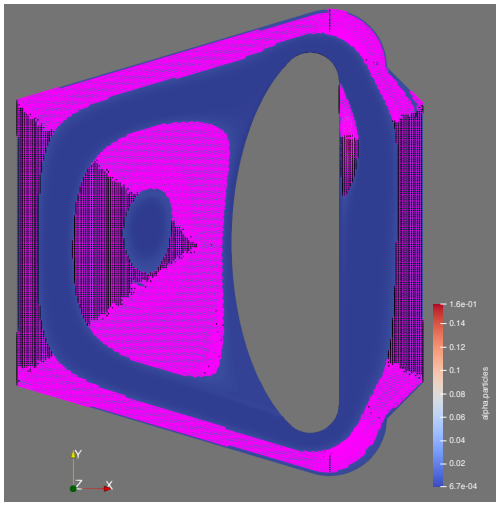

Figure 6.17: Concentrations Above 1% by Volume - Case 4

TEMPERATURE

The temperature profile remained largely unchanged even with the considerable variation in particulate distribution. Peak temperature remained close to the same at 1029 K, and the minimum was 857 K.

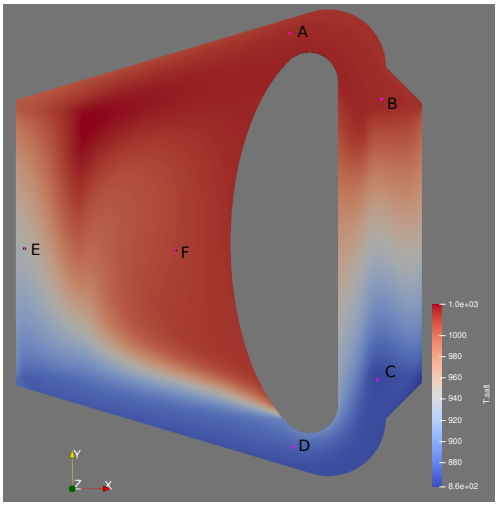

Figure 6.18: Temperature Contour Plot - Case 4

Point A from Case 1 Figure 5.5 shows the high particulate concentration of 52% for that case. In reviewing Figure 5.9, it is apparent there is a higher temperature at this location compared to Figure 6.18. This is because particulates did not collect at this same location in Case 4. This is further reinforcement that eliminating the local points of high particulate concentration can reduce the risk of temperatures being higher than preferred throughout the core. Figure 6.19 shows the point monitor temperatures do not noticeably differ from previous cases.

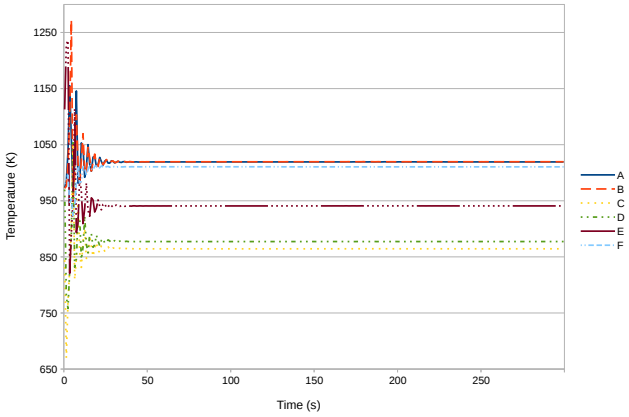

Figure 6.19: Temperature Monitor at Key Points - Case 4

VELOCITY

The predicted velocity vector plot in Figure 6.20 is similar to the previous cases. There is a slight decrease to the peak velocity from 4.51 m/s to 4.31 m/s at the same location near the heat exchanger inlet, likely due to the broader distribution of particulates leading up to and existing in that area slowing the salt.

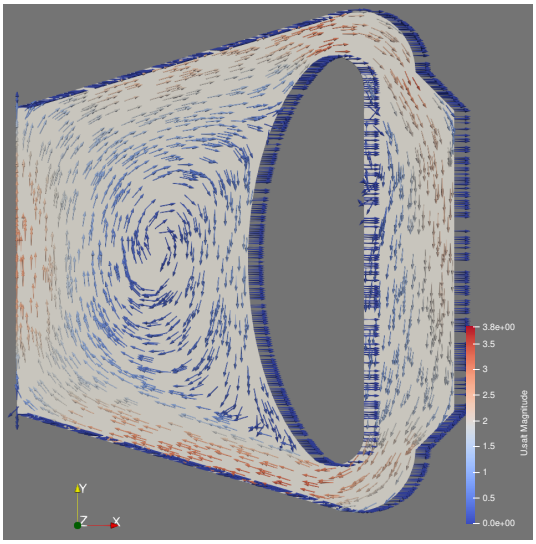

Figure 6.20: Steady State Velocity Vector Plot - Case 4

RESIDUALS

The residual values changed somewhat for this case. Less so in the manner of actual values, but the trending varied considerably. This is shown in Figure 6.7.

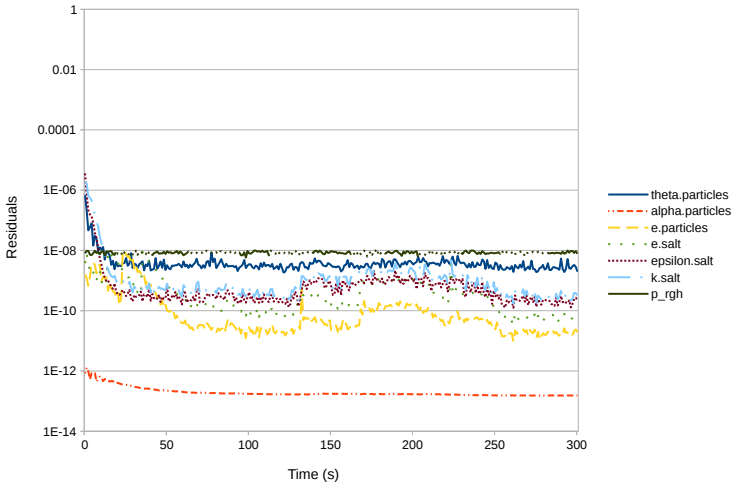

Figure 6.21: Residuals Plot - Case 4

The values still remained largely between 1×10^{-8} and 1×10^{-13}. For most values except *Theta.particles*, *alpha.particles*, and *p_rgh*, the residual values appear to be continuing in their reduction near the end of the simulation. In addition, there were larger variations in *e.particles*, *e.salt*, *k.salt*, and *epsilon.salt* residuals. The residuals for *alpha.particles* appear slightly lower than in the previous cases, indicating more stability in the simulation with lower density particulate.

6.2.4. CASE 5: HIGH PARTICULATE DENSITY

PARTICULATE CONCENTRATION

The high particulate density scenario investigated in Case 5 is unsurprisingly an inverse of the low density case, where a more intense impact of the centrifugal force is seen on the distribution of particulate.

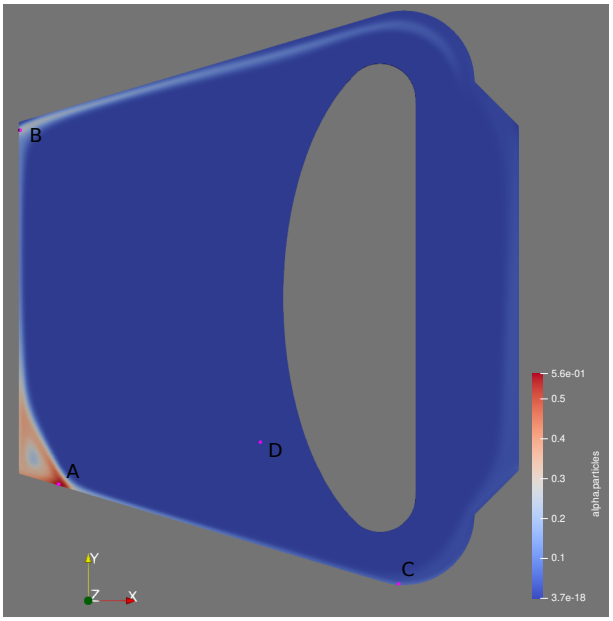

Figure 6.22: Particle Distribution - Case 5

Not only was the highest concentration greater at the end point, at 56% instead of 52%, but there is no steady state reached for the particulate. It continues to move around the core, as the new density of 8200 kg/m^3 is substantially higher than the salt density of 4125 kg/m^3. While not apparent from Figure 6.22, Figure 6.23 shows that there was no stability at Points A, B, and C along the outer edges of the model.

Figure 6.24 shows the particulate distribution at four different times nearing the end of the simulation. It can be seen that the particulate groups together and is carried around the outer edge of the model with

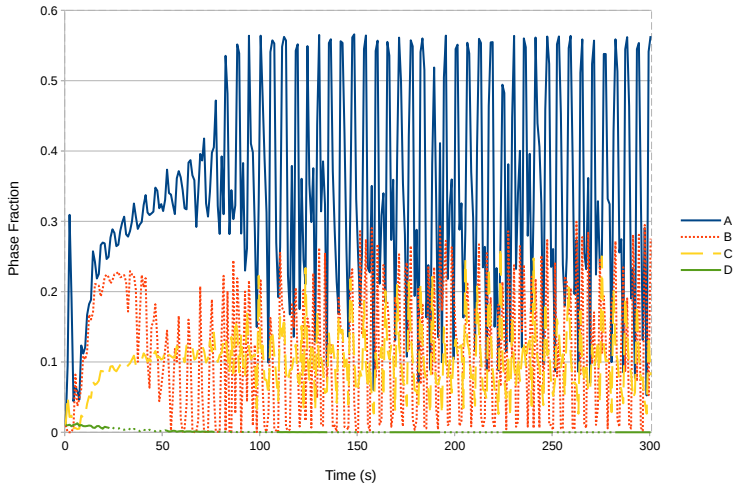

Figure 6.23: Particle Concentration over Time (5 min) - Case 5

the flow of the salt. Point A still tends to have a high concentration throughout the simulation, where Point B ranges from nearly zero to almost 30%, and Point C being near the base of the reactor, has a minimum around 5% and peaks in the similar range of Point B.

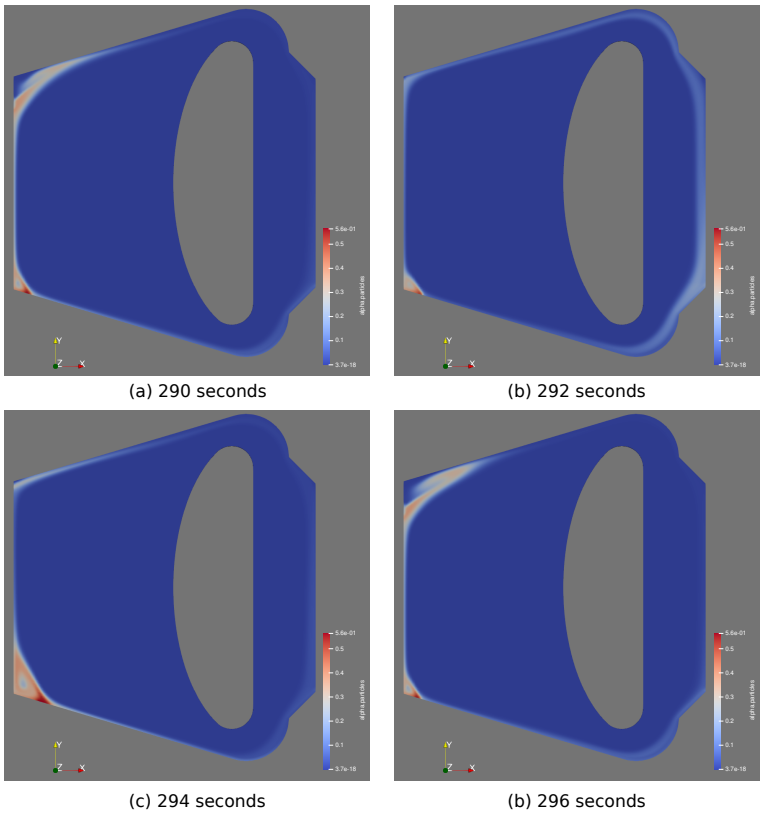

(a) 290 seconds (b) 292 seconds

(c) 294 seconds (b) 296 seconds

Figure 6.24: Particle Distribution 8 Second Duration - Case 5

This further points to the notion that density of the particulate has a major influence on the behaviour of particulate flow in such a reactor and high density particulate should be a focus point for filtration techniques in reactor design. It is reiterated that these CFD simulations have not been validated by experiments and it cannot be confirmed that these results are realistic, but higher density particulate would realistically be expected to collect at lower locations in the core due to gravity, which is observed in the simulation results. In addition, particles can be expected to aggregate as discussed in Section 4.1, indicating these results could be realistic based on theory.

TEMPERATURE

Case 5 is the first instance where a noticeable change has been observed in the temperature distribution of the reactor. Figure 6.25 shows the predicted peak temperature near 1100 K.

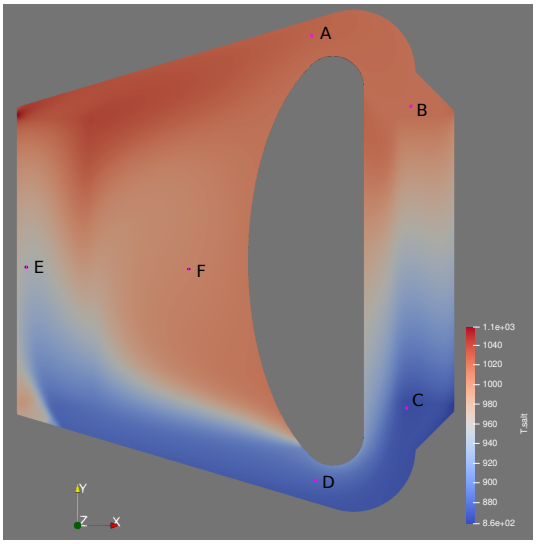

Figure 6.25: Temperature Contour Plot - Case 5

The predicted peak temperature has increased to 1059 K, while the minimum was maintained around 858 K. The fluctuations of the particulate distribution are reflected in the temperature profile, where the point monitors in Figure 6.26 show fluctuating values at each of them compared to the stable values seen previously. Due to the nature of the values cycling around certain values, the simulation appears to be nearing steady-state. Point F shows a continuing decreasing trend that indicates additional time would be required to achieve steady-state if the simulation will eventually reach such a state. Section 6.2.4 explains that trends in residuals indicate it may not have converged for quite some time, so the

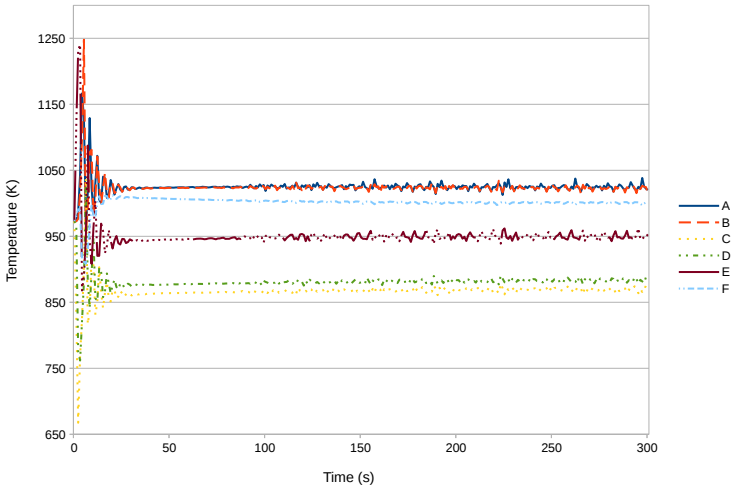

Figure 6.26: Temperature Monitor at Key Points - Case 5

simulation was only run as long as the other cases to compare the effects of high density particulate on the flow behaviour. In addition, the higher local temperature occurred at the bottom of the centre of the core, where the high particulate concentration is shown as Point A in Figure 6.22.

VELOCITY

The computed vector plot for Case 5 is similarly unchanged from the base case and others as seen in Figure 6.27. The large vortex remains in the core with the same overall trend in direction and velocity. The final state peak velocity was 4.32 m/s, but this ranged from 4.08 m/s to 4.41 m/s in the last 20 seconds.

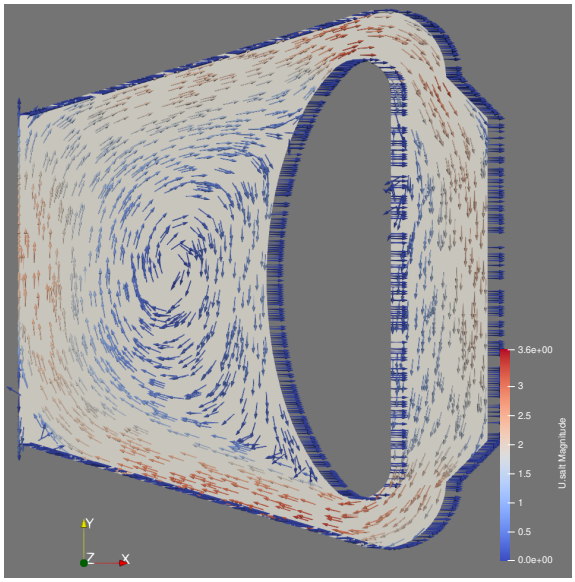

Figure 6.27: Steady State Velocity Vector Plot - Case 5

RESIDUALS

With the simulation not reaching a true steady-state in this scenario, the simulation did not converge to the same level as previous cases. Figure 6.28 shows the *alpha.particles* residual fluctuates around 1×10^{-12} and other values were between 1×10^{-6} and 1×10^{-10} at the simulation end with a slight increasing trend. The simulation may not have reached true convergence for quite some time, if ever.

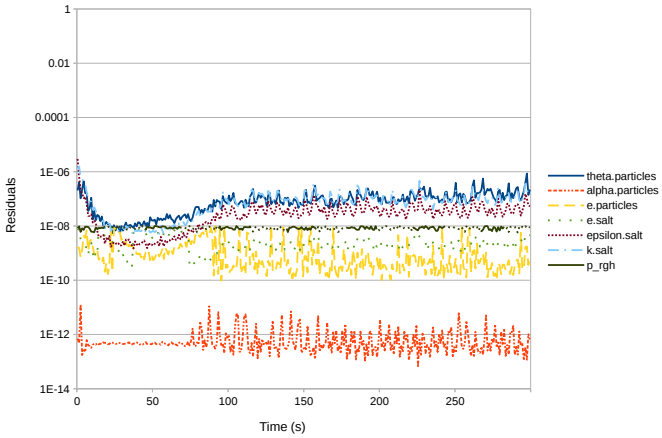

Figure 6.28: Residuals Plot - Case 5

6.2.5. CASE 6: LOW INITIAL PARTICULATE CONCENTRATION

PARTICULATE CONCENTRATION

Particulate concentration was reduced to 0.15% for the initial conditions in Case 6.

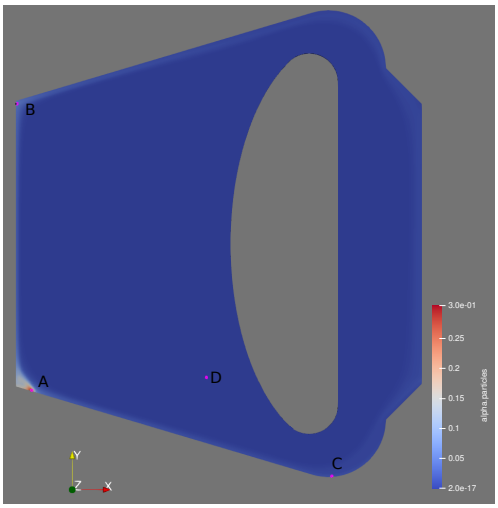

Figure 6.29: Particle Distribution - Case 6

Figure 6.29 shows that generally the concentration is lower than the base case, as is expected. The maximum predicted concentration occurs at 33% per Figure 6.30, instead of 52% as seen in Case 1.

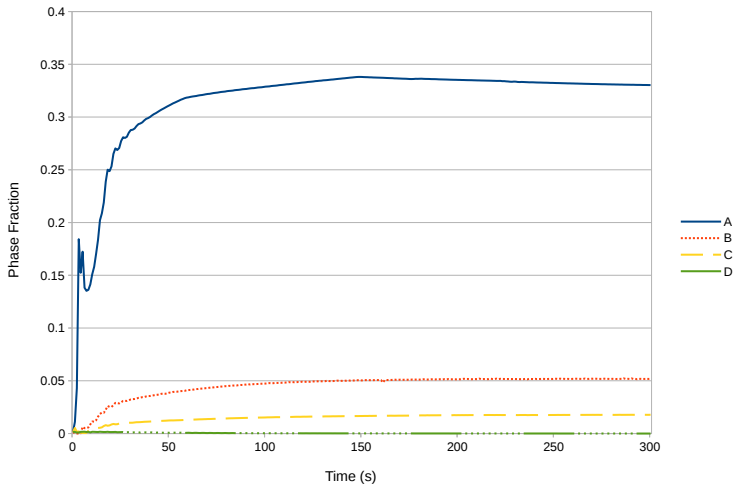

Figure 6.30: Particle Concentration over Time (5 min) - Case 6

The collection around the inlet of the heat exchanger does not occur in this case and the distribution of particles over 1% concentration remains around the outer edges as the density remains 6180 kg/m^3 for the particulate in this case. This is shown in Figure 6.31.

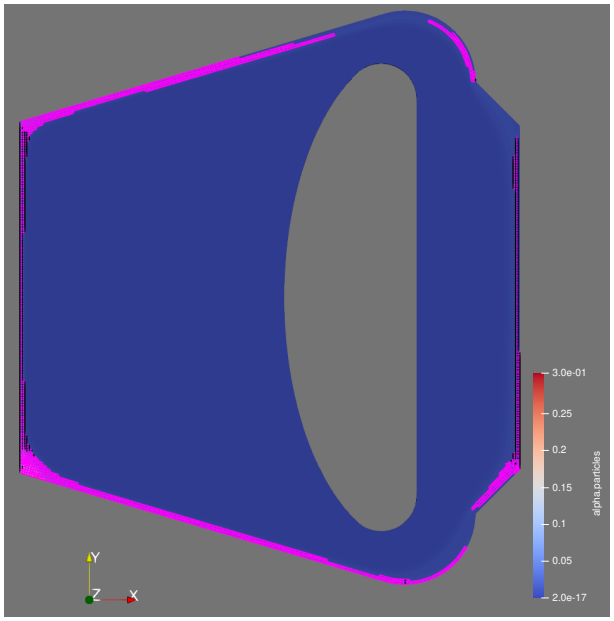

Figure 6.31: Concentrations Above 1% by Volume - Case 6

TEMPERATURE

Returning to base case density, the larger variances seen in the high density case are not repeated as is evident from Figure 6.32. While the maximum temperature is the same as that of the base case at 1028 K, the minimum temperature is 854 K. This is lower than the 863 K seen previously, but still above the melting temperature of the salt (837 K).

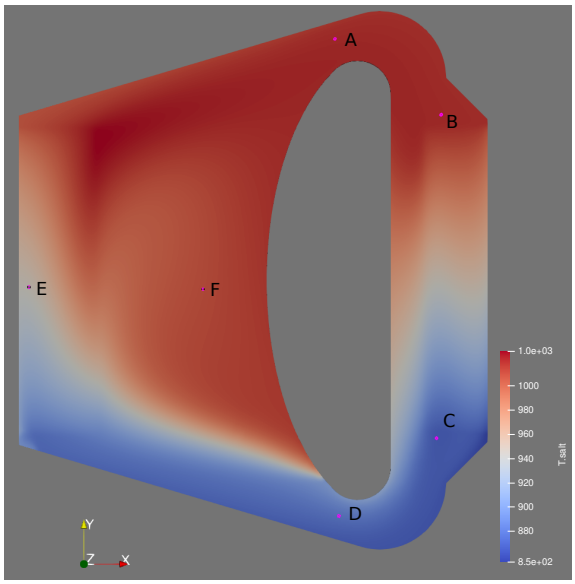

Figure 6.32: Temperature Contour Plot - Case 6

The general trend among the temperature point monitors remain stable and very similar to the values seen in the base case, as can be seen in Figure 6.33.

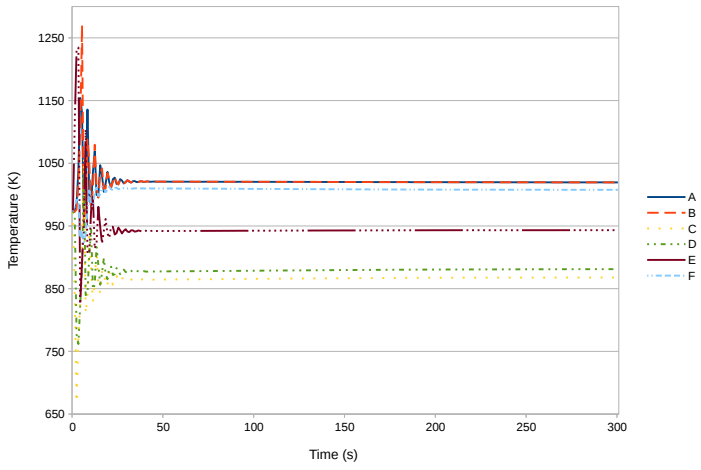

Figure 6.33: Temperature Monitor at Key Points - Case 6

VELOCITY

The velocity vector plot calculated in Case 6 (Figure 6.34) is effectively the same as the base case, with a lower peak velocity of 4.26 m/s. The flow pattern remains the same with comparable velocities overall.

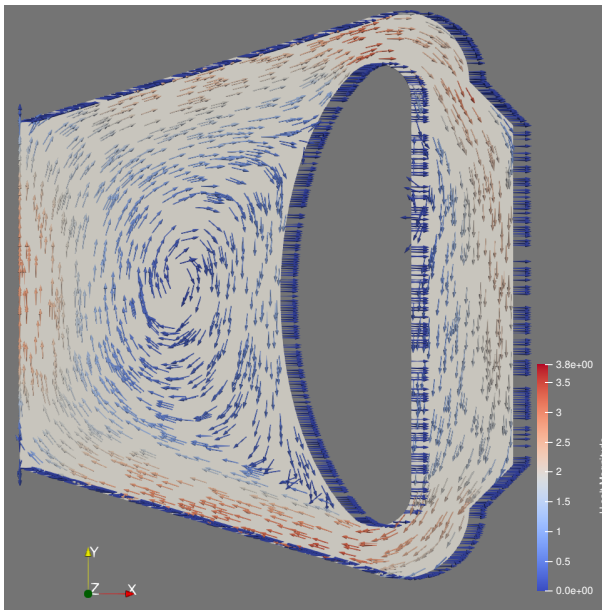

Figure 6.34: Steady State Velocity Vector Plot - Case 6

RESIDUALS

Residuals shown in Figure 6.35 returned to a more stable state in the low concentration simulation, indicating that lower levels of particulate result in lower impact to the physics of the reactor.

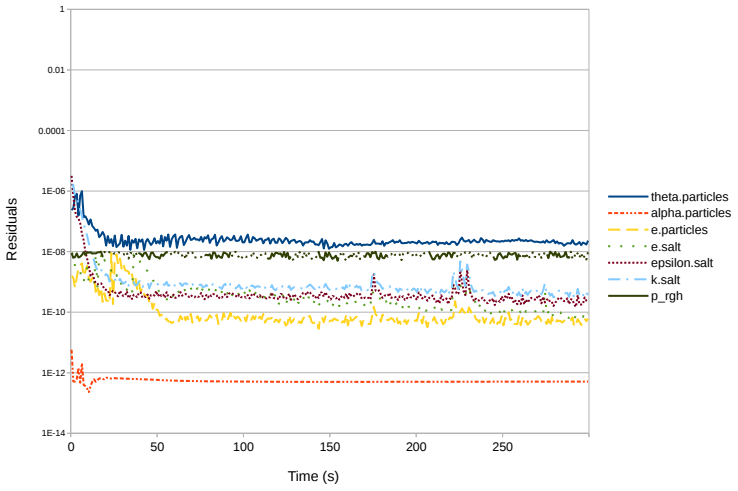

Figure 6.35: Steady State Velocity Vector Plot - Case 6

6.2.6. CASE 7: HIGH INITIAL PARTICULATE CONCENTRATION

PARTICULATE CONCENTRATION

Case 7 utilized a high concentration of particulates, with the initial conditions of 3.5% by volume. Figure 6.36 shows the distribution at the final time step with the highest concentration at the base of the core.

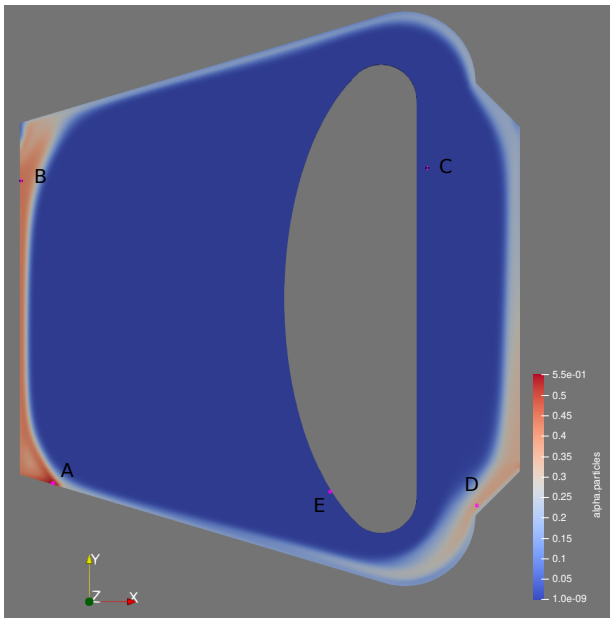

Figure 6.36: Particle Distribution - Case 7

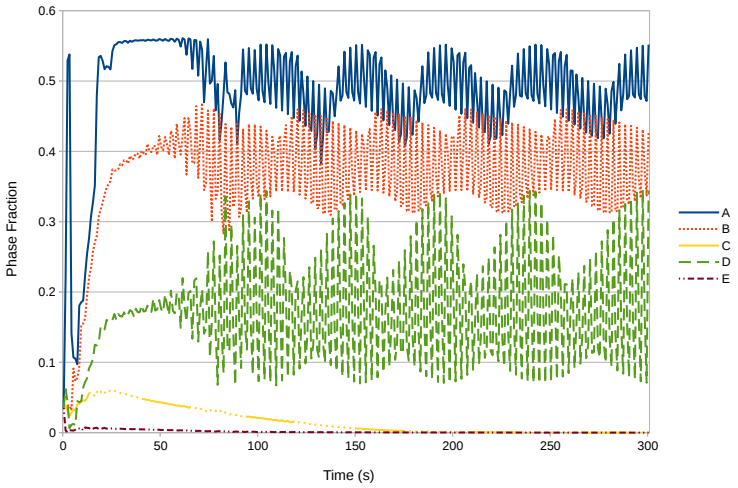

Figure 6.37: Particle Concentration over Time (5 min) - Case 7

Similar to the high density case, this high level of particulate resulted in a cycle of particulates being carried around the reactor as opposed to collecting in one location. This is apparent from Figure 6.37,

where Points A, B, and D demonstrate a sinusoidal pattern in their local concentration values. Point A remains the highest in concentration for the majority of the simulation, where the temporary increases in Points B and D show that the group of particulate is moving around the reactor. Given the particle density is maintained at 6180 kg/m^3 for this case, the centrifugal force still maintains the particulate at the outer edges of the reactor as seen in Figure 6.38, even while it continues to change location.

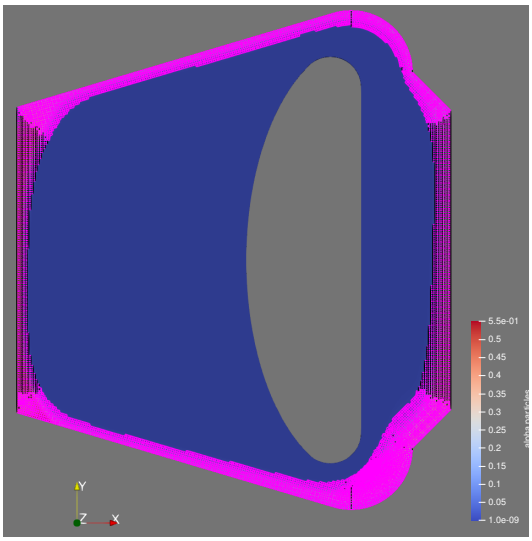

Figure 6.38: Concentrations Above 1% by Volume - Case 7

TEMPERATURE

The predicted temperature fluctuates with the movement of particulates, as seen in Figure 6.39.

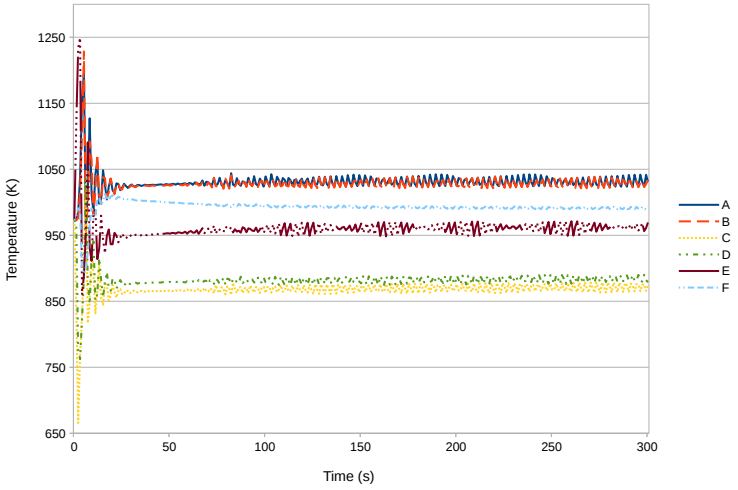

Figure 6.39: Temperature Monitor at Key Points - Case 7

With a peak computed temperature of 1159 K, depicted in Figure 6.40, it is apparent that localized points with high levels of particulates create a risk for reactor operation through degradation or even melting of the reactor vessel. As particulate concentrations would likely increase over time, it is apparent that proper filtration techniques would be required to ensure continued stable reactor operation.

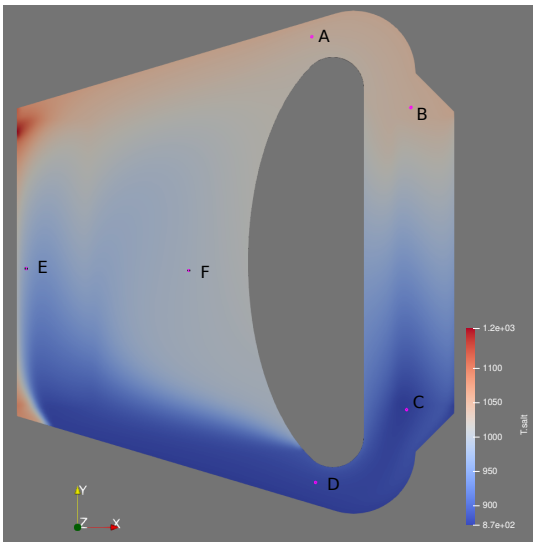

Figure 6.40: Temperature Contour Plot - Case 7

VELOCITY

The peak computed velocity ranges from 4.05 to 4.47 m/s in the last 20 seconds of the simulation, but the flow pattern is otherwise unchanged as seen in Figure 6.41.

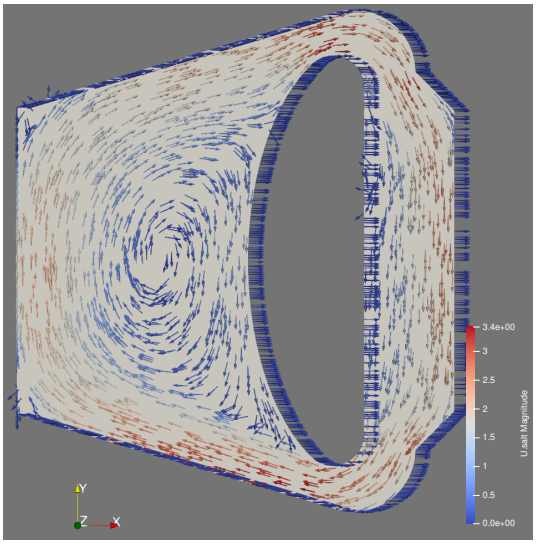

Figure 6.41: Steady State Velocity Vector Plot - Case 7

RESIDUALS

Figure 6.42 shows that the residuals in this case were similar to those in Case 5 with values for all but *alpha.particles* and *p_rgh* being between 1×10^{-6} and 1×10^{-10} for the majority of the simulation. The *alpha.particles* residuals cycled around 1×10^{-13}, and this case overall appeared to be converging better that Case 5 in that the residuals were still decreasing or had reached a plateau.

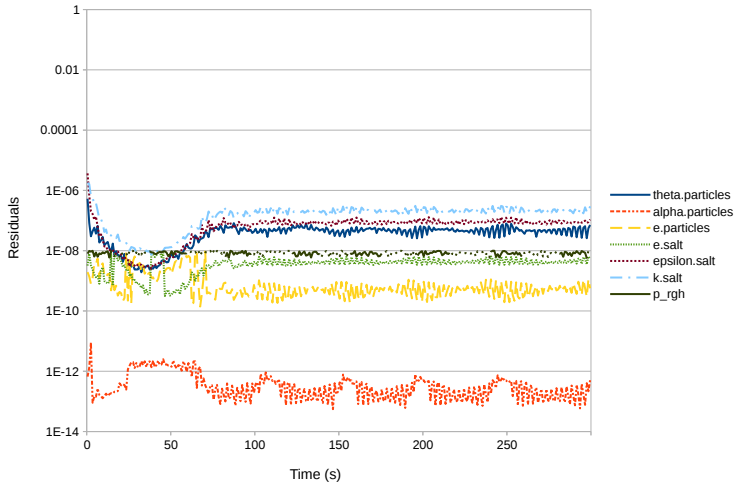

Figure 6.42: Steady State Velocity Vector Plot - Case 7

6.3. COMPARISON SUMMARY

The following section includes an overarching comparison of the six cases against the base case and further discussion on the implications of the variations of the three modified parameters. Table 6.2 lists attributes associated with each case, related to concentration, particulate movement, and temperature properties. In Cases 5 and 7, the particles were predicted to be cyclically carried around the outer edge of the core, so the values can change even in a steady state condition, but the values provided were taken at the end of the simulations (300 s).

It is immediately apparent that neither Case 2 nor Case 3, in which the particulate diameter was modified, resulted in any considerable change predicted from the base case. As the density and concentration of the particulate remained constant, the total number of particles was reduced such that the solid mass was maintained. This shows that the range of expected particulate size is not sufficiently large to influence the flow profile, particulate behaviour, or temperature profile in a meaningful way when there is no

Table 6.2 Results of the Sensitivity Analysis for the Simulation of Particle Transport in MSR Core

Case No.	Particulate Diameter (mm)	Density (kg/m^3)	Initial Concentration (% vol)	Max. Particulate Concentration (% vol)	Average Temp.	Min. Temp. (K)	Margin to Freezing (K)	Max. Temp. (K)	Max. Velocity (m/s)
1	1.5	6180	1.0%	52%	971	863	26	1028	4.51
2	0.02	6180	1.0%	52%	971	863	26	1028	4.51
3	3.0	6180	1.0%	52%	971	863	26	1028	4.51
4	1.5	4240	1.0%	16%	971	857	20	1029	4.31
5	1.5	8200	1.0%	56%	971	858	21	1059	4.32
6	1.5	6180	0.15%	33%	971	854	17	1028	4.26
7	1.5	6180	3.5%	55%	972	871	34	1159	4.43

impact on solid mass.

Case 4, in which the particulate density was reduced, was the first instance in which a few changes were observed when compared against the base case. First, there was a major reduction in the maximum particulate concentration from 52% to 16%. This was due to the lighter particles mixing more evenly with the salt because the centrifugal force of the salt flow had less of an effect on them. Because of this, the minimum temperature also decreased as the collection of the particles along the outlet of the heat exchanger did not group in such a way that inhibited heat transfer. It is noted that this increases the risk associated with fuel salt freezing, as the margin reduces to 20 K from the already small margin of 26 K. The maximum temperature was similarly reduced. As more particulates block the areas leading to the point of highest velocity, the maximum velocity is also reduced.

When the particulate density was increased to 8200 kg/m^3 for Case 5, it increased the predicted peak particulate concentration to 56% as the centrifugal forces pushed more particles together. The minimum temperature remained low as the particles collected along the edges where the cold temperatures occurred in the free flow of salt after the heat exchanger. The maximum temperature was high due to collection of particles in the upper left corner of the visible model following the heat generation. In this case, the particles continue to flow around the outer edge of the reactor, so there is no constant max temperature or velocity, but with no change in average temperature in any cases thus far, it is apparent that the system is being treated as "closed" based on the constant and equal levels of heat being generated and removed from the system.

The initial concentration was reduced to 0.15% by volume in Case 6, where an expected reduction in the maximum particle concentration occurred, along with the minimum and maximum temperatures due to the improved heat transfer with minimized collections of particles around the edges of the core. This case had the lowest "margin to freezing", indicating that modifications to the design would be required to ensure sufficient safety factor such that the fuel would not freeze. Maximum velocity was also reduced.

Case 7 saw the increase of initial particulate concentration to 3.5%, resulting in a near tie for the highest particle concentration, but demonstrably the highest minimum and maximum temperatures, as collections of particulate inhibited heat transfer. Interestingly, Case 7 saw a marginal increase in average temperature to 972 K. However, this was actually less than one degree difference from the other cases accounting for significant figures and can be likely attributed to error in the calculations based on the small variance. The velocity reduced in this case, but it is noted that it would vary as the particles travel around the reactor.

The Molten Salt Reactor Experiment at Oak Ridge National Laboratory, which noted that while the "Fine particles appeared to have been swept out by the draining fluid, . . . [l]arger particles accumulated near the drain line" [2]. In this work, there is no draining of the fluid, and the particle size did not appear to have any influence on particle collection, but the particle density was also unchanged even when larger diameter particles were used. In reality, it would be expected that particles varying in size will not all be of the same density, and large dense particles will likely collect in the same manner the high density particles did in Case 5. This leads to the discussion around other modifications that can be made to better represent reality, which are outlined in Chapter 8.

There are two key conclusions that can be drawn from these simulations, First, it is predicted that the particulate size does not have a big impact when sizes are within the range expected to be seen in these reactors. Second, the density and concentration were computed to have considerable impact as they can influence maximum particle concentration that heavily influences minimum and maximum temperatures. The overall message here is that mass of the particulate in the reactor has considerable influence and can cause particles clouds in which the particles cyclically move around the outer edge of the reactor. These results will not fully represent reality based on the high number of variables which are not adjusted or not included in this work, but these findings can contribute to further work on the topic that

will better represent a realistic simulation. The summarized conclusions of these results are provided in Chapter 7.

7

CONCLUSIONS

CFD simulations have been performed and the results of these simulations have been documented to contribute to the understanding of how solid particulates behave in a molten salt loop. The simulations were set up based on a review of literature that captured the properties of MSRs, the solid particulates that could be expected to exist in MSRs, and the requirements of CFD software settings to simulate the behaviour. A base case scenario was simulated in which a 2-D axially symmetric model of a MSR with fuel composed of LiF (77.5% mol) – ThF (20.0% mol) - $^{233}UF_4$ (2.5% mol) was set up, where it was assumed that solid particulates were suspended in the salt. A parametric sensitivity analysis was performed to compare changes in the flow properties and behaviour of the solid particulates caused by variations in the size, density, and concentration of the solid particulates in the core.

Key findings of the base case simulation and the sensitivity analysis are documented in the list below:

1. The solid particulates experienced the effects of centrifugal force, as their density being higher than the salt resulted in the collection of particulates along the outer edges of the core. A maximum particle concentration of 52% was predicted in the base case.

2. Reducing the diameter of the particles to 0.02 mm and increasing it to 3.0 mm had little effect on the particle collection behaviour. As the particles have the same density and the concentration as base case, the number of particles is reduced and the total mass of solid content is maintained, limiting the impact on flow behaviour.

3. A solid particulate density reduction from of 6180 kg/m^3 to 4240 kg/m^{3}resulted in more consistent distribution of the particles among the core and reduced the maximum particulate concentration to 16%, eliminating local hot spots seen in the base case.

4. Increasing the particulate density to 8200 kg/m^3 led to a more extreme version of the results seen in the base case, where the centrifugal effect pushed the particles even more closely together along the outer edges of the reactor. However, particle distribution did not remain stationary as they were carried by the flow along the outer edges of the reactor, periodically reaching a maximum concentration of 56% and increasing the peak predicted temperature by 3% above the base case from 1028 K to 1059 K.

5. An decrease in the concentration of the particulate from 1.0% to 0.15% reduced the maximum particulate concentration to 33% where particles were distributed along the edges of the core.

6. At a particulate concentration of 3.0%, particles collected along the outer edges of the reactor, but cycled with the flow pattern. This created hot spots at high concentration areas that raised reactor temperatures by up to 13% from 1028 K to 1159 K.

7. There was minimal impact on the flow pattern and velocity in the core for each of the cases.

As these simulations include a 2-D rendition of a closed-system that includes assumptions of static fuel composition and reactor power, excludes the gaseous phase, and excludes interfaces with other systems, it does not fully capture what would be expected in reality. There are many variables that need to be taken into account in MSRs that are not captured in these simulations, and they have not been validated by experiments.

The primary objective of this work was to obtain a better understanding of the flow characteristics of solid particulate precipitated from the salt in the core of a molten salt reactor. It has been shown that

particulates can have a considerable impact on the reactor operation, specifically with regards to congregating such that localized temperature values are increased, impacting flow to a limited extent, and increasing the risk of occurrence of flow blockages. While this work did not simulate the intricate mechanics of a molten salt pump, this would be a piece of equipment where particles could accumulate and result in blockages or impact the reactor in other ways. The density profile of the generated particulate and the overall concentration are more likely to cause issues in reactor operation when they are higher. As such, it is important to design molten salt reactors to minimize the likelihood of particulate collection, and ensure there are appropriate filtration methods utilized in molten salt reactor operation to limit the overall particulate concentration. Filtration techniques could take advantage of the fact the higher density particulate is simulated to collect primarily in the centre of the core. A helium sparging system could be designed to disperse the particulate from this location, where it would more evenly mix into the rest of the flow and a portion of the flow could be circulated through a separate processing facility. Further to these conclusions, recommendations for future work related to CFD simulations of molten salt reactors are provided in Chapter 8.

8

RECOMMENDATIONS FOR FUTURE WORK

Where this report documents the impact of modifying the three parameters of particle size, density, and initial concentration in a molten salt 2-D axially symmetrical simulation, other work can be performed to improve the approximation of a realistic reactor.

8.1. OPENFOAM MODIFICATIONS

Additional OpenFOAM simulations could be performed with similar cases that better represent realistic properties of molten salt reactors. Specifically, the solid particulates within an MSR would not occur at a single density, particulate size, or concentration. These values would span a series of compounds that would be generated in such a reactor, and would change over time. Further simulations could better capture the transient nature of these particulates.

The addition of a gaseous phase, likely the common cover gas helium, would reflect MSR operation more accurately. This could be done first as a simulation with salt and the gas as two-phase flow, and subsequently three-phase flow including solid, liquid, and gaseous phases. As MSFRs will typically include

helium sparging processes to filter out gaseous fission products, sole use of helium in the gaseous phase would likely yield sufficiently accurate results.

A solver titled *multiphaseEulerFoam* was used in the simulations of this work, which is a native solver that comes with the base installation of OpenFOAM. While designed for use of compressible and incompressible fluids, and is used to capture solids as well, the solver can be modified to better account for the use of solid, liquid, and gaseous phases.

8.2. COUPLING WITH OTHER SOFTWARE

In the same way the solid particulate properties (size, density, etc.) vary during reactor operation, so does the composition of the molten salt. A means of capturing this time-based composition would be to couple OpenFOAM with other software to capture the complex behaviour of compounds based on temperature and pressure, and long-term exposure to neutron fields that result in transmutation of the salt. Specifically, the coupling of OpenFOAM with Thermochimica could be used for the purpose of predicting phase transformations as described in work by Scuro *et al.* [54]. Results of simulations using such tools would better allow designers to determine how and when to employ filtration technologies to return or maintain the salt at a certain composition that best suits the design basis. Capturing the correct phases of the bulk salt along with calculating the neutronics would best represent the behaviour expected to be seen in reality.

8.3. EXPERIMENTAL WORK

Following further simulations as outlined in Sections 8.1 and 8.2, it would be prudent to perform experimental work to validate the findings of the simulations related to solid particulate and salt behaviour, and prove the concepts associated with fuel composition management. Initially, molten salts that exclude radioactive material would be preferred, where solid particulates born from fission products can be represented using components known to have melting temperatures above the applicable operational temperature and particles sizes and densities similar to those identified in this report. With various sizes, densities, and concentrations of solid particulates, flow and temperature measurements can be used potentially in conjunction with ultrasonic or infrared density measurements to determine how the solid

matter impacts the flow behaviour. Radioactive material would eventually be incorporated into larger scale demonstration units in support of transition to grid-scale MSRs.

REFERENCES

[1] Igor Pioro, *Handbook of Generation IV Nuclear Reactors*, Elsevier Science & Technology, 2016.

[2] R. Robertson, "MSRE Design and Operations Report, Part I - Description of Reactor Design," Oak Ridge National Laboratory, Oak Ridge, TN, USA, Tech. Rep. ORNL-TM-728, 1965.

[3] D. Zhang, L. Liu, M. Liu, R. Xu, C. Gong, J. Zhang, C. Wang, S. Qiu, and G. Su, "Review of conceptual design and fundamental research of molten salt reactors in China," *International Journal of Energy Research*, vol. 42, pp. 1834–1848, 2018.

[4] F. Gelbard, B. Beeny, L. Humphries, K. Wagner, L. Albright, M. Poschmann, and M. Piro, "Application of MELCOR for Simulating Molten Salt Reactor Accident Source Terms," *Nuclear Science and Engineering*, in press.

[5] A. Di Ronco, S. Lorenzi, F. Giacobbo, and A. Cammi, "Multiphysics analysis of RANS-based turbulent transport of solid fission products in the Molten Salt Fast Reactor," *Nuclear Engineering and Design*, vol. 391, p. 111739, 2022.

[6] Terrestrial Energy, *Terrestrial Energy Congratulates OPG for Darlington Site Work Approval*, https://www.terrestrialenergy.com/2021/10/terrestrial-energy-congratulates-opg-for-darlington-site-work-approval, October 2021, Accessed: 2023-03-05.

[7] Terrestrial Energy, *Overview of the Terrestrial Energy IMSR Cogeneration Plant*, https://www.terrestrialenergy.com/media/overview-of-the-terrestrial-energy-imsr-cogeneration-plant/, February 2023, Accessed: 2023-02-27.

[8] Moltex Energy, *Technology suite*, https://www.moltexenergy.com/technology-suite/, February 2023, Accessed: 2023-02-27.

[9] SAMOFAR, *Project - SAMOFAR*, http://samofar.eu/project/, February 2023, Accessed: 2023-02-27.

[10] SAMOSAFER, *Project - SAMOSAFER*, https://samosafer.eu/project/, February 2023, Accessed: 2023-02-27.

[11] Euratom, *Evaluation and Viability of Liquid Fuel Fast Reactor System*, 2015, https://cordis.europa.eu/docs/results/249/249696/final1-final-report-f.pdf Accessed: 2022-08-25.

[12] M. Aufiero, A. Cammi, O. Geoffroy, M. Losa, L. Luzzi, M. E. Ricotti, and H. Rouch, "Development of an OpenFOAM model for the Molten Salt Fast Reactor transient analysis," *Chemical Engineering Science*, vol. 111, pp. 390–401, 2014.

[13] A. Tosolin, O. Beneš, J.-Y. Colle, P. Soucek, L. Luzzi, and R. Konings, "Vaporization behaviour of the Molten Salt Fast Reactor fuel: The LiF-ThF_4-UF_4 system," *Journal of Nuclear Materials*, vol. 507, pp. 319–328, 2018.

[14] E. Merle, D. Heuer, A. Laureau, M. Brovchenko, M. Allibert, M. Aufiero, and V. Ghetta, "Physical Assessment of the Load Following and Starting Procedures for the Molten Salt Fast Reactor," 2015, Proceedings of ICAPP 2015.

[15] C. Forsberg, S. Lam, D. Carpenter, D. Whyte, R. Scarlat, C. Contescu, L. Wei, J. Stempien, and E. Blandford, "Tritium Control and Capture in Salt-Cooled Fission and Fusion Reactors: Status, Challenges, and Path Forward," *Nuclear Technology*, vol. 197, pp. 119–139, 2017.

[16] United States Geological Survey, *Resources on Isotopes | Periodic Table–Lithium*, 2004, https://wwwrcamnl.wr.usgs.gov/isoig/period/li_iig.html Accessed: 2023-02-27.

[17] C. Arthurs, "Knowledge Gap Assessment of the JRC Database for Irradiated Salts," 2020, Ontario Tech University, unpublished paper.

[18] Rita F. de Carvalho, *INTRODUCTION TO OPENFOAM*, 2019, https://2019.foam-iberia.eu/files/Curso_B1_introduction2OpenFOAM.pdf Accessed: 2022-08-16.

[19] U.S. DOE Nuclear Energy Research Advisory Committee, *A Technology Roadmap for Generation IV Nuclear Energy Systems*, http://web.archive.org/web/20100304230148/https://www.ne.doe.gov/genIV/documents/gen_iv_roadmap.pdf, December 2022, Accessed: 2023-03-05.

[20] World Nuclear Association, *Molten Salt Reactors*, 2022, https://www.world-nuclear.org/information-library/current-and-future-generation/molten-salt-reactors.aspx Accessed: 2022-08-25.

[21] B. Chisholm, S. Krahn, and K. Fleming, "A systematic approach to identify initiating events and its relationship to Probabilistic Risk Assessment: Demonstrated on the Molten Salt Reactor Experiment," *Progress in Nuclear Energy*, vol. 129, no. 103507, 2020.

[22] Joint Research Centre, *Joint Research Centre Molten Salt Database - JRCMSD*, 2022, https://joint-research-centre.ec.europa.eu/joint-research-centre-molten-salt-database-jrcmsd_en Accessed: 2022-08-25.

[23] G. Guéneau, N. Dupin, L. Kjellqvist, E. Geiger, M. Kurata, S. Gossé, E. Corcoran, A. Quaini, R. Hania, A. Smith, M. Piro, T. Besmann, P. Turchi, J. Dumas, M. Welland, T. Ogata, B. Lee, J. Kennedy, C. Adkins, M. Bankhead, and D. Costa, "TAF-ID: An international thermodynamic database for nuclear fuels applications," *CALPHAD: Computer Coupling of Phase Diagrams and Thermochemistry*, vol. 72, pp. 1–21, 2021.

[24] K. Lipkina, K. Palinka, E. Geiger, B. Fitzpatrick, O. Vălu, O. Beneš, and M. Piro, "Thermodynamic investigations of the LiF-CsF and NaF-CsF pseudo-binary system," *Journal of Nuclear Materials*, vol. 568, no. 153901, 2022.

[25] I. Clifford and C. Fiorina, *Lecture 1: An overview on the use of OpenFOAM as a multi-physics library for nuclear reactor analysis*, 2022, https://elearning.iaea.org/m2/course/view.php?id=1286 Accessed: 2022-08-26.

[26] E. Cervi, S. Lorenzi, A. Cammi, and L. Luzzi, "Development of a multiphysics model for the study of fuel compressibility effects in the Molten Salt Fast Reactor," *Chemical Engineering Science*, vol. 139, pp. 379–93, 2019.

[27] E. Cervi, S. Lorenzi, A. Cammi, and L. Luzzi, "Development of an SP3 neutron transport solver for the analysis of the Molten Salt Fast Reactor," *Nuclear Engineering and Design*, vol. 346, pp. 209–19, 2019.

[28] P. Bajpai, S. Lorenzi, and A. Cammi, "A multiphysics model for analysis of inert gas bubbles in Molten Salt Fast Reactor," *European Physical Journal Plus*, vol. 135, no. 409, 2020.

[29] F. Caruggi, A. Cammi, E. Cervi, A. Di Ronco, and S. Lorenzi, "Multiphysics modelling of gaseous fission products in the molten salt fast reactor," *Nuclear Engineering and Design*, vol. 392, p. 111762, 2022.

[30] C. Fiorina, D. Lathouwers, M. Aufiero, A. Cammi, C. Guerrieri, J. Kloosterman, L. Luzzi, and M. Ricotti, "Modelling and analysis of the MSFR transient behaviour," *Annals of Nuclear Energy*, vol. 64, pp. 485–498, 2014.

[31] D. Gérardin, A. Uggenti, S. Beils, A. Carpignano, S. Dulla, E. Merle, D. Heuer, A. Laureau, and M. Allibert, "A methodology for the identification of the postulated initiating events of the Molten Salt Fast Reactor," *Nuclear Engineering and Technology*, vol. 51, pp. 1024–1031, 2019.

[32] H. Rouch, O. Geoffroy, P. Rubiolo, A. Laureau, M. Brovchenko, D. Heuer, and E. Merle-Lucotte, "Preliminary thermal–hydraulic core design of the Molten Salt Fast Reactor (MSFR)," *Annals of Nuclear Energy*, vol. 64, pp. 449–456, 2014.

[33] D. Kamp, "Cooling requirements for the freeze plug module," B.Sc. Thesis, Delft University of Technology, Delft, Netherlands, 2018.

[34] T.-C. Ong, M. Sarvghad, K. Lippiatt, L. Griggs, H. Ryan, G. Will, and T. Steinberg, "Review of the solubility, monitoring, and purification of impurities in molten salts for energy storage in concentrated solar power plants," *Renewable and Sustainable Energy Reviews*, vol. 131, no. 110006, 2020.

[35] C. Xu, X. Li, Z. Wang, Y. He, and F. Bai, "Effects of solid particle properties on the thermal performance of a packed-bed molten-salt thermocline thermal storage system," *Applied Thermal Engineering*, vol. 57, pp. 69–80, 2013.

[36] Helvaci and S. Peker, *Solid–Liquid Two Phase Flow*. Elsevier, 2008.

[37] D. Jiang, D. Zhang, X. Li, S. Wang, C. Wang, H. Qin, Y. Guo, W. Tian, G. Su, and S. Qui, "Fluoride-salt-cooled high-temperature reactors: Review of historical milestones, research status, challenges, and outlook," *Renewable and Sustainable Energy Reviews*, vol. 161, no. 112345, 2022.

[38] P. Das, S. Mukherjee, R. Mishra, and S. Dash, "Thermodynamic and Physical Properties of Molten LiF-ThF_4-UF_4 Salts Mixture," *Journal of Fluorine Chemistry*, vol. 226, p. 109349, 2019.

[39] D. Gérardin, M. Allibert, D. Heuer, A. Laureau, E. Merle-Lucotte, and C. Seuvre, "Design evolutions of Molten Salt Fast Reactor," 2017, IAEA-CN245-575, Université Grenoble Alpes, Grenoble, France.

[40] E. Capelli, "Thermodynamic Characterization of Salt Components for Molten Salt Reactor Fuel," Ph.D. Thesis, Delft University of Technology, Delft, Netherlands, February 2016.

[41] W. Zhu, Z. Wang, X. Zhu, N. Shu, and T. Fan, "A new evaluation of fission product yields for the neutron induced fission of U-233 and Th-232," *Fusion Engineering and Design*, vol. 125, pp. 608–614, 2017.

[42] W. Cheng, B. Gu, C. Shao, and Y. Wang, "Hydraulic characteristics of molten salt pump transporting solid-liquid two-phase medium," *Nuclear Engineering and Design*, vol. 324, pp. 220–230, 2017.

[43] K. Shibata, O. Iwamoto, T. Nakagawa, N. Iwamoto, A. Ichihara, S. Kunieda, S. Chiba, K. Furutaka, N. Otuka, T. Ohsawa, T. Murata, H. Matsunobo, A. Zukeran, S. Kamada, and J.-I. Katakura, "JENDL-4.0: A New Library for Nuclear Science and Engineering," *Journal of Nuclear Science and Technology*, vol. 60, no. 4, pp. 1–30, 2010.

[44] W. Hayes, *Handbook of Chemistry and Physics*, ser. CRC Handbooks. CRC Press, 2015.

[45] C. Constable, B. Lindley, and G. Parks, "Maximising discharge burnup in an open cycle molten salt reactor," *EPJ Web Conf.*, vol. 247, no. 12002, 2021.

[46] B. R. Betzler, J. J. Powers, and A. Worrall, "Molten salt reactor neutronics and fuel cycle modeling and simulation with SCALE," *Annals of Nuclear Energy*, vol. 101, pp. 489–503, 2017.

[47] OpenFOAM Foundation, *multiphaseEulerFoam.C File Reference*, 2022, https://cpp.openfoam.org/v8/multiphaseEulerFoam_8C.html Accessed: 2022-09-27.

[48] OpenFOAM Foundation, *OpenFOAM 2.1.0: Multiphase Modelling*, 2011, https://openfoam.org/release/2-1-0/multiphase-interface-compressible-euler/ Accessed: 2022-09-27.

[49] OpenFOAM Foundation, *DPMFoam.C File Reference*, 2022, https://cpp.openfoam.org/v8/DPMFoam_8C.html Accessed: 2022-09-27.

[50] P. Shi, A.-E. Sommer, H. Rox, K. Eckert, and R. Rzehak, "Euler-Euler/RANS modeling of solid-liquid flow in stirred tanks: A comprehensive model validation," *Minerals Engineering*, vol. 185, no. 107679, 2022.

[51] CFD Direct, *Turbulence Modelling | OpenFOAM*, 2022, https://cfd.direct/openfoam/features/turbulence-modelling/ Accessed: 2022-09-26.

[52] S. Rodriguez, *Applied Computational Fluid Dynamics and Turbulence Modeling*. Springer, 2019.

[53] CFD Direct, *Reynolds-Averaged Simulations | Turbulence Modelling*, 2022, https://cfd.direct/openfoam/features/ras-turbulence-modelling/ Accessed: 2022-09-26.

[54] N. Scuro, M. Poschmann, O. Beneš, and M. Piro, "Progress in Coupling Computational Thermodynamics and Computational Fluid Dynamics to Support Molten Salt Reactor Applications," 2022, Proceedings of the Fourth International Conference on Generation IV and Small Reactors (G4SR-4), Toronto, Canada.

[55] OpenCFD Ltd, *Euler implicit time scheme*, 2016, https://www.openfoam.com/documentation/guides/latest/doc/guide-schemes-time-euler.html Accessed: 2022-10-15.

[56] OpenCFD Ltd, *Gauss gradient scheme*, 2018, https://www.openfoam.com/documentation/guides/latest/doc/guide-schemes-gradient-gauss.html Accessed: 2022-10-15.

[57] CFD Direct, *OpenFOAM v6 User Guide - 4.4 Numerical schemes*, https://doc.cfd.direct/openfoam/user-guide-v6/fvschemes, July 2018, Accessed: 2023-03-05.

[58] OpenCFD Ltd, *Linear divergence scheme*, 2017, https://www.openfoam.com/documentation/guides/latest/doc/guide-schemes-divergence-linear.html Accessed: 2022-10-15.

[59] OpenCFD Ltd, *Limited linear divergence scheme*, 2017, https://www.openfoam.com/documentation/guides/latest/doc/guide-schemes-divergence-limited-linear.html Accessed: 2022-10-15.

[60] OpenCFD Ltd, *Van Leer divergence scheme*, 2017, https://www.openfoam.com/documentation/guides/latest/doc/guide-schemes-divergence-vanleer.html Accessed: 2022-10-15.

[61] Y. Zhang, H. Pang, L. Feng, and X. Q. Jin, "Quadratic finite element and preconditioning methods for options pricing in the SVCJ model," *The Journal of Computational Finance*, vol. 17, no. 3, pp. 3–30, 2014.

[62] OpenCFD Ltd, *GAMG Solver*, 2017, https://www.openfoam.com/documentation/guides/latest/doc/guide-solvers-multigrid-gamg.html Accessed: 2022-10-16.

[63] OpenCFD Ltd, *Smooth Solver*, 2017, https://www.openfoam.com/documentation/guides/latest/doc/guide-solvers-smooth-smooth.html Accessed: 2022-10-16.

[64] ANSYS, *Lecture 7: Mesh Quality and Advanced Topics*, https://featips.com/wp-content/uploads/2021/05/Mesh-Intro_16.0_L07_Mesh_Quality_and_Advanced_Topics.pdf, February 2015, Accessed: 2023-03-04.

[65] ANSYS, *ANSYS Meshing Application Introduction*, https://www.researchgate.net/profile/Khalid-Saleem-4/post/What-is-the-best-and-bad-values-of-mesh-quality-variables-such-as-skewness-Orthogonal-Quality-maximum-cell-size-or-others-parameters-using-Fluent-CF/attachment/60885e1e220bc50001541637/AS%3A1017279433146368%401619549725508/download/Mesh+Quality-Appendix-A.pdf, 2009, Accessed: 2023-03-04.

[66] Center of Engineering Multiscale Modeling Fluid Flow, *Mastering twoPhaseEulerFoam*, https://www.cemf.ir/PDFs/OpenFOAM/Fluidizedbed.pdf, May 2020, Accessed: 2023-04-06.

[67] Kuron, M., *3 Criteria for Assessing CFD Convergence*, https://www.engineering.com/story/3-criteria-for-assessing-cfd-convergence, January 2015, Accessed: 2023-03-04.